

Shock waves in two-phase bubbly liquids

Cornel, W.A.

DOI

[10.4233/uuid:0384a3c9-eaf1-4fb8-a67a-93920da3f0df](https://doi.org/10.4233/uuid:0384a3c9-eaf1-4fb8-a67a-93920da3f0df)

Publication date

2024

Document Version

Final published version

Citation (APA)

Cornel, W. A. (2024). *Shock waves in two-phase bubbly liquids*. [Dissertation (TU Delft), Delft University of Technology]. <https://doi.org/10.4233/uuid:0384a3c9-eaf1-4fb8-a67a-93920da3f0df>

Important note

To cite this publication, please use the final published version (if applicable).
Please check the document version above.

Copyright

Other than for strictly personal use, it is not permitted to download, forward or distribute the text or part of it, without the consent of the author(s) and/or copyright holder(s), unless the work is under an open content license such as Creative Commons.

Takedown policy

Please contact us and provide details if you believe this document breaches copyrights.
We will remove access to the work immediately and investigate your claim.

SHOCK WAVES IN
TWO-PHASE BUBBLY LIQUIDS

AN EXPERIMENTAL STUDY

W.A. Cornel

SHOCK WAVES IN TWO-PHASE BUBBLY LIQUIDS

AN EXPERIMENTAL STUDY

SHOCK WAVES IN TWO-PHASE BUBBLY LIQUIDS

AN EXPERIMENTAL STUDY

Proefschrift

ter verkrijging van de graad van doctor
aan de Technische Universiteit Delft,
op gezag van de Rector Magnificus prof. dr. ir. T.H.J.J. van der Hagen,
voorzitter van het College voor Promoties,
in het openbaar te verdedigen op vrijdag 25 oktober 2024 om 12:30 uur

door

Wouter Anthonie CORNEL

Natuurkundig ingenieur
Technische Universiteit Delft, Nederland,
geboren te 's-Gravenzande.

Dit proefschrift is goedgekeurd door de promotoren.

Samenstelling promotiecommissie:

Rector Magnificus	Voorzitter
Prof. dr. ir. C. Poelma,	Technische Universiteit Delft, promotor
Prof. dr. ir. J. Westerweel	Technische Universiteit Delft, promotor

Onafhankelijke leden:

Prof. Dr.-Ing. J. Hussong	TU Darmstadt, Duitsland
Prof. dr. ir. J.A.M. Kuipers	Technische Universiteit Eindhoven
Prof. dr. ir. J.T. Padding	Technische Universiteit Delft
Prof. dr. ir. T.J.C van Terwisga	Technische Universiteit Delft
Prof. dr. ir. C.H. Venner	Universiteit Twente

This research is part of the public-private research programme Slashing of Liquefied Natural Gas (SLING) with project number P14-10 which is (partly) financed by the Netherlands Organisation for Scientific Research (NWO).



ISBN : 978-94-6496-228-4

Printed by : Gildeprint - Enschede

Copyright © 2024 by W.A. Cornel, all rights reserved

An electronic version of this dissertation is available at
<http://repository.tudelft.nl/>.

CONTENTS

Summary	vii
Samenvatting	ix
Preface	xiii
1 Introduction	1
1.1 Background	1
1.2 Gas/vapor-liquid compressibility	2
1.3 Objectives.	5
1.4 Research approach	5
1.5 Outline of the thesis.	7
2 Local micro-bubble concentration by defocused volumetric shadowgraphy with a single camera	11
2.1 Introduction	12
2.2 Imaging model	14
2.3 Bubble shape	15
2.4 Experimental facility and methods	15
2.5 Differential pressure reference measurements	18
2.6 Results	19
2.6.1 Calibration curve	19
2.6.2 Local bubble concentrations in bubble clouds.	19
2.6.3 Comparison of the z -position with reference camera	21
2.6.4 Comparison with differential pressure reference measurements.	21
2.7 Conclusion and Outlook	23
3 Non-intrusive imaging method for shock wave propagation in bubbly liquids	27
3.1 Introduction	28
3.2 Model description	30
3.3 Experimental set-up	33
3.3.1 Facility.	33
3.3.2 Bubble velocity by imaging	35
3.3.3 Shock wave front speed by imaging	36
3.3.4 Reference measurements by two-phase PIV	38
3.3.5 Reference measurements by pressure transducers	40
3.4 Results	41
3.5 Conclusions and Outlook	45

4	Energy partitioning of cloud cavitation collapses via time-resolved X-ray densitometry	49
4.1	Introduction	50
4.2	High-speed X-ray facility (HSX)	53
4.3	Data processing	57
4.3.1	Image data	57
4.3.2	Vapor volume of detached cavities	60
4.3.3	Pressure data	61
4.3.4	Synchronizing image and pressure data	64
4.4	Results	64
4.5	Discussion	70
4.6	Conclusion	75
5	Conclusion	83
5.1	Summary of the research findings.	83
5.1.1	Findings on the proposed experimental methods	83
5.1.2	Findings on emitted shock wave energy	84
5.2	Outlook	84
	Acknowledgements	89
	Curriculum Vitæ	93
	List of Publications	95

SUMMARY

Natural gas is one of the most important global energy sources, and is commonly transported in pipelines (in gaseous state) or specially-designed LNG vessels (in liquid state). As LNG is stored inside the ship cargo containment system at atmospheric pressure and low temperatures, just below the boiling point of circa $-162\text{ }^{\circ}\text{C}$ (depending on the composition), small perturbations in pressure or temperature may result in phase changes between the liquid and vapor phase. During transportation overseas, the motion of the ship induces movements of the LNG inside the containment system. Sloshing may result into wave impacts that potentially cause damage to the containment system. During these wave impacts, phase changes inside the LNG fluid domain are likely to occur, which alter the fluid properties locally. Insights into these phase changes during sloshing impacts are of key importance for the accurate, efficient and safe designs of cargo containment systems inside LNG vessels. The main objectives of this dissertation are twofold : (1) the development and validation of non-intrusive measurement techniques to characterize the propagation of shock waves through multiphase fluids, and (2) quantifying the energy partitioning and emission of shock waves by collapsing vapor bubble clouds. To this aim, two novel measurements techniques are developed and validated for accurately quantifying the two-phase liquid properties and the shock wave propagation, non-intrusively. Also, the emission of shock waves by collapsing vapor bubbles is assessed non-intrusively with state-of-the-art high-speed X-ray densitometry.

The vapor/gas volume concentration of a two-phase liquid is known to have significant effect on the compressibility of the two-phase liquid, and thus on the exerted impact loads by the impacting wave crest upon structures. Therefore, a non-intrusive measurement method on the local dilute vapor/gas fraction inside the fluid domain is developed and validated to characterize the fluid properties before impact loads acts upon the aerated liquid. Due to limited optical access to the measurement domain, only a single high-speed camera is used. The method is capable of extracting three-dimensional volumetric properties, based on defocused volumetric shadowgraphy. It is shown that the in-depth z -position of the bubble's center in a range of $\pm 2.5\text{ mm}$ around the focal plane proved accurate. Combined with (x, y) bubble cross-sectional data and measurement domain, the local vapor/gas fraction is retrieved. Two reference methods, based on the differential pressure ($\Phi_V = 0.081\% \pm 0.011$) and direct observation of the bubble's in-depth z -position by a second camera, both validate these results independently.

Subsequently, the propagation of shock waves propagating through the two-phase gas/water liquid is measured non-intrusively, solely from the gas bubble velocities. The proposed and validated imaging-based method allows to measure inside the fluid domain, and is thus not restricted to only measurements at the wall by flush-mounted intrusive pressure transducers. Also, the flow remains unaltered and no tracer particles are required. By comparing the relative motion between gas bubbles and applying split field-of-view (FOV), the shock wave front speed is measured. The shock wave pressure and shock-induced liquid velocity are computed with a hydrodynamic model, of which the shock wave speed is one of the inputs. Reference measurements show that the method provides accurate estimates for the shock wave speed (by FOV) and shock-induced velocity (by the model), while the shock wave pressure (also by the model) is more challenging.

Perturbations in pressure or temperature may cause the liquid (in thermodynamic equilibrium) to evaporate locally, and thereby forming vapor bubble clouds. Upon pressure recovery, these clouds collapse and emit strong transient shock waves. The final collapse stages are recorded with high-speed X-ray densitometry with sub-millimeter spatial and sub-millisecond temporal resolution, and are simultaneously recorded by high-frequency pressure transducers. By computing the initially-present cavity potential energy (E_{pot} from the X-ray images) and the shock wave energy (E_s from the pressure data), the energy conversion factor E_s/E_{pot} is quantified for various flow regimes, as characterized by the cavitation number and pressure (Ca, P_∞). On average, between 24 and 56 percent of the initial potential cavity energy E_{pot} is converted into shock wave energy E_s for cloud cavitation within the experimental range of $0.41 < Ca < 0.71$ and $35.9 < P_\infty < 71.0$ kPa. Also, the energy conversion factor E_s/E_{pot} , and the amount of E_{pot} and E_{sw} , increase for decreasing cavitation number by keeping kinetic energy added to the flow constant. More cavity potential energy is partitioned into shock wave energy for increasing surrounding pressures for constant cavitation number. The conversion factor E_s/E_{pot} varies significantly per individual cycles, which is most likely caused by the observed large cycle-to-cycle variance in the projected geometrical shapes of the vapor clouds. The observed discrepancy between E_{pot} and E_s cannot be fully explained by the potential energy conversion to rebound energy E_{reb} , internal energy U or other losses such as acoustic noise to the surroundings. We surmise that complex fluid mechanisms, such as the formation of impinging jets, are accountable for this energy discrepancy as suggested by Schenke *et al.* (2019).

This dissertation describes the developed and validated measurement techniques, together with the findings on energy partitioning and shock wave emission by collapsing cavitation clouds. Finally, directions for future research are presented based on these findings.

SAMENVATTING

Aardgas is een van de belangrijkste wereldwijde energiebronnen en wordt voornamelijk getransporteerd door pijpleidingen (in gasvormige toestand) of speciaal ontworpen LNG-schepen (in vloeibare toestand). Aangezien LNG (vloeibaar aardgas) wordt opgeslagen in de ladingtanks van LNG-schepen onder atmosferische druk en lage temperaturen, net onder het kookpunt van circa $-162\text{ }^{\circ}\text{C}$ (afhankelijk van de samenstelling), kunnen kleine verstoringen in druk of temperatuur leiden tot faseovergangen tussen de vloeistof- en dampfase. Gedurende het overzeese transport veroorzaakt de beweging van het schip tot het bewegen van de LNG in de ladingtanks. Het klotsen (sloshing) kan brekende golven veroorzaken die mogelijk de tankwanden kunnen beschadigen. Tijdens deze golf inslagen op de tankwanden is het waarschijnlijk dat fase-overgangen optreden, waardoor de vloeistofeigenschappen lokaal veranderen. Inzicht in deze faseovergangen tijdens de impact van klotsende golven zijn van cruciaal belang voor het nauwkeurig, efficiënt en veilig ontwerpen van de ladingtanks in LNG-schepen. Het doel van dit proefschrift is tweeledig: (1) het ontwerpen en valideren van niet-intrusieve meettechnieken om de voortbeweging van schokgolven door meerfasen-stroming te karakteriseren, en (2) het kwantificeren van de energieverdeling en emissie van schokgolven door imploderende dampbellenwolken. Om dit doel te bereiken zijn twee nieuwe niet-intrusieve meettechnieken ontwikkeld en gevalideerd voor het nauwkeurig meten van de tweefasen vloeistofeigenschappen en voor de voortbeweging van schokgolven. Ook is de emissie van schokgolven door imploderende dampbellen op niet-intrusieve wijze onderzocht met geavanceerde hogesnelheids-röntgendensitometrie.

Het is bekend dat de damp/gas volumeconcentratie in een tweefase vloeistof een significant effect heeft op de samendrukbaarheid van deze vloeistof, en derhalve ook op de uitgeoefende impact door de inslaande golftop op de tankwanden. Een niet-intrusieve meetmethode voor het bepalen van de lokale damp/gas fractie binnenin het vloeistofdomein is ontwikkeld en gevalideerd om de vloeistofeigenschappen te karakteriseren voordat de impact wordt uitgeoefend op de beluchte vloeistof. Vanwege de beperkte optische toegang tot het meetdomein wordt slechts één hogesnelheidscamera gebruikt. De meetmethode is in staat om drie-dimensionale volumetrische eigenschappen te bepalen, gebaseerd op onscherpe volumetrische 'shadowgraphy'. Het is aangetoond dat de diepte (z -positie) van het centrum van de bel nauwkeurig kan worden bepaald voor een afstand van $\pm 2.5\text{ mm}$ rondom het brandspuntvlak. Gecombineerd met de (x, y) dwarsdoor-

sneede van de bel en de afmetingen van het meetdomein is de lokale damp/gas fractie bepaald. Twee referentiemethoden, gebaseerd op het drukverschil ($\Phi_V = 0.081\% \pm 0.011$) en de directe waarneming van het middelpunt van de bel door een tweede camera, valideren beide deze resultaten onafhankelijk.

Vervolgens is de voortbeweging van schokgolven door een beluchte vloeistof niet-intrusief gemeten, uitsluitend door middel van de snelheid van de gasbellen. De voorgestelde en gevalideerde optische methode maakt het mogelijk om binnenin het vloeistofdomein te meten, en is dus niet beperkt tot slechts metingen aan de wanden zoals bij intrusieve druksensoren. Bovendien blijft de stroming ongewijzigd en zijn er geen tracerdeeltjes nodig. Door de relatieve beweging tussen gasbellen te vergelijken en een gesplitst gezichtsveld (FOV) toe te passen, wordt de frontsnelheid van de schokgolf gemeten. De schokgolfdruk en de door de schokgolf geïnduceerde vloeistofsnelheid worden berekend met een hydrodynamisch model, waarbij de schokgolfsnelheid één van de inputs is. Uit referentiemetingen blijkt dat deze methode nauwkeurige waarden geeft voor de schokgolfsnelheid (via FOV) en de schok-geïnduceerde vloeistofsnelheid (via het model), terwijl de schokgolfdruk (ook via het model) meer uitdagend is gebleken.

Verstoringsen in druk of temperatuur kunnen ertoe leiden dat de vloeistof (in thermodynamisch evenwicht) lokaal verdampt, waarbij dampbellenwolken ontstaan. Wanneer de druk zich herstelt, imploderen deze dampbellenwolken en zenden hierbij kortstondige, krachtige schokgolven uit. De laatste fase van de implosie is geregistreerd door middel van hogesnelheids-röntgendensitometrie met een ruimtelijke resolutie van minder dan een millimeter en een temporele resolutie van minder dan een milliseconde, en wordt tegelijkertijd geregistreerd met hoogfrequente druksensoren. Door de aanvankelijke aanwezige potentiële energie van de caviteit (E_{pot} , uit de röntgenbeelden) en de schokgolf-energie (E_s , uit de drukgegevens) te bepalen, wordt de energie conversie E_s/E_{pot} gekwantificeerd voor verschillende stromingsregimes, zoals gekarakteriseerd door het cavitatiegetal en de druk (Ca, P_∞). Gemiddeld wordt tussen 24 en 56 procent van de initiële potentiële energie E_{pot} omgezet in schokgolf-energie E_s voor dampwolcavitatie bij het experimentele bereik van $0.41 < Ca < 0.71$ en $35.9 < P_\infty < 71.0$ kPa. Ook nemen de energieconversiefactor E_s/E_{pot} en de hoeveelheid E_{pot} en E_s toe bij een afnemend cavitatiegetal, waarbij de toegevoegde kinetische energie aan de stroming constant is gehouden. Meer potentiële energie wordt verdeeld in schokgolfenergie voor toenemende omgevingsdruk bij een constant cavitatiegetal. De conversiefactor E_s/E_{pot} varieert aanzienlijk per individuele cyclus, wat hoogstwaarschijnlijk wordt veroorzaakt door geobserveerde grote variantie in cycli in de geprojecteerde geometrische vormen van de dampwolken. De waargenomen discrepantie tussen E_{pot} en E_s kan niet volledig worden verklaard door de potentiële energieconversie naar *rebound* energie E_{reb} , interne energie U of andere energieverliezen zoals akoestisch geluid naar de omgeving.

Derhalve wordt vermoed dat complexe vloeistofmechanismen, zoals de vorming van botsende jets, verantwoordelijk zijn voor dit energieverval, zoals gesuggereerd door Schenke et al. (2019).

Dit proefschrift beschrijft de ontwikkelde en gevalideerde meettechnieken, tesamen met de bevindingen over energiepartitionering en schokgolfemissie door imploderende cavitatie wolken. Tenslotte worden op basis van deze bevindingen aanbevelingen voor toekomstig onderzoek gepresenteerd.

PREFACE

The PhD research described in this thesis is performed as part of the SLING¹ research project to assess the sloshing physics and impact loads by disentangling the complex sloshing wave dynamics. The SLING research project is a public-private research program involving a large collaboration between industrial partners and academia. The research program intends to gain insight in the sloshing dynamics of LNG by structuring the research project into three thematic groups: multiphase dynamics, variability of impact loads, and structural response². These topics focus on different wave component or elementary load process (ELPs)³. Additionally, the research topics converge to form one overarching sloshing framework, combining all the acquired experimental and numerical findings. Both experimental and numerical research was performed by seven PhD candidates, two PDEng candidates and one post-doctoral researcher. Specifically, this dissertation focuses on the experimental investigation of the effect of two-phase liquid compressibility, i.e. the ‘stiffness’ of the fluid, on the liquid impact loads during sloshing, in presence and absence of phase transitions. Gas pockets, entrapped by the breaking waves, are explicitly taken out of the scope of this research, as being part of another research within the project. To this purpose, experiments were planned to be performed in an advanced autoclave (‘Atmosphere’)⁴ at research institute MARIN for optimally controlling the temperature and pressure. Due to limited optical access, measurements can only be conducted by a single high-speed camera. The experimental setup consists of submerged pistons to transfer momentum (by an impactor) directly to the single or two-phase liquid, to isolate the effect of direct impact without being affected by the impact of gas/vapor layer in between the piston and the free surface. Due to external construction delays and the effects of the Covid-19 global pandemic on the project, the originally planned experiments could unfortunately not have been conducted within the time frame of this funded PhD research. Alternatively, high-speed X-ray densitometry measurement on phase changes in cavitating flows were performed at TNO research institute in The Hague/Ypenburg. While these experiments did not use the previously

¹The project name SLING is an acronym for ‘Sloshing of Liquefied Natural Gas’.

²<https://www.marin.nl/en/jips/nwo-perspectief-sling>

³H. Bogaert, *An experimental investigation of sloshing impact physics in membrane LNG tanks on floating structures*, PhD thesis, TU Delft, 2018

⁴<https://www.marin.nl/en/about/facilities-and-tools/basins/atmosphere>

developed measurement techniques, the physical phenomena are adjacent to those of the original problem. Obtained experimental and processed data on two-phase liquid compressibility and impact loads by shock wave emission are used, in isolation or combined with experimental and numerical findings by other research participants within the SLING project, to develop and validate an overarching sloshing framework which allows for more efficient design procedures of LNG containment systems.

1

INTRODUCTION

1.1. BACKGROUND

Natural gas is one of the most important global energy sources and is commonly transported in pipelines or specially-designed LNG-vessels overseas. Liquefied natural gas (LNG) is sub-cooled natural gas in the liquid state, and can be stored inside cryogenic membrane tanks in LNG vessels at atmospheric pressure and very low temperatures. Depending on the actual composition of the natural gas, the boiling temperature is typically minus 162 degrees Celsius, which allows to reduce the cargo volume to approximately 1/600th of the gaseous volume at standard temperature and pressure. As of the end of April 2023, there are 668 LNG-vessels operational with an average capacity of 163 thousand cubic meter (IGU, 2023). Although LNG is a fossil fuel, LNG is a much cleaner alternative compared to heavy fuel oils or coal for energy production. LNG can be seen as a transition step towards clean energy production. By using synthetic e-LNG, produced with renewable energy and the circulation of carbon dioxide, the CO₂ emission for ship transportation reduces to nearly zero (TNO, 2020).

Sloshing of LNG during transportation overseas may lead to severe impact loads onto the ship containment system and the tank membranes, causing permanent damage to the cargo containment system and leading to safety concerns. For example, damage was observed to several locations of the containment system during an inspection of the LNG vessel Spirit of Catalunya in 2006, which indicated local over-pressure due to sloshing (Gavory & de Seze, 2009). Strict operational conditions prescribe the filling level of

the membrane tank, and require that the membrane tank may either be nearly filled or almost empty during transportation to reduce the sloshing impact loads onto the tank membrane walls (Det Norske Veritas, 2006; Lloyd's Register, 2009). However, to enhance the flexibility in LNG distribution, it is desired to operate vessels with partially filled LNG membrane tanks as well, allowing to load and unload at multiple locations. Also, since sub-cooled LNG is stored at atmospheric pressure and close to the thermodynamic equilibrium with its gas phase inside the containment tanks (Hicks, 2018), small transient perturbations in temperature or pressure may lead to local phase transitions, such as boiling and cavitation. This affects the fluid properties considerably. Particularly for cryogenic liquids such as LNG, phase transitions complicate the physics of sloshing, because local flow regions may spontaneously change due to the transition from liquid to gas and vice versa. Understanding these physics of sloshing in combination with the effects of local phase transitions during impact loads on the membrane walls is key for safe transportation, but not yet well understood.



Figure 1.1: LNG vessel (left) [obtained from Mokhatab *et al.*, Handbook of Liquefied Natural Gas, 2014], and cargo containment system (right) [obtained from GTT.fr].

1.2. GAS/VAPOR-LIQUID COMPRESSIBILITY

The impact loads exerted by impacting liquids on structures strongly depend on the compressibility of the single liquid or two-phase gas/vapor-liquid. The inertia of the flow is mainly attributed to the density of the liquid phase ρ_l , while the compressibility of the two-phase flow is mainly attributed to the gas/vapor phase. Adding gas or vapor bubbles to the liquid increases the compressibility of the mixture and lowers the acoustic wave speed c . The pressure exerted by an impacting liquid onto structures can be approximated by the Joukovsky equation (i.e. water hammer equation), $\Delta P = \rho c \Delta v$, which is derived from Newton's second law of motion. This equation states that the change in pressure ΔP is proportional to the density of the liquid ρ , the acoustic wave speed through the medium c , and the transient change in liquid velocity Δv . For example, in case of breaking waves on non-moving solid structures, Δv is the incoming velocity of

the breaking wave tip. For single-phase liquids, by approximation $c = \sqrt{dP/d\rho} = \sqrt{K/\rho}$ for an infinite reservoir, where $K = \rho(dP/d\rho) = \rho c^2$ represents the bulk modulus. The compressibility is the reciprocal of the bulk modulus, i.e. $\kappa = 1/K$. Note that also containment walls (with finite stiffness) may also have an effect on the compressibility κ , because they may also compress in responds to a pressure wave. This is important for an experimental setup with flexible tube wall ($\kappa_{wall} > 0$), where the acoustic wave speed in the confined pure liquid is lower than the acoustic wave speed in infinite reservoirs, which are assumed to have infinite stiff boundaries (i.e. $\kappa \rightarrow 0$).

The presence of gas/vapor bubbles and their dynamics complicates the problem significantly. By adding gas or vapor bubbles to the single-phase liquid, the density is reduced to $\rho = (1 - \alpha)\rho_l + \alpha\rho_g$, where α is the volumetric vapor or gas fraction (i.e. the volume not occupied by liquid). For example, $\alpha = 0$ retrieves the density for a single-phase liquid in absence of vapor or gas, while $\alpha = 1$ represents solely vapor/gas. Since $\rho_g \ll \rho_l$, the mixture density can be approximated by $\rho \approx (1 - \alpha)\rho_l$. Gas/vapor bubbles enhance the compressibility of the mixture, which lowers acoustic wave speeds drastically (Watanabe & Prosperetti, 1994). This compressibility is more sensitive to the volumetric vapor/gas fraction compared to the density, even for small bubble concentrations. Historically, several expressions for the acoustic wave speed through an aerated liquid have been proposed in the academic literature. By assuming a homogeneous mixture with bulk density and compressibility, Wood (1941) expressed the acoustic speed of sound in an aerated liquid as:

$$\frac{1}{\rho c^2} = \frac{1 - \alpha}{\rho_l c_l^2} + \frac{\alpha}{\rho_g c_g^2} \quad (1.1)$$

where c_l and c_g are the acoustic speed of sound in pure liquid and gas, respectively. Bubble dynamics and interaction between bubbles are not taken into account in this expression. This expression shows that even for small aeration levels ($\mathcal{O}(1\%)$), the acoustic wave speed reduces significantly to 129 m/s, compared to 1481 m/s for single-phase water. This has a significant effect on the impact load ΔP . For example, during the world record for cliff diving in 2015, the water was aerated to lessen the impact by the water onto the diver while hitting the water surface with a velocity of 120 km/h (SBPM, 2021). In this situation, the aeration significantly reduces the acoustic wave speed and slightly lowers the mixture density, and thus lowering the impact load.

Historically, the propagation of shock waves in dilute bubbly liquids were studied extensively due to the scientific and engineering relevance, both experimentally (Kameda

et al., 1998; Noordzij & Van Wijngaarden, 1974) and numerically (Ando, Colonius, et al., 2011; Delale & Tryggvason, 2008; Drumheller et al., 1982). Commonly, these experiments are conducted in vertical confined tubes, in which shock waves are generated by free-falling impact pistons (Ando, Sanada, et al., 2011) or a diaphragm rupture mechanism (Kameda et al., 1998; Miyazaki et al., 1971). Campbell et al. (1958) confirmed experimentally that the shock wave propagation speed depends on the volume of gas in the mixture and on the shock strength. Impact tests were performed to investigate the gradual change in the structure of shock waves travelling through bubbly liquids and the existence of three types of shock waves (Noordzij & Van Wijngaarden, 1974), and the effect of different gas compressibility (Beylich & Gulhan, 1990). By obtaining a uniform spatial distribution of non-condensable gas bubbles, Kameda et al. (1998) found that the experimental results were in good quantitative agreement with a model that they proposed. However, despite the vast amount of research, the majority of studies concerns water/air mixtures under standard conditions in absence of phase changes.

The effect of phase change by boiling or cavitation on the exerted pressure by the impacting liquid, which may occur due to (small) perturbations in temperature or pressure when the (two-phase) fluid is close to thermodynamic equilibrium, is still underexposed in literature. These phase transitions from liquid to vapor (vaporization) and from vapor to liquid (condensation) further complicates the sloshing physics and impact loads, as the compressibility of the (two-phase) fluid may change significantly, both locally and temporarily. Transient changes in the local pressure, upon impact, may cause rapid local vaporization and condensation inside the fluid domain, which may have an effect on impact loads exerted by the liquid on solid structures. Once the rarefaction wave passes, which trails the compression shock wave, the local pressure may drop below the vapor pressure. The sudden appearance of vapor bubbles is likely to cause a cushioning effect and thus dampening the impact load. This cushioning effect appears as the local compressibility strongly increases as a result of the large amount of vapor bubbles. Shock waves, which propagate through fluid regions with relatively large vapor fractions, have significantly lower wave speeds (Büdich et al., 2018; Gawandalkar & Poelma, 2022).

Once the rarefaction wave has passed and the local pressure recovers, vapor bubbles may collapse in isolation or collectively as a cloud. Under certain conditions, single vapor bubbles collectively act as a coherent bubble cloud, where the natural frequency approximates the cloud structure (Reisman et al., 1998; Wang & Brennen, 1995). During the implosion process, initial potential cavity energy is converted into liquid kinetic energy.

Once the inward accelerating liquid collides, part of the kinetic energy is subsequently converted into shock wave energy (Tinguely et al., 2012). It is shown that collapsing vapor bubbles are able to emit strong propagating shock waves through the liquid domain (Chen et al., 2015). The collapse of vapor bubble clouds, consisting of many interacting vapor bubbles in close proximity of each other, have been investigated extensively in cavitating flows around hydrofoils, near wedges, venturis and backward steps. Typically, these phenomena occur at time scales < 0.1 ms, which results in steep pressure gradients. To illustrate, the estimated pressure magnitude is approximately 0.5 MPa over a 10 mm distance from the center of a collapsing isolated vapor bubble with a 5 mm radius, in an infinite reservoir with wave speed of $U_s \approx 1480$ m/s, based on a conversion factor $E_s/E_{pot} = 0.60$ (discussed in detail in Chapter 4); this yields a pressure variation of approximately 1.8 GPa/s.

The occurrence of emitted shock waves and the enhanced mixture compressibility due to local rapid evaporation, caused by phase changes within the liquid domain upon wave impact, combined with non-condensable gas bubbles mixed due to sloshing, may exert additional loads upon solid structure. During the overseas transportation of LNG, these phenomena are likely to occur. Understanding their contribution, both in isolated and combined, to the impact load is essential to approach the complex sloshing dynamics. These combined effects are not yet known, but are essential for accurate modeling of impact loads for sub-cooled LNG. This research attempts to fill this gap in the academic literature.

1.3. OBJECTIVES

The main objectives of this dissertation are twofold : (1) the development and validation of non-intrusive measurement techniques to characterize the propagation of shock waves through multiphase fluids, and (2) quantifying the energy partition and emission of shock waves in the process of collapsing vapor bubble clouds.

1.4. RESEARCH APPROACH

The measurements are performed in a vertical confined tube with highly-controlled aeration levels, ambient pressure and temperature. Except for the secondary flow induced by the rising vapor/ gas bubbles, the liquid phase is stagnant. A submerged piston, representing the membrane wall, causes a shock wave (i.e. a finite-amplitude pressure wave) propagating through the two-phase liquid; see Figure 1.2. The force exerted by the liquid

onto the impacting piston, the liquid properties (local aeration, temperature and pressure), the propagation of shock waves, and gas/vapor bubble dynamics are measured accurately. By systematically varying each of these experimental conditions, the effects of each of these properties on the impact loads can be determined. The submerged piston is specifically designed to exclude the formation of an entrapped gas layer.

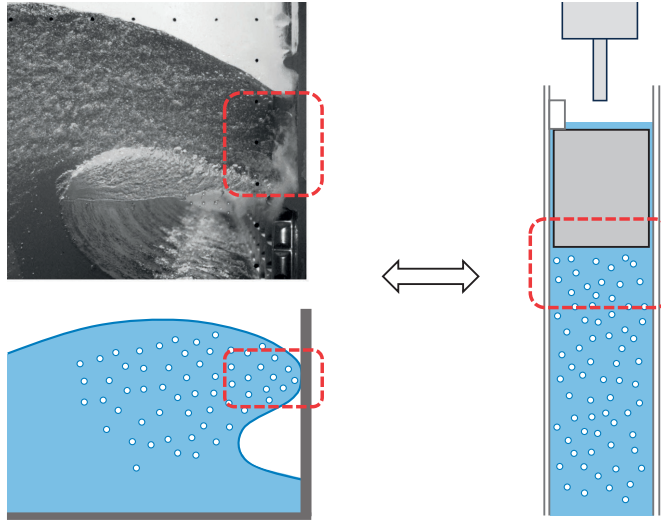


Figure 1.2: Image of an impacting wave crest on a structure (top-left, obtained from Bogaert (2018)), the schematic representation of the impacting wave crest (bottom-left), and the experimental setup to study these impacts for well-specified and controllable experimental conditions (right).

This research is motivated by the need to study transient phenomena in the multiphase fluid and track propagating shock waves non-intrusively, and can directly be applied to other demanding environments. The experimental challenge was to retrieve shock wave characteristics (wave speed, pressure magnitude, and shock-induced liquid velocity) from high-speed camera recordings. A split field-of-view (FOV) was introduced that enhances the accuracy of wave speed measurements significantly. As bubbles are naturally present in aerated liquids, this method is truly non-intrusive and no additional equipment is required. Both novel experimental techniques are designed and validated at the Laboratory for Aero & Hydrodynamics at the TU Delft.

A convergent-divergent channel (i.e. venturi) is used to generate controllable phase

changes in the cavitating flow. Cavitation occurs when the local pressure in the liquid phase drops below the vapor pressure, causing liquid to vaporize and form vapor bubbles within the liquid. Upon pressure recovery, these vapor bubble clouds collapse by rapid condensation and emit shock waves during the final collapse. The shock waves imply impact loads on nearby solid structures. The energy conversion between initial potential vapor energy and emitted shock wave energy is studied to estimate the expected pressure loads on solid structures, based on the initially present amount of vapor and local flow conditions. The amount of initial potential energy of the vapor bubbles and the geometric evolution of the vapor bubble clouds is measured via high-speed X-ray densitometry with sub-millimeter spatial and sub-millisecond temporal resolution under various flow conditions. Synchronized pressure transducers are employed to simultaneously quantify the emitted shock wave energies emitted by the vapor cloud collapse, which directly translates to impact loads. Detailed insights in the energy conversion from potential vapor energy to shock wave energy can be used to estimate what flow conditions may result in critical threshold conditions that may lead to undesired operational conditions, and to validate numerical studies.

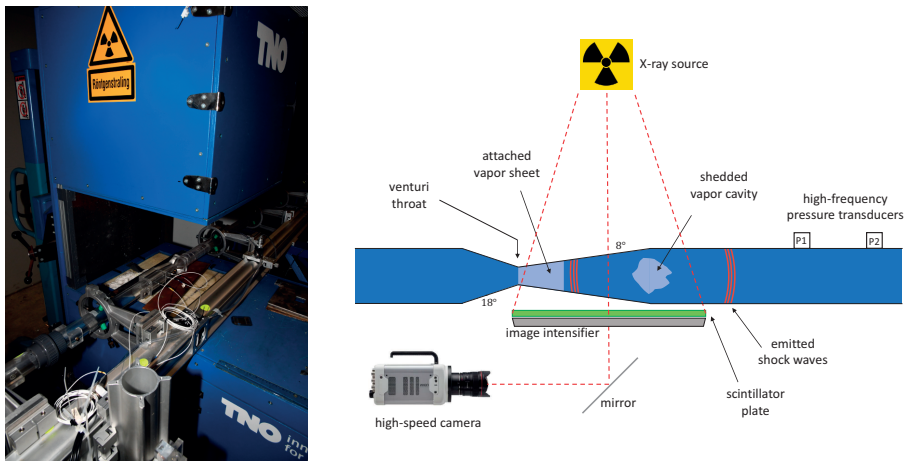


Figure 1.3: Picture (left) and schematic overview (right) of the measurement section of the X-ray densitometry setup at TNO (not to scale). The photo is cordially provided by Frits Hilvers (TNO).

1.5. OUTLINE OF THE THESIS

This thesis is structured as follows: Chapter 2 presents an experimental method that has been developed to measure detailed two-phase fluid properties, such as bubble sizes and void fraction, by recording local three-dimensional volumetric bubble concentra-

tions from individual shadowgraph images. Accurate local volumetric vapor/gas fractions are important to determine the local fluid density, and the effects on bubble concentration and distributions on the shock wave propagation through the aerated liquid. In Chapter 3, another imaging technique is presented and validated that deduces shock wave characteristics from the velocities of gas bubbles during shock wave passages. Both approaches are non-intrusive methods and can be applied to situations where the insertion of measurement probes is not possible or undesirable. Chapter 4 describes experiments on cloud cavitation with time-resolved X-ray densitometry measurements, performed at TNO (location Ypenburg-The Hague), to study the emitted shock waves by collapsing vapor bubble clouds for different sets of cavitation numbers and system pressures. Main conclusions of this thesis are presented in Chapter 5. Also, this final chapter includes an outlook for future research directions to possibly answer remaining open research questions.

BIBLIOGRAPHY

- Ando, K., Colonius, T., & Brennen, C. E. (2011). Numerical simulation of shock propagation in a polydisperse bubbly liquid. *Int. J. Multiph. Flow*, 37(6), 596–608.
- Ando, K., Sanada, T., Inaba, K., Damazo, J. S., Shepherd, J. E., Colonius, T., & Brennen, C. E. (2011). Shock propagation through a bubbly liquid in a deformable tube. *J. Fluid Mech.*, 671, 339–363.
- Beylich, A. E., & Gulhan, A. (1990). On the structure of nonlinear waves in liquids with gas bubbles. *Physics of Fluids A: Fluid Dynamics*, 2(8), 1412–1428.
- Bogaert, H. (2018). *An experimental investigation of sloshing impact physics in membrane LNG tanks on floating structures* (Doctoral dissertation). TU Delft.
- Büdich, B., Schmidt, S. J., & Adams, N. A. (2018). Numerical simulation and analysis of condensation shocks in cavitating flow. *J. Fluid Mech.*, 838, 759–813.
- Campbell, I. J., Pitcher, A. S., & Temple, G. F. J. (1958). Shock waves in a liquid containing gas bubbles. *Proc R Soc Lon Ser-A*, 243(1235), 534–545.
- Chen, G., Wang, G., Hu, C., Huang, B., Gao, Y., & Zhang, M. (2015). Combined experimental and computational investigation of cavitation evolution and excited pressure fluctuation in a convergent–divergent channel. *Int. J. Multiphase Flow*, 72, 133–140.
- Delale, C. F., & Tryggvason, G. (2008). Shock structure in bubbly liquids: Comparison of direct numerical simulations and model equations. *Shock Waves*, 17(6), 433–440.
- Det Norske Veritas, D. N. V. (2006). Sloshing analysis of LNG membrane tanks. *Classification Notes*, (30.9), 12.
- Drumheller, D. S., Kipp, M. E., & Bedford, A. (1982). Transient wave propagation in bubbly liquids. *J. Fluid Mech.*, 119, 347–365.
- Gavory, T., & de Seze, P. (2009). *Sloshing In Membrane LNG Carriers And Its Consequences From a Designer's Perspective*.
- Gawandalkar, U., & Poelma, C. (2022). The structure of near-wall re-entrant flow and its influence on cloud cavitation instability. *Exp. Fluids*, 63(5), 77.
- Hicks, P. D. (2018). LNG-solid impacts with gas cushioning and phase change. *Journal of Fluids and Structures*, 80, 22–36.
- IGU. (2023). *World LNG report 2023* (tech. rep.). International Gas Union.
- Kameda, M., Shimauro, N., Higashino, E., & Matsumoto, Y. (1998). Shock waves in a uniform bubbly flow. *Phys. Fluids*, 10(10), 2661–2668.
- Lloyd's Register, L. R. (2009). *Sloshing assessment guidance document for membrane tank LNG operations: Guidance notes* (tech. rep.).

- Miyazaki, K., Fujii-EE, Y., & Suita, T. (1971). Propagation of pressure wave in air-water two-phase system. *J. Nucl. Sci. Technol.*, 8(11), 606–613.
- Noordzij, L., & Van Wijngaarden, L. (1974). Relaxation effects, caused by relative motion, on shock waves in gas-bubble/liquid mixtures. *J. Fluid Mech.*, 66(1), 115–143.
- Reisman, G. E., Wang, Y.-C., & Brennen, C. E. (1998). Observations of shock waves in cloud cavitation. *J. Fluid Mech.*, 355, 255–283.
- SBPM. (2021). *New cliff diving world record set in switzerland* (tech. rep.). Seattle Back Packers Magazine.
- Tinguely, M., Obreschkow, D., Kobel, P., Dorsaz, N., de Bosset, A., & Farhat, M. (2012). Energy partition at the collapse of spherical cavitation bubbles. *Phys. Rev. E*, 86(4), 046315.
- TNO. (2020). *E-fuels cruciaal voor verduurzaming zwaar transport* (tech. rep.). TNO.
- Wang, Y.-C., & Brennen, C. E. (1995). The Noise Generated by the Collapse of a Cloud of Cavitation Bubbles. *Cavitation and gas-liquid flow in fluid machinery devices* (pp. 17–29). ASME.
- Watanabe, M., & Prosperetti, A. (1994). Shock waves in dilute bubbly liquids. *J. Fluid Mech.*, 274, 349–381.
- Wood, A. (1941). *A textbook of sound*. G. Bell; Sons.

2

LOCAL MICRO-BUBBLE CONCENTRATION BY DEFOCUSED VOLUMETRIC SHADOWGRAPHY WITH A SINGLE CAMERA

The challenge presented in this chapter is to determine the local volumetric bubble concentration (or void fraction) in the center of a micro-bubble cloud with limited optical access and without disturbing the flow. By applying defocused volumetric shadowgraphy to an aerated water column we are able to measure the characteristics of single micro-bubbles in the control volume for a void fraction of up to 0.078 percent. The time-averaged local bubble concentration in the center of the water column is measured over four periods (800 seconds each) to investigate the repeatability. Two reference methods are applied, based on differential pressure ($\Phi_V = 0.081 \text{ percent} \pm 0.011$) and direct observation of the bubble's in-depth z -position, both validate the results independently.

Parts of this chapter were published in : W.A. Cornel, J. Westerweel, C. Poelma, "Local micro-bubble concentration by defocused volumetric shadowgraphy with a single camera", *Proceedings 18th International Symposium on Flow Visualization*, ETH Zürich, 2018

2.1. INTRODUCTION

The presence of micro-bubbles in fluids has considerable effects on the two-phase liquid compressibility and thus the speed of sound, even for moderate volume fractions. Micro-bubbles are small compressible gas bubbles with typical diameters between $1\ \mu\text{m}$ and $1\ \text{mm}$. Knowledge of the local volumetric bubble concentration (or void fraction) is of key importance in several industrial processes, such as the production of ammonia and water waste treatment (Dehaeck et al., 2009) Especially for industrial processes exposed to elevated pressures and temperatures, such as fuel injectors, access to the region of interest in the flow can be difficult. Furthermore, the flow phenomena of interest might be locally disturbed by the presence of intrusive measurement sensors.

Direct imaging methods are non-intrusive, have the ability to characterize particle shape in great detail and are relatively inexpensive (Lee et al., 2009; Legrand et al., 2016). Shadowgraphy or back-lighting has the advantages offered by digital imaging methods such as visualization of objects in high spatial resolution, identification of particle images and extraction of their characteristics (Pu et al., 2005). Also, this measurement method is robust for bubbles as no random dust particles are falsely detected (Dehaeck et al., 2009). In fact, the main disadvantage of shadowgraphy is the loss of depth information when objects are projected on a two-dimensional image. Therefore, many of the proposed imaging techniques for volumetric measurements use multiple cameras to construct a three-dimensional space. However, some articles in literature report imaging techniques for 3D particle positioning based on a *single* camera. Combining shadowgraphy with defocused imaging enables the acquisition of depth information by the degree of out-of-focus from a single camera. Using this principle, the distance from the focus plane is derived from determining the image intensity gradient, or blurriness, over the bubbles' edges. The idea of using focal gradient to infer depth from images was introduced by Pentland (1987). He examined the focal gradients resulting from the limited depth of field inherent in optical systems as a useful source of depth information. By measuring the error in focus (i.e. focal gradient) the depth in the image can be estimated.

In recent years many researchers elaborated on defocused shadowgraphy to determine locations and sizes for synthetic particles (Lebrun et al., 1993; Lecuona et al., 2000; Willert & Gharib, 1992), larger gas bubbles (Bröder & Sommerfeld, 2007) and dense sprays (J. B. Blaisot & Yon, 2005; J.-B. Blaisot & Ledoux, 1998; Buraga-Lefebvre et al., 2000; Fdida & Blaisot, 2009; Legrand et al., 2016; Malot & Blaisot, 2000). Lebrun et al. (1993) used two CCD cameras with the same angle of view to deduce particle diameters from the im-

age contrast and the cross-section areas of the defocused images. More recently, Bröder and Sommerfeld (2007) developed an interesting planar defocusing imaging technique for the analysis of the hydrodynamics in bubbly flows based on the intensity gradient to define the depth of field of the imaging plane for bubble diameters between 2.0 and 4.0 mm. The intensity gradient over the boundary of the micro-bubble in the image, or blurriness, contains information on the in-field depth position z relative to the object focal plane. Fdida and Blaisot (2009) used the calibration of the point spread function (PSF) to determine the drop size distribution by counting drops. Malot and Blaisot (2000) developed an imaging model based on the point spread function to determine the drop size distributions of sprays produced by low-velocity plain cylindrical jets. Wavelet transforms, based on the PSE, are constructed to perform hologram analysis (Buraga-Lefebvre et al., 2000; Pu et al., 2005). The study of Ren et al. (1996) shows that corrections for the estimated diameters are less significant for larger particles. Digital pattern recognition algorithms deliver accurate and robust results as the projected particles are close to circular. Lee et al. (2009) developed a modified in-focus parameter based upon optical principles to identify particles. Their adaptive sampling volume methodology varies with each particle size based upon a critical in-focus value. By linking particle depth location to the circle of confusion (COC), determined from the gray scale gradients of the 2D image profile and from image contrast considerations, Legrand et al. (2016) obtained less than 20 percent in particle sizing with displacements up to 30 particle diameters away from the focus plane.

Closely related to defocused volumetric imaging is defocused digital particle image velocimetry (DDPIV) where flow fields of tracer particles are measured (Pereira & Gharib, 2002). For example, Willert and Gharib (1992) proposed a new approach to track particles in space and time by using defocusing and an embedded mask in the camera lens to observe triangular patterns. Dehaeck et al. (2009) proposed an alternative method to locate depth from 2D-images which combines back-lighting and glare point velocimetry. Only bubbles inside the thin laser sheet have two symmetrical glare points, so that the control volume is well-defined. The laser sheet needs to be perpendicular to the optical access, which makes this method unsuitable for cases with limited optical access.

In this research, we further elaborate on defocused volumetric shadowgraphy by extending it to smaller compressible gas micro-bubbles with typical mean diameter of 0.6 mm and apply Circular Hough Transform (CHT) and Sobel edge detection for bubble shape recognition. The objective of this paper is to propose a method, based on intensity gradi-

ents, to measure bubble concentrations in aerated liquids locally from images captured by one single camera. As smaller droplets and dense sprays (typical particle size $< 100 \mu\text{m}$) and larger bubbles (with typical diameters $> 2.0 \text{ mm}$) are studied extensively over recent years, only limited literature is publicly available for micro-bubbles with diameters smaller than 1 millimeters. These micro-bubbles have the advantages of having a relative large surface to volume and approximate sphericity which allows for precise volumetric determination. We employ defocused volumetric shadowgraphy to acquire bubble size distribution and locations accurately. The bubble z -position is relative to the focus plane and thus the measurement volume is well-defined. On the other, the *sign* of the relative distance from the focus plane cannot be traced back from the images. Therefore, it is possible to determine precisely if bubbles are located within a specified control volume, only we do not know whether the bubbles are located in front or behind the focus plane (Legrand et al., 2016). A second advantage of defocused imaging is the ability to measure bubble characteristics, such as bubble volume, since the observed gas bubbles have sharp contours in the focus plane.

The outline of this chapter is as follows: The next section describes the imaging model and point spread function which approaches the defocused intensity profile of the image. From this, the experimental setup, methodology and calibration procedure are described. The result section discusses the measured bubble concentrations for the center of a bubble cloud and compares the findings with the two validation techniques. The last section concludes the proposed method and provides an outlook for future research directions.

2.2. IMAGING MODEL

An optical imaging system with back-light illumination is used in this research; see Fig. 2.1. The intensity distribution in the image is the convolution of the point spread function (PSF), i.e. the system response, and the object function (Lebrun et al., 1993). The shape of the PSF can be approximated by a Gaussian function for non-coherent polychromatic light and that the PSF depends on the relative distance between the focus plane and the object (Fdida & Blaisot, 2009; Pentland, 1987). The Gaussian function flattens out for particles further located away from the focus plane, i.e. the object projection of the image plane becomes increasingly blurred. Consequently, the intensity gradient of the edge between the projected object and the background decreases too. The contribution of non-spherical aberrations is assumed to be negligible by imposing the PSF to have a generic symmetrical Gaussian shape (J.-B. Blaisot & Ledoux, 1998).

2.3. BUBBLE SHAPE

The degree of bubble sphericity depends on the dimensionless Eötvös (or Bond) number, Morton number and the Reynolds number, for which the bubble shape regimes are indicated by the Grace diagram. The Eötvös number compares the gravitational force ($\rho g L^3$) with the surface force (σL), while the Reynolds number is the ratio of inertia to viscous forces. The Morton number ($g\mu^4/\rho\sigma^3$) follows from a dimensional analysis on the motion of air bubbles in liquids, and can be reformulated as $We^3/(Re^4Fr^2)$, where the Weber number We describes the ratio of inertia to surface forces and the Froude number Fr is the ratio of inertia to gravity. Micro-bubbles, with typical diameters of 600 μm in water (depth ≈ 0.5 m) under standard conditions, approach sphericity as the surface tension dominates over the gravitational force. For these dimensionless numbers, the Grace diagram indicates that bubbles are located far into the spherical regime. Sphericity is an important bubble characteristic that enables us to expand the projected two-dimensional bubble into the three-dimensional space accurately. Especially for larger gas bubbles, which may become irregular wobbling as the relative influence of the surface tension lowers, determining the volume from projected images may become more challenging.

2.4. EXPERIMENTAL FACILITY AND METHODS

In this work, defocused shadowgraphy is used to estimate the depth of objects in single 2D-images captured by a single camera. Basically, the object's (x,y) -coordinates are directly available by processing the calibrated 2D-images correctly, while the z -coordinates follow from the amount of defocusing or blurring. An experimental setup has been constructed to generate an aerated liquid; see Fig. 2.1. A static water column with a height of 1.30 meter and width of 110 mm, filled with filtered tap water, has optical access provided by two opposing windows, where the camera optical axis is aligned with a LED panel for diffuse incoherent back-light illumination. Two fine-pore aerators (Pentair) are installed at the bottom of the water column and generate adjustable gas bubble clouds with bubble diameters between 500 and 900 μm . Thus, typical particle sizes are much larger than the wavelength of the incoherent light (i.e. $D/\lambda \gg 1$). Two reference measurement methods are added to validate the observed depth position by the single camera. First, a reference camera is installed, perpendicular to the optical axis of the main camera, to validate the bubble position in the y,z -plane. This way, the z -coordinate is observed directly. Secondly, the void fraction is measured globally by the pressure difference over the aerated liquid and a reference water column.

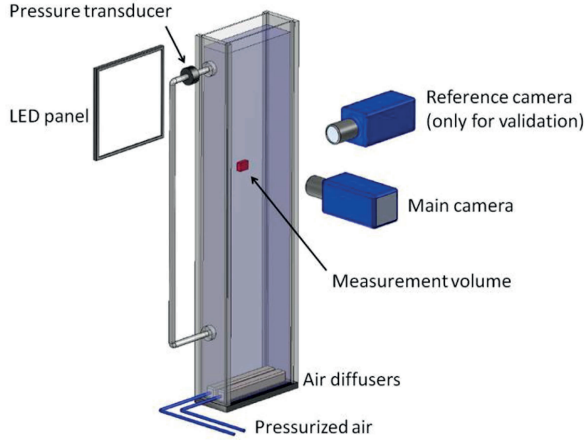


Figure 2.1: Systematic overview of the experimental setup (not to scale). The measurement volume (red rectangular) is aligned between the center line of the LED panel and the main camera. Two air diffusers ($300 \times 40 \times 40 \text{ mm}^3$) are installed at the bottom and connected to pressurized air. The differential pressure transducer and the reference camera serve as validation methods.

The PSF describes the complete, quantitative response of the optical system (Fdida & Blaisot, 2009). The response is determined experimentally by attached bubbles on the calibration sheet. The calibration is performed by recording multiple images of the calibration sheet, with attached micro-bubbles and spacing markers, by translating the CCD camera (LaVision Imager Intense), equipped with a 105 mm objective (Nikkor), in steps between $50 \mu\text{m}$ (near the object focal plane) and $400 \mu\text{m}$ (further away). The aperture of the objective ($f^\#$) is set to 4 to obtain a small depth of field. The 12-bit grey level frame images are sized 1040×1376 pixels. For each image, the magnitude of the intensity gradient of the attached bubble is measured to construct a calibration curve, which relates the magnitude of the image intensity gradient and the distance from the focal plane; see Fig. 2.4.

Once the imaging system is calibrated and the calibration sheet is removed, a bubble cloud of approximately $110 \times 300 \text{ mm}^2$ in cross-section is generated when releasing compressed air through the fine-pore aerators at the bottom of the water column. Contrary to the calibration procedure, the unbounded bubbles are moving towards the free surface. Motion blur, the effect that moving objects are smeared out over their trajectory path, might cause blurred edges too. In order to reduce motion blur in the image, the exposure time is set to $50 \mu\text{s}$ during the entire experiment. The image pixel resolution is 0.01086 mm/pixel , corresponding to a field of view of $14.9 \times 11.3 \text{ mm}$. Assuming an average bubble rising velocity of 100 mm/s , the travelled distance during exposure of the camera is $5.0 \mu\text{m}$, or 0.5 pixels. The control volume has dimensions of $10 \times 8 \times 5 \text{ mm}^3$ (L

$\times W \times H$) and centered in the middle of the bubble cloud (see Fig. 2.1). During the experiments, the camera and objective settings (i.e. aperture, focal length, exposure time) are constant and the frame rate is set to 0.5 Hz.

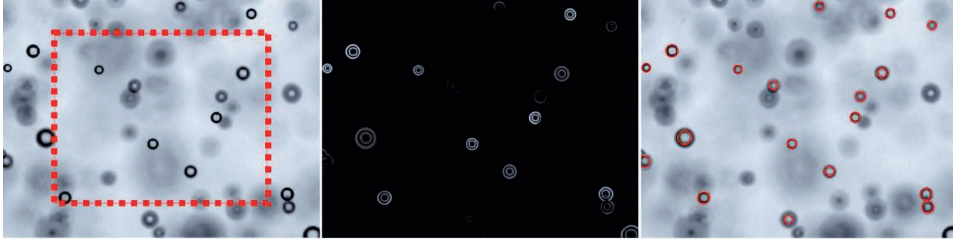


Figure 2.2: Unprocessed image with projected control volume (left), magnitude of the intensity gradient (center), and detected bubbles (right) for the same image. The center image is used for detecting the (x,y) -coordinates of the projected bubble location.

The micro-bubble detection procedure is based on the Circular Hough Transform (CHT) and Sobel edge detection from the MATLAB image processing toolbox, in combination with own modifications. First, the recorded raw images from the camera are smoothed by a Gaussian filter to remove the high spatial frequency originated from the stochastic nature of incoming photons at the camera sensor. Smoothing the raw images has the advantages of uncovering the intensity profile of the bubbles freed from background noise. The PSF is determined experimentally from the intensity gradient in the filtered image. To further improve the robustness of the proposed method, the intensity gradient is determined over four directions and the median is used to determine the out-of-focus distance. This additional robustness step ensures that no single outlier causes incorrect values. Also, the direction of the gradient is used to separate the inner and outer edge of the dark circle. As both the calibration and measurements are processed with the same procedure, the intensity gradients are matched and the depth position is obtained from the calibration.

This intensity gradient-based method does not require thresholding to identify objects, because the intensity gradient is directly related to the out-of-focus distance to the focal plane. However, it becomes increasingly difficult to characterize for defocused bubbles far away from the focal plane. Therefore, only sharp-contoured bubbles are evaluated, which are positioned relatively closely to the focal plane. The sensitivity of the CHT is set to be able to detect bubbles at an absolute distance of 4.0 mm from the focal plane. To avoid missing bubbles at the edge of the control volume due to not being recognized by the CHT, the control volume has an absolute depth distance of 2.5 mm, to ensure

that all qualified bubbles are detected. Individual bubble volumes are estimated by the equivalent spherical bubble diameter, where the bubble radius is the distance from the identified bubble center to the bubble edge, as defined by the location median of the four maximum edge intensity gradients. In the final step, void fractions Φ_V are computed per image by summing up the volumes of single bubbles over the control volume. The total average void fraction $\langle \Phi_V \rangle$ is the average of the void fractions per image.

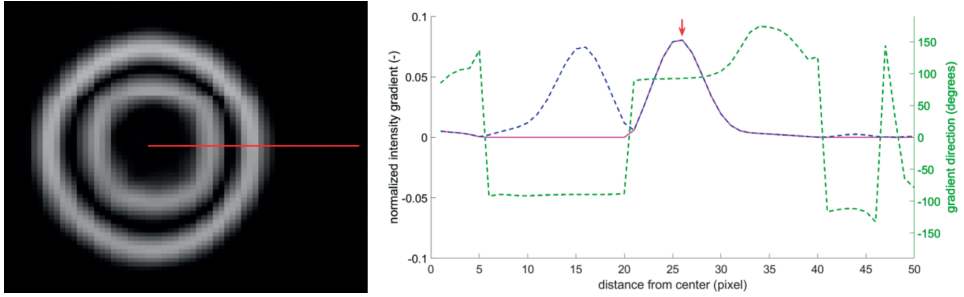


Figure 2.3: Left: the red line represents one of the four intensity profiles over the edge of the bubble. Right: the direction of the gradient (dotted green line) ensures that the outer circle is selected by zeroing the intensity gradient for negative angles (magenta line).

2.5. DIFFERENTIAL PRESSURE REFERENCE MEASUREMENTS

A reference differential pressure measurement is performed in order to validate the measured bubble concentration in the control volume. The injected bubbles lower the effective density and thus reducing the hydro-static pressure; see Fig. 2.1. Even through the bubble concentrations are low ($\Phi_V \ll 1$), the differential pressure sensor is able to measure accurately the pressure difference between the single-phase and the aerated water column. The pressure drop over the test section consists of the static head and the wall friction, of which the latter depends on the Reynolds number. For the single-phase case the water is stagnant, while the induced liquid velocity by the rising gas bubbles is assumed to be negligible. Therefore, the effect of the main contribution of the pressure difference for aerated liquids is (Poelma, 2004):

$$\Delta P = \rho_g \Phi_V g H + \rho_l (1 - \Phi_V) g H - \rho_l g H \rightarrow \Phi_V = \frac{\Delta P}{g H (\rho_g - \rho_l)}, \quad (2.1)$$

where ρ_g and ρ_l are the gas and liquid densities, respectively, H the height of the test section and g the gravitational acceleration. Pressure differences are only measurable for substances with different densities. Considering that $\rho_g \ll \rho_l$, Eq. (2.1) approximates $\Phi_V \approx -\Delta P / (\rho_l g H)$. The accuracy of the Validyne DP45 very low pressure transducer is

± 0.5 percent over the full measurement range. Typical pressure differences are in the range of 10 to 150 Pa, so that the membrane with maximum pressure allowance of 550 Pa was selected. This corresponds to an absolute measurement uncertainty of 5.5 Pa, or approximately 0.55 mm water column height, or an error of 0.056 percent volume fraction for the micro-bubbles (based on Eq. 2.1). Because of the sensitivity of the pressure transducer, the pressure difference is measured at a temporal frequency of 1 kHz over 30 seconds to reduce the pressure fluctuations below the measurement accuracy.

2.6. RESULTS

2.6.1. CALIBRATION CURVE

The normalized intensity gradient of one bubble with diameter of $950 \mu\text{m}$, attached to the calibration sheet, is fitted with a function of the summation of three Gaussian terms. Clearly, the calibration curve is not symmetrical; see Fig. 2.4. The skewness, a measure of the asymmetry of the data around the mean, is positive (+ 1.3403) and indicates that the data to the left of the calibration curve are spread out more than to the right. This observation is in agreement with the findings of Fdida and Blaisot (2009), who referred to the asymmetry as the ‘perspective effect’. An alternative method to describe the function shape is the kurtosis, which measures the tailedness of the calibration curve. The computed kurtosis of 3.61 exceeds the kurtosis of a univariate normal distribution (3.00), meaning that the calibration curve is more peaked than than univariate normal distribution.

2.6.2. LOCAL BUBBLE CONCENTRATIONS IN BUBBLE CLOUDS

The void fraction in the center of the micro-bubble cloud is determined at 400 mm below the free surface. In total, 4 524 micro-bubbles were detected within the control volume over 1 600 consecutive images. In order to further inspect the robustness of the recognition method, detected bubbles are marked and visually inspected. Table 2.1 presents the measured void fraction for 4 time periods to check for compliance with the steady-state condition. The distribution of the bubble diameters is also shown in Fig. 2.5.

Once the (x, y, z) -coordinates of the micro-bubbles are measured accurately, bubbles that are located within the defined measurement section are selected for further analysis. Although the boundaries of the measurement volume are demarcated accurately, only the absolute z -position relative to the focal plane is known. In other words, we do not have information if the bubble is located in front or behind the focal plane. Unless all bubbles are known to be located on one side of the focal plane, no full 3D spatial rep-

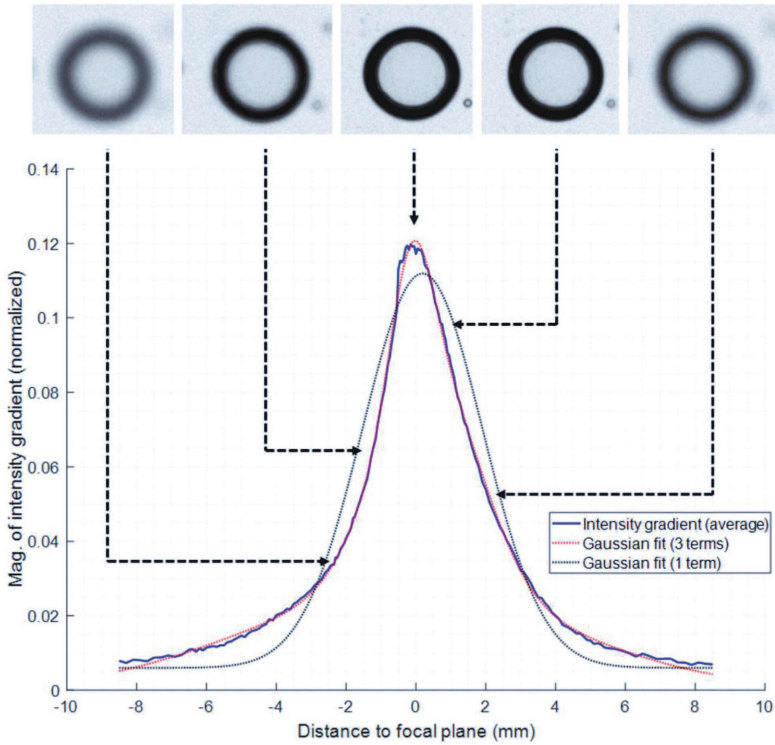


Figure 2.4: Calibration curve of the defocused distance to object focal plane (diagram) with examples of the defocused calibration bubbles (top).

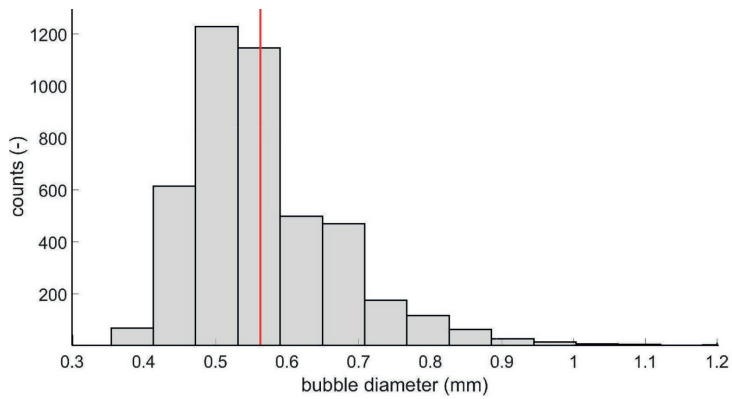


Figure 2.5: Histogram of the bubble diameters based on 4 524 bubbles with average bubble size of $563 \mu\text{m}$ (indicated by the red line).

resentation can be reconstructed with this method. To overcome this problem, Legrand et al. (2016) depicted the z -coordinate of the particle to be able to construct a 3D vi-

Table 2.1: Measured bubble characteristics for 4 consecutive time periods of 800 seconds (i.e. 400 images) each. The bubble concentration, mean and median bubble diameter, and number of detected bubbles are stationary in time.

time period (s)	0 - 800	802 - 1600	1602 - 2400	2402 - 3200	total
bubble concentration (%)	0.079	0.076	0.076	0.079	0.078
mean diameter (mm)	0.563	0.559	0.563	0.566	0.563
median diameter (mm)	0.532	0.532	0.532	0.543	0.532
number of bubbles (-)	1164	1150	1109	1101	4524

sualization. In this work, we do follow this approach, as the visualization gives twice as high bubble concentrations when the negative z -positions are mirrored in the $(x,y,z=0)$ -plane.

2.6.3. COMPARISON OF THE z -POSITION WITH REFERENCE CAMERA

To validate the z -position found by our method, we installed a reference camera, aligned with the center line of the control volume and perpendicular to the optical axis of the main camera. Arrays of bubbles were injected and recorded simultaneously in the measurement section by both cameras. Images from the main camera span the x,y -plane, and thus first need to be processed to obtain the z -coordinate. Meanwhile, images recorded by the reference camera span the (y,z) -plane, and hence the z -coordinate is directly observable. Figure 2.6 shows the comparison with the reference camera and validates that defocused imaging allows for determining the in-depth z -position of microbubbles from the recorded images by only the main camera. The offset for the z -position by the reference camera was set afterwards during the processing as it proved to be very difficult to place the calibration target exactly in the focal plane of the main camera. A simple linear regression analysis is performed to test the quality of the fit for determining bubble positions by defocused shadowgraphy (indicated by the red line). Based on the R-squared of 0.9883, we conclude that the calculated z -positions agree well to the validation data.

2.6.4. COMPARISON WITH DIFFERENTIAL PRESSURE REFERENCE MEASUREMENTS

A second reference method, based on the differential pressure between two interconnected water columns, is performed to validate the correctness of the void fraction measurements. One water column is filled with a single-phase liquid, while the second column (in which the measurement section is located) is aerated with gas bubbles. The

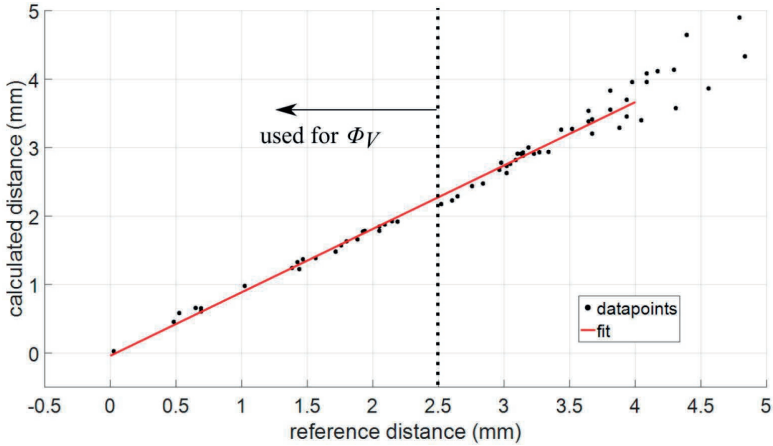


Figure 2.6: Histogram of the bubble distance based on 4,524 bubbles with average bubble size of $563 \mu\text{m}$ (indicated by the red line).

reference void fraction, measured by the pressure difference between the single-phase water column and the aerated column, equals to 0.081 ± 0.011 percent. The differential pressure measurement operates independently from the defocused shadowgraphy in the sense that different approaches are employed. However, one important limitation of the pressure difference method is the global scope, by which it is not possible to obtain local void fractions. Bubbles near the bottom of the water column experience a larger static head pressure and hence are more compressed. Naturally, bubbles close to the free surface are relatively more expanded. Considering a water column of 0.95 meter, the static head compresses micro-bubbles at the bottom by roughly 9 percent in volume and 2.9 percent in diameter, assuming isothermal compression and atmospheric pressure at the free surface. As the measurement section is located near the center of the water column (0.40 meter below the free surface, the camera records bubbles with average bubble diameters and thus volume changes may be ignored. Therefore, complex flow behaviors are not taken into account, but it is possible that bubbles have a preference to center in the middle of the channel, leading to a non-uniform bubble density distribution in the water column. However, visual inspection of the stagnant aerated liquid learned that the bubble cloud (at least visually) were relatively evenly distributed in the water column. Even though the global scope of the differential pressure measurement is not able to provide local information in the control volume, yet the reference void fraction corresponds reasonable well to the obtained bubble concentration of 0.078 percent by the defocused volumetric shadowgraphy method.

2.7. CONCLUSION AND OUTLOOK

Defocused volumetric shadowgraphy is used to determine accurately the micro-bubble position z from 2D-images, recorded by a single camera, and provides detailed volumetric information about the number and volume of non-condensable micro-bubbles in the center of bubble clouds. It is demonstrated that this method is able to accurately determine local void fractions for bubble clouds in (industrial) setups with limited optical access in a non-intrusive and non-disturbing manner. The bubble size distribution is determined by finding the center of the bubble using the Circular Hough Transform (CHT) and the Sobel edge detection (from MATLAB) and the radius by the radial location of the median of 4 maximum intensity gradients. Based on the Eötvös and Bond number, the non-condensable bubbles are considered to be spherical so that the 2D projected bubbles provide accurate representation for the 3D-volume. Currently, most work has been done on the density measurement of droplets in dense sprays. This work extends the literature on the field of defocused imaging and local void fraction measurements by applying this method to detect micro-bubbles in aerated liquids. In future research, the number of local measurements may be extended by positioning the control volume systematically throughout the fluid section to construct full bubble concentration maps for several aerated flow conditions.

BIBLIOGRAPHY

- Blaisot, J. B., & Yon, J. (2005). Droplet size and morphology characterization for dense sprays by image processing: Application to the Diesel spray. *Exp. Fluids*, 39(6), 977–994.
- Blaisot, J.-B., & Ledoux, M. (1998). Simultaneous measurement of diameter and position of spherical particles in a spray by an original imaging method. *Appl. Opt.*, 37(22), 5137–5144.
- Bröder, D., & Sommerfeld, M. (2007). Planar shadow image velocimetry for the analysis of the hydrodynamics in bubbly flows. *Meas. Sci. Technol.*, 18(8), 2513.
- Buraga-Lefebvre, C., Coëtmelec, S., Lebrun, D., & Özkul, C. (2000). Application of wavelet transform to hologram analysis: Three-dimensional location of particles. *Opt. Lasers. Eng.*, 33(6), 409–421.
- Dehaeck, S., Van Parys, H., Hubin, A., & van Beeck, J. P. A. J. (2009). Laser marked shadowgraphy: A novel optical planar technique for the study of microbubbles and droplets. *Exp. Fluids*, 47(2), 333–341.
- Fdida, N., & Blaisot, J.-B. (2009). Drop size distribution measured by imaging: Determination of the measurement volume by the calibration of the point spread function. *Meas. Sci. Technol.*, 21(2), 025501.
- Lebrun, D., Ozkul, C., Touil, C. E., Blaisot, J. B., & Kleitz, A. (1993). On-line particle size and velocity measurements by the analysis of defocused images: extended depth of field. In M. J. Downs (Ed.), *Laser dimensional metrology: Recent advances for industrial application* (pp. 139–148). SPIE.
- Lecuona, A., Sosa, P. A., Rodríguez, P. A., & Zequeira, R. I. (2000). Volumetric characterization of dispersed two-phase flows by digital image analysis. *Meas. Sci. Technol.*, 11(8), 1152.
- Lee, C., Wu, C. H., & Hoopes, J. A. (2009). Simultaneous particle size and concentration measurements using a back-lighted particle imaging system. *Flow Meas. Instrum.*, 20(4), 189–199.
- Legrand, M., Nogueira, J., Lecuona, A., & Hernando, A. (2016). Single camera volumetric shadowgraphy system for simultaneous droplet sizing and depth location, including empirical determination of the effective optical aperture. *Expe. Therm. Fluid Sci.*, 76, 135–145.
- Malot, H., & Blaisot, J.-B. (2000). Droplet size distribution and sphericity measurements of low-density sprays through image analysis. *Part. Part. Syst. Charact.*, 17(4), 146–158.

- Pentland, A. P. (1987). A New Sense for Depth of Field. *IEEE Transactions on Pattern Analysis and Machine Intelligence, PAMI-9*(4), 523–531.
- Pereira, F., & Gharib, M. (2002). Defocusing digital particle image velocimetry and the three-dimensional characterization of two-phase flows. *Meas. Sci. Technol.*, *13*(5), 683.
- Poelma, C. (2004). *Experiments in particle-laden turbulence: Simultaneous particle/fluid measurements in grid-generated turbulence using particle image velocimetry* (Doctoral dissertation). Delft University of Technology.
- Pu, S. L., Allano, D., Patte-Rouland, B., Malek, M., Lebrun, D., & Cen, K. F. (2005). Particle field characterization by digital in-line holography: 3D location and sizing. *Exp. Fluids*, *39*(1), 1–9.
- Ren, K. F., Gouesbet, G., Géhan, G., Lebrun, D., Özkul, C., & Kleitz, A. (1996). On the measurements of particles by imaging methods: Theoretical and experimental aspects. *Part. Part. Syst. Charact.*, *13*(2), 156–164.
- Willert, C. E., & Gharib, M. (1992). Three-dimensional particle imaging with a single camera. *Exp. Fluids*, *12*(6), 353–358.

3

NON-INTRUSIVE IMAGING METHOD FOR SHOCK WAVE PROPAGATION IN BUBBLY LIQUIDS

A novel experimental imaging-based method is presented for the non-intrusive determination of shock wave characteristics (i.e. shock wave speed and magnitude, and shock-induced liquid velocity) in a bubbly flow solely from gas bubble velocities. Shock wave speeds are estimated by the relative motion between gas bubbles at two locations by splitting the camera field-of-view using a mirror construction, increasing the dynamic spatial range (DSR) of the measurement system. Although gas bubbles have in general poor tracing properties of the local fluid velocity, capturing the relative dynamics provides accurate estimates for the shock wave properties. This proposed imaging-based method does not require pressure transducers, the addition of tracer particles, or volumetric reconstruction of the gas bubbles. The shock wave magnitude and shock-induced liquid velocity are computed with a hydrodynamic model, which only requires non-intrusively measured variables as input. Two reference measurements, based on pressure transducers and the liquid velocity field by particle image velocimetry (PIV), show that the proposed method provides reliable estimates for the shock wave front speed and the shock-induced liquid velocity within the experimental range of $70 < U_s < 400$ m/s.

This chapter is based on: W.A. Cornel, J. Westerweel, C. Poelma, "Non-intrusive imaging method for shock wave propagation in bubbly liquids", *Experiments in Fluids*, volume 64, issue 2, 2023

3.1. INTRODUCTION

Shock waves may cause severe damage to hydraulic systems by transient pressure variations (Ghidaoui et al., 2005; Schmitt et al., 2006). The dynamics of propagating shock waves through single-phase liquids and multiphase liquids in confined geometries have been studied extensively over recent decades (Jakeman et al., 1984; Kameda et al., 1998; Noordzij & Van Wijngaarden, 1974; Tijsseling, 2007). Imaging-based methods have been employed to study shock wave characteristics of propagating shock waves through two-phase gas-liquid mixtures (Ando et al., 2011; Frolov et al., 2022) and laser-induced shock waves (Vogel et al., 1996).

In case of laser-induced shock waves, they are emitted spherically, by approximation, when a sufficiently high-intensity focused laser beam evaporates liquid locally. In these highly-controlled measurements, shock wave front locations and shock wave speeds are measured by high-speed camera (Hayasaka et al., 2016; Horvat et al., 2022; Lee et al., 2011; Mur et al., 2022). Emitted shock wave pressures can be estimated reliably by the shock wave speed near the emission center (Vogel et al., 1996), which allows to estimate shock wave pressures solely from camera images.

For shock waves propagating through two-phase gas-liquid mixtures, Campbell et al. (1958) were among the first to use *optical* devices to determine shock wave propagation speeds. They applied two photoelectric cells at different heights and measured the passage of the shock wave by the change in light transmission through the mixture. However, this method is only applicable to relative large void fractions while the bubble dynamics cannot be studied due to the limited spatial resolution. Ando et al. (2011) used high-speed camera images to validate the theoretically predicted wave speed by superimposing the expected pressure wave front on the images. Frolov et al. (2017) investigated the momentum transfer from the shock wave to a bubbly air-water mixture by tracking the motion of bubbles and a polyethylene thread to quantify the bubble and liquid velocities, respectively, while obtaining the shock wave speed from pressure transducers. Recently, Gluzman and Thomas (2022) studied unsteady shock wave propagation in aviation fuel cavitation by high-speed imaging and developed an image processing technique, denoted enhanced gradient shadowgraphy, to enhance the appearance of shock waves in the images. Frolov et al. (2022) used high-speed imaging to study the shock wave front with non-reacting and reacting gas bubbles for the application in pulsed detonation hydro ramjet, and extracted the shock-induced bubble velocity from the images. Shock wave pressures are commonly measured by high-frequency pressure

transducers. However, disadvantages of pressure transducers include the limitation to measure only at the walls (not inside the flow domain of interest), they are intrusive, and, in case of high temperatures or restricted areas pressure transducers cannot be used at all.

In this research we propose an imaging-based method that non-intrusively estimates shock wave pressure and velocity, and shock-induced liquid velocity, for shock waves propagating through an aerated liquid, solely from the observed change in bubble velocity and without the need for pressure transducers or tracer particles. Only a single camera (100 kHz) is required. Although cameras are commonly used to image the response of bubbles (see above), to the best of the authors' knowledge no method has been developed yet that determines shock wave pressures directly from the observed change in bubble velocity during the shock wave passages. Shock waves are generated by dropping a free-falling weight on a cylinder, submerged in an elastic tube, whereby the momentum is transferred to the gas-liquid mixture. The shock wave front speed U_s is determined from the *relative* motion of the bubbles between two separated locations. The relative motion of the gas bubbles is used to indicate the arrival of the shock wave front. Since shock waves induce large transient velocity gradients in the bubbly liquid, bubbles may not be considered ideal candidates at first. Indeed, bubbles with sizes in the range of several millimeters have poor fidelity as flow tracers (Mei, 1996). However, their response to sudden changes in ambient pressure is highly consistent. We focus on the *relative* motions between similar bubbles during the initial interaction between the proximal bubble side and the shock wave front. In a second step, a hydrodynamic model is used to estimate the shock wave pressure change ΔP and shock-induced liquid velocity Δu_l from U_s (from step 1) and the evolution in slip velocity u_{slip} . Additional two-phase PIV and high-frequency pressure measurements are performed in a controlled experiment of a propagating shock wave through a bubbly air-water mixture in a vertical pipe to validate the proposed method.

The structure of this paper is as follows: The next section describes the hydrodynamic model. The experimental setup and data processing of the bubble motions, the determination of the shock wave speed by a split field-of-view (FOV), the reference two-phase PIV images, and pressure sensor data are described in Section 3.3. Results for the measured shock wavefront speeds, and the shock-induced pressures and liquid velocities, are shown and compared with the reference measurements. The final section summarizes our main findings and conclusions.

3.2. MODEL DESCRIPTION

RELEVANT EQUATIONS

The steady shock wave speed U_s in a bubbly liquid with initial density ρ_0 in a deformable tube with initial cross-section A_0 can be derived from the quasi one-dimensional mixture conservation equations with fluid-structure interaction and is given by (Ando et al., 2011):

$$U_s = \sqrt{\frac{g(P_{l,1}) - g(P_{l,0})}{\rho_0 A_0 \left(1 - \frac{\rho_0 A_0}{\rho_1 A_1}\right)}}, \quad (3.1)$$

with:

$$g(P_l) = A_0 \left[\left(1 - \frac{2P_{l,0}a_0}{Eh}\right) P_l + \left(\frac{a_0}{Eh}\right) P_l^2 \right], \quad (3.2)$$

where subscript 0 represents the undisturbed state prior to the shock wave, and subscript 1 the state for elevated pressures, E the Young's modulus, h the wall thickness, and a_0 the mean radius as defined by $(a_{outer} + a_{inner})/2$. For a rigid tube ($E \rightarrow \infty$), this reduces to $U_s = \sqrt{(P_{l,1} - P_{l,0})/(\rho_0(1 - \rho_0/\rho_1))}$, while finite values of E yield lower shock wave velocities. The shock-induced liquid velocity $\Delta u_l = u_1 - u_0$ on the aft side of the shock is given by (Ando et al., 2011):

$$\Delta u_l = \left(1 - \frac{\rho_0 A_0}{\rho_1 A_1}\right) U_s. \quad (3.3)$$

Although Eq. (3.1) provides a direct relation between the steady shock wave speed U_s and the shock wave pressure amplitude $\Delta P_s = P_{l,1} - P_{l,0}$, we do not have information on the mixture density ρ_1 and mid-plane cross-section A_1 after the shock, and thus we cannot directly apply this equation to determine the shock wave speed. For very dilute bubble mixtures, the change in dispersed gas phase volume might possibly be determined by resolving the variation in the diameter of individual bubbles. However, here we assume that volumetric information is not available. Combining Eqs. (3.1-3.3) yields :

$$U_s = \frac{1}{\rho_0 \Delta u_l} \left[\left(1 - \frac{2P_{l,0}a_0}{Eh}\right) (P_{l,1} - P_{l,0}) + \left(\frac{a_0}{Eh}\right) (P_{l,1}^2 - P_{l,0}^2) \right] \quad (3.4)$$

The last term on the r.h.s. of Eq. (3.4) can be neglected for small to moderate elevated pressures, as: $a_0/(Eh) \approx O(10^{-9} Pa^{-1})$, so that the last term $O(1 \text{ m/s}) \ll O(U_s)$, which yields :

$$\Delta P_s = \frac{\rho_0 U_s \Delta u_l}{\left(1 - \frac{2P_{l,0}a_0}{Eh}\right)}, \quad (3.5)$$

Typical values for the fraction in the denominator of Eq. (3.5) are $O(10^3)/O(10^7) \ll 1$, which yields the original Joukowsky or water hammer equation:

$$\Delta P_s = \rho_0 U_s \Delta u_l \quad (3.6)$$

The acoustic wave speed c is commonly used as independent parameter in the Joukowsky equation instead of the shock wave speed U_s . For finite-amplitude shock waves, this only holds for single-phase fluids or very dilute bubbly gas-liquid mixtures where $U_s \approx c$, i.e. for unity Mach number, but this is invalid for higher void fractions where $U_s > c$. The shock wave speed U_s is determined accurately from the split-FOV imaging method, and the liquid density can be estimated by $\rho_0 = \alpha \rho_g + (1 - \alpha) \rho_l \approx \rho_l$ for low aeration levels α , where ρ_g is the gas density and ρ_l the liquid density. However, Δu_l cannot be measured optically as we purposely avoid the use of seeding particles. Hence, Δu_l is determined by the bubble slip velocity (u_{slip}) between the liquid and bubble velocity, $u_{slip} = u_l - u_b$, and coupled to ΔP_s via Eq. (3.6). The equation of motion for isolated deformable non-spherical bubbles is given by (Salibindla et al., 2021):

$$V_b \rho_b \frac{d\mathbf{u}_b}{dt} = \rho_l V_b C_A \left(\frac{D\mathbf{u}_l}{Dt} - \frac{d\mathbf{u}_b}{dt} \right) + \frac{\rho_l}{2} A_b C_D (\mathbf{u}_l - \mathbf{u}_b) |\mathbf{u}_l - \mathbf{u}_b| - V_b \nabla P + \mathbf{F}_h + \rho_l C_L (\mathbf{u}_l - \mathbf{u}_b) \times (\nabla \times \mathbf{u}_l) + V_b (\rho_l - \rho_b) \mathbf{g}, \quad (3.7)$$

where the six terms on the right-hand side represent added-mass, drag, pressure gradient, history, lift and buoyancy forces, respectively. The added mass coefficient is C_A , and ∇P is the pressure gradient around the bubble (Salibindla et al., 2021).

MODEL FRAMEWORK

In the present study, we apply a model to determine the properties of a shock wave propagating through a quiescent aerated liquid, confined in a vertical elastic tube. The following assumptions are made: (1) the flow is one-dimensional, (2) the Basset history force \mathbf{F}_h is ignored in the model, as the effect of the Basset force is negligible for bubble Reynolds numbers $Re_b = |\mathbf{u}_l - \mathbf{u}_b| D_b / \nu_b > 50$ (Magnaudet & Eames, 2000; Salibindla et al., 2021; Takagi & Matsumoto, 1996), (3) the gas density is neglected since $\rho_b \ll \rho_l$, (4) the lift force term (based on $\nabla \times \mathbf{u}_l = 0$) is neglected, and (5) the thermodynamic behavior is adiabatic, since $\chi / (\omega R^2) \approx O(10^{-4}) \ll 1 \ll I_g / R \approx O(10^2)$ for bubbles with a typical diameter of 5 mm (Van Wijngaarden, 2007). Following Kalra and Zvirin (1981), velocities and gravitational acceleration are taken positive in downward direction. The term on the l.h.s. in Eq. (3.7) is neglected based on assumption (3). For $\partial \mathbf{u}_l / \partial t = U_s \partial \mathbf{u}_l / \partial y$ (since $\partial y = U_s \partial t$) and $\mathbf{u} = \mathbf{u}_l$, the material derivative $D\mathbf{u}_l / Dt = \partial \mathbf{u}_l / \partial t + \mathbf{u} \cdot \partial \mathbf{u}_l / \partial y$ can be writ-

ten as $Du_l/Dt = (U_s + u_l)\partial u_l/\partial y$. Since $U_s \gg u_l$, the term $u_l \cdot \partial u_l/\partial y$ can be neglected, and the material derivative reduces to $Du_l/Dt \approx du_l/dt$, resulting in $du_l/dt - du_b/dt = du_{slip}/dt$. For the response of a bubble to a shock wave, Eq. (3.7) thus simplifies to:

$$\frac{du_{slip}}{dt} = \frac{1}{C_A} \left(\frac{1}{\rho_l} \frac{dP}{dy} - \frac{3C_D}{4D_b} u_{slip} |u_{slip}| + g \right), \quad (3.8)$$

where the change of the bubble slip velocity depends on the shock wave pressure, the drag force and, the buoyancy force. The pressure gradient term is estimated by: $dP/dy = (1/U_s)dP/dt \approx -(1/U_s)\Delta P_s/\Delta t = (1/U_s)(P_{l,0} - P_{l,1})/t^*$, where $\Delta P_s = P_{l,1} - P_{l,0} = \rho_0 U_s \Delta u_l$ (Eq. 3.6), and t^* from the elapsed time between the arrival of the shock wave t_0 and the moment of maximum absolute bubble velocity (see Fig. 3.4). We assume that the shock wave profile has a constant slope of $dP/dt = (P_{l,1} - P_{l,0})/t^*$. The shock wave pressure ΔP_s is derived from Eq. (3.6). An *a priori* estimate of Δu_l in the range from 0 to u_b m/s (because $|\Delta u_l| < |u_b|$) in steps of 0.01 m/s is used to compute ΔP_s , while we solve Eq. 3.8 numerically by a forward Euler method for $t = 0$ to t^* in time steps (Δt) of 10^{-8} seconds, since the transient event is of the order of milliseconds. For each Δu_l , the maximum bubble velocity $u_{b,model} = \Delta u_l - u_{slip}$ is compared to the measured u_b and the estimated Δu_l that minimized $|u_{b,model} - u_{slip}|$. This Δu_l is selected and used to compute ΔP_s . Furthermore, the added mass coefficient is taken as $C_A \approx 1/2$ (Batchelor, 2000). The bubble diameter D_b is updated for each time step Δt for changes in the ambient pressure by the shock wave passage via the polytropic gas relation $P_g D_b^{3\kappa} = P_{g,0} D_{b,0}^{3\kappa}$ with $P_g = P_{g,0} + (dP/dt)t$:

$$D_b = D_{b,0} \left(1 + \frac{1}{P_{g,0}} \frac{dP}{dt} t \right)^{-1/(3\kappa)} \quad (3.9)$$

with the initial average bubble equivalent diameter $D_{b,0}$ following directly from Eq. (3.8) for $du_{slip}/dt = 0$ and $dP/dy = 0$, and assuming $\rho_l \gg \rho_b$ (assumption 3):

$$D_{b,0} = \frac{3C_D u_{b,0}^2}{4g} \quad (3.10)$$

where the initial bubble velocity $u_{b,0}$ is determined from the images prior to the shock wave passage. The drag coefficient C_D is modelled as (Turton & Levenspiel, 1986) :

$$C_D = \frac{24}{Re_b} (1 + 0.173 Re_b)^{0.657} + \frac{0.413}{1 + 16300 Re_b^{-1.09}}, \quad (3.11)$$

After the shock wave passage, C_D is set to 2.6 (Kalra & Zvirin, 1981).

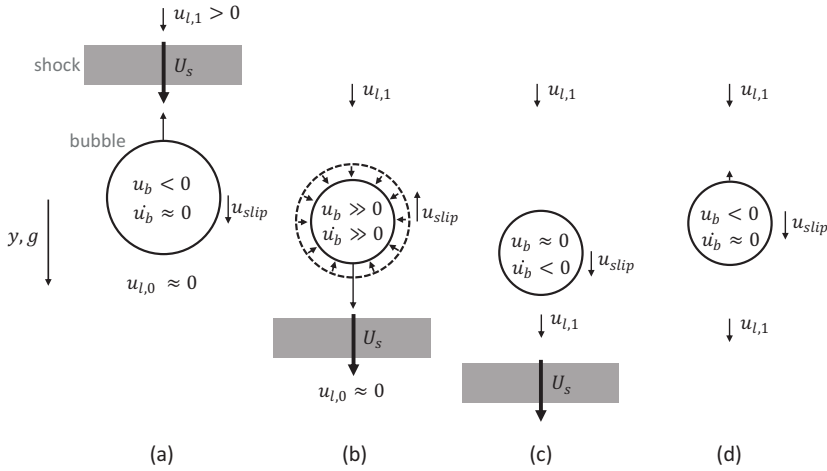


Figure 3.1: Schematic overview of the shock wave passage. An example of experimentally measured liquid and bubble velocities during the shock wave passage is shown in Fig. 3.11 (left), and the bubble response to the shock wave in Fig. 3.12 (inset).

In summary, the framework of the model is as follows:

1. estimate $D_{b,0}$ from the bubble rising velocity before the impact;
2. an *a priori* estimate by looping over Δu_l from 0 to u_b in steps of 0.01 m/s;
3. calculate ΔP_s from Δu_l , aerated liquid density and the measured shock wave speed U_s (from section 3.3.3);
4. numerically solve the non-linear differential equation (eq. 3.8) from $t=0$ to t^* with time step $\Delta t = 10^{-8}$ seconds by a forward Euler numerical scheme and update D_b for each time step;
5. calculate the bubble velocity $u_{b,model}$ by subtracting u_b (the outcome of the numerically solved non-linear differential equation) from the induced liquid velocity Δu_l ;
6. determine Δu_l and ΔP_s by $\min |u_b - u_{b,model}|$

3.3. EXPERIMENTAL SET-UP

3.3.1. FACILITY

Experiments were performed to validate the proposed measurement method and model. Figure 3.2 shows the experimental set-up, which consists of a vertical transparent acrylic

plastic tube (Perspex, $E = 2855$ MPa) with inner diameter D_{in} of 60 mm and 5.0 mm wall thickness. Shock waves are generated by the impact of a free-falling weight ($m = 3.65$ kg), released by an electromagnet, on a submerged piston ($m = 0.246$ kg), whereby the momentum of the free-falling weight (the impactor in Fig. 3.2) is transferred to the piston and subsequently to the liquid. Tests are performed with impact velocities of 0.85 and 1.70 m/s, so that the maximum theoretical shock pressures are within the measurement range of the pressure transducers. Specifically, $\Delta P_s = \rho_l u_{imp} U_s \approx 680$ kPa $<$ 689 kPa, based on the shock wave speed of 400 m/s in the confined tube. With complete immersion of the piston, effects of entrapped gas between the impactor and the liquid surface are largely avoided. No significant friction occurs between the piston and the inner wall as the $D_{piston} = 59$ mm $<$ D_{in} , which also allows the gas from the aeration to escape freely around the piston. Bubbles are generated by forcing pressurized air through a porous block (Pentair) at the bottom of the tube. To ensure similar-sized bubbles, only bubbles that emerge near the core of the porous block are let into the vertical tube. The liquid phase consists of filtered tap water and the gas phase is ambient air. A single high-

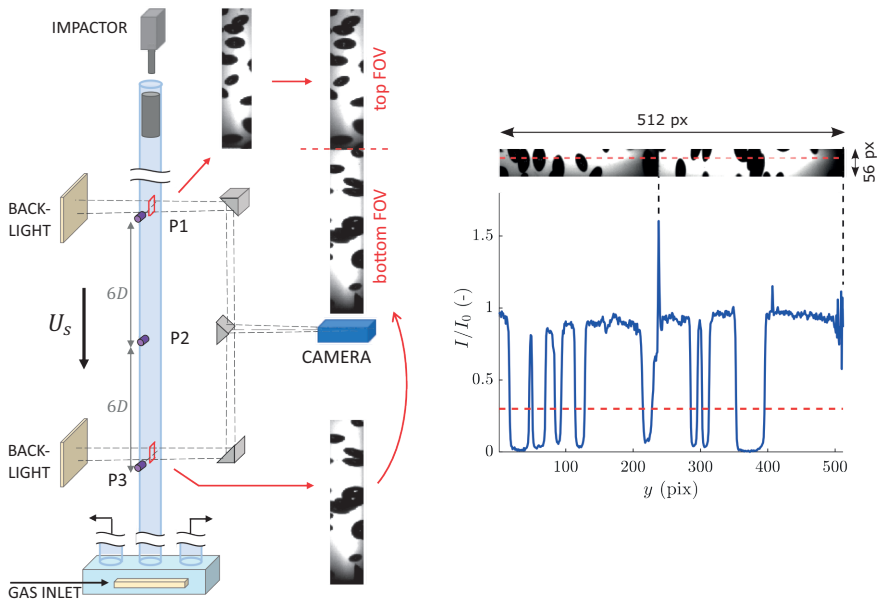


Figure 3.2: Left: experimental setup with optically split FOV configuration. The optical configuration includes one camera, one prism and two mirrors to measure the shock wave properties. Pressure transducers (P1 to P3) are solely used to validate the image-based measurements. Right: intensity threshold (horizontal dotted line) to segregate the bubbles from the liquid.

speed CMOS camera (Phantom VEO 640L), equipped with a Nikon 200 mm lens ($f^\# = 11$), is aligned with the optical construct of one prism and two mirrors (Thorlabs) to capture

bubbles in high spatial and temporal resolution ($99 \mu\text{m}/\text{pix}$, $\Delta t = 10 \mu\text{s}$) for determining the shock wave speed in the top and bottom field-of-view (FOV). The centers of the top and bottom FOVs are separated by 720 mm. The recorded images have a 512×56 -px format, which is the maximum image size (in pixels) at the frame rate of 100 kfps. The upper part of the image (256×56 px) displays the top FOV, and the lower part (256×56 px) the bottom FOV (see Fig. 3.2). Fluctuations in light intensity are negligible during the transient event (≈ 1 ms).

Three high-speed pressure transducers (PCI Piezoelectric PCB102) with resonance frequency ≥ 500 kHz are flush-mounted in the Perspex tube wall with an equal spacing of $6 D_{tube}$. High-frequency pressure transducers are commonly used to determine the shock wave speed in tubes and serve here as reference measurements. Pressure transducers P1 and P3 correspond to the top and bottom FOV respectively, and P2 to the optical axis of the camera. The signals are sampled by National Instruments (NI) LabVIEW 2018 (version 18.0.1f4) and NI Data Acquisition (DAQ) USB-6212 with a sampling rate of 100 kHz, resulting in a Nyquist frequency of 50 kHz. Once the electromagnet releases the impactor, a TTL signal triggers both the acquisition of the pressure (LabVIEW 2018) and images (DAVIS 8.4) simultaneously.

The aeration level is measured by a differential pressure transducer (Validyne model DP45), which compares the hydrostatic pressure of the aerated column with a reference water-only column of the same height. The sampling frequency of the differential pressure transducer is 100 Hz and is only employed before and after the impacts, as the membrane cannot withstand the larger shock wave amplitudes upon impact. The aeration level is calculated by $\alpha = \Delta P_m / gL(\rho_l - \rho_g)$, where ΔP_m is the pressure difference over the membrane. The sensor is calibrated in-situ using different water heights.

3.3.2. BUBBLE VELOCITY BY IMAGING

Shadowgraphy is used to capture the motion of bubble images. Planar tracking of individual bubbles is compromised by the possibility of overlapping bubble images in the recorded image. Segregation of overlapping bubbles has been addressed extensively in literature (Kim et al., 2016; Lau et al., 2013; Li et al., 2020). However, for cropped image sizes (to enable high-speed recording) it is often not possible to capture entire bubbles (or only at very low spatial resolutions) which makes volumetric reconstruction of individual bubbles even more problematic. Instead, the displacement of the proximal bubble side is tracked by a 1D-correlation, parallel to the direction of the shock wave, and

volumes are not reconstructed. Fig. 3.3 summarizes the image processing steps. First, the raw images are corrected for the background image (without bubbles, Fig. 3.3b). Second, the bubbles are extracted by applying an intensity threshold, where $I_{binary}(i, j) = 1$ for $I(i, j) \leq I_{th}$ and zero otherwise. The threshold level is set to 30 % of the average background intensity scale (Fig. 3.3 left) for all images. In the binary images, the objects are morphologically filled using the MATLAB (version R2018b) function *imfill*. Proximal bubble edges are detected by evaluating a 3×3 px array around each possible line correlation center. For each image with size (N_y, N_x) there are $(N_y - 2)(N_x - 2)$ possible line correlation centers that are evaluated. Proximal bubble edges are detected at pixel $(i + 1, j)$ when the condition $I(i + 1, j) - I(i, j) = 1$ is satisfied, together with constraints to prevent (1) that vertical line correlations are applied over the bubbles' edges that are parallel to the incoming shock wave, and (2) that no other bubbles are present in the proximity that interfere with the 1D-correlation, to ensure that only valid line correlations are being processed. In the second step, a Gaussian 2D filter is applied to the background-corrected image (Fig. 3.3, a) to remove high frequency spatial noise, and the intensity gradient operator in vertical direction is calculated to emphasize the edges of the bubbles' images using the MATLAB function *imgradientxy*. 1D-correlations are used to calculate the displacement of the proximal bubble edge between images, where these correlations have a window size of 21×1 px and are centered at pixels that are indicated as proximal bubble edges (from step 1). Interpolation using a three-point Gaussian fit is applied to determine the displacement at sub-pixel level (Adrian & Westerweel, 2011).

3.3.3. SHOCK WAVE FRONT SPEED BY IMAGING

Once a shock wave front arrives at the proximal side of a bubble, the bubble surface deforms by the change in external pressure and it accelerates in the direction of the shock wave. Note that the differences in scales between travelled distance of the shock wave front (U_s / f_{cam}), and bubble diameter (D_b) cause a trade-off between high temporal resolutions (but cropped images) or high spatial resolutions (but low frame rates). To circumvent this, we split the field-of-view (FOV) of a single camera into two FOVs, separated by distance ΔY . Each FOV focuses on a local flow region with vertical length $L_{y,im} = 256$ px $\ll \Delta Y$, so that bubble motions on two separated positions can be studied simultaneously. This results in an increased dynamic spatial range (DSR) = $(2L_{y,im} + \Delta Y) / \Delta y_{b,max}$, where $\Delta y_{b,max}$ is the bubble's maximum displacement (Adrian & Westerweel, 2011; Westerweel et al., 2013), with a similar dynamic velocity range (DVR) as if the FOVs were not split, i.e. $\Delta Y = 0$. Therefore, by splitting the FOV by distance ΔY , we increased the capability of the measurement system by $DVR \times DSR = (2L_{y,im} + \Delta Y) / \sigma_u$, where σ_u rep-

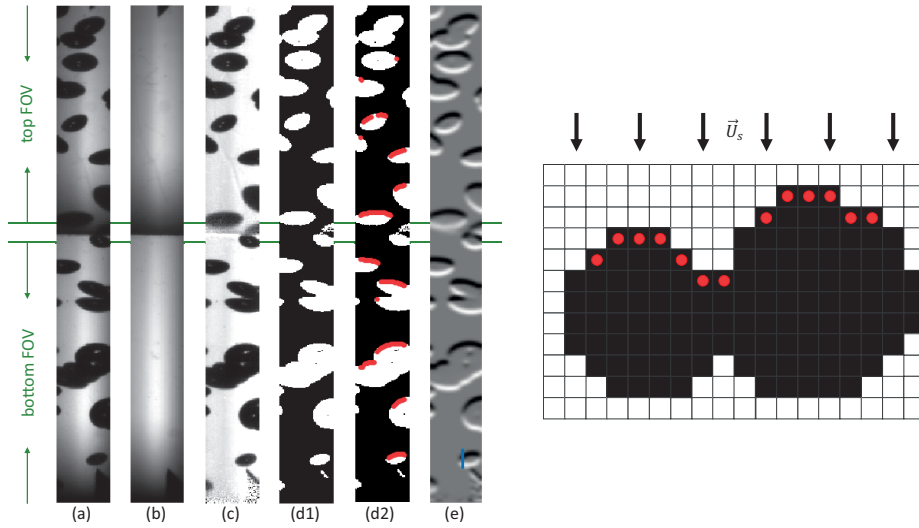


Figure 3.3: Post-processing for the split-FOV images for determining the bubble velocity by 1D-line correlations (left); and an example of 1D-correlation centers for determining the bubble displacement (right). The red dots indicate pixels that are used as center for determining the vertical displacement by line correlations (see also *d2*). Note that bubble ‘sides’ are not taken into account due to the sharp local curvature. The shock wave arrives from the top.

resents the rms error in the velocity measurement. Splitting one image into two FOVs is done by an optical alignment of a prism and two mirrors. For finite-amplitude pressure waves, the arrival time of the shock wave is uniquely defined by the time instance at which the bubble velocity intersects the zero velocity threshold (see Fig. 3.4). The shock wave speed U_s is determined using the time difference Δt between the moment when the shock wave affects bubbles in each of the two FOVs and it is defined by $U_s = \Delta Y / \Delta t$. Increasing ΔY has no effect on the spatial resolution of the images, as the spatial resolution only depends on the size of the FOV. The largest measurement uncertainty is introduced by the arrival time of the shock wavefront. With the simultaneous recording of the two FOVs on the same image sensor, the time difference in the passing of the shock wave is uniquely registered. The magnitude of the displacement is less relevant, as long as the bubble deformation can be measured. Incidentally, for the most severe impacts, precursory waves through the frame (to which the mirrors are attached to) may cause oscillations in the velocity profile. These oscillations have negligible effect on the shock wave speed determination as the velocity fluctuations of the precursory waves are much smaller than the change in velocity by the passage of the shock wave.

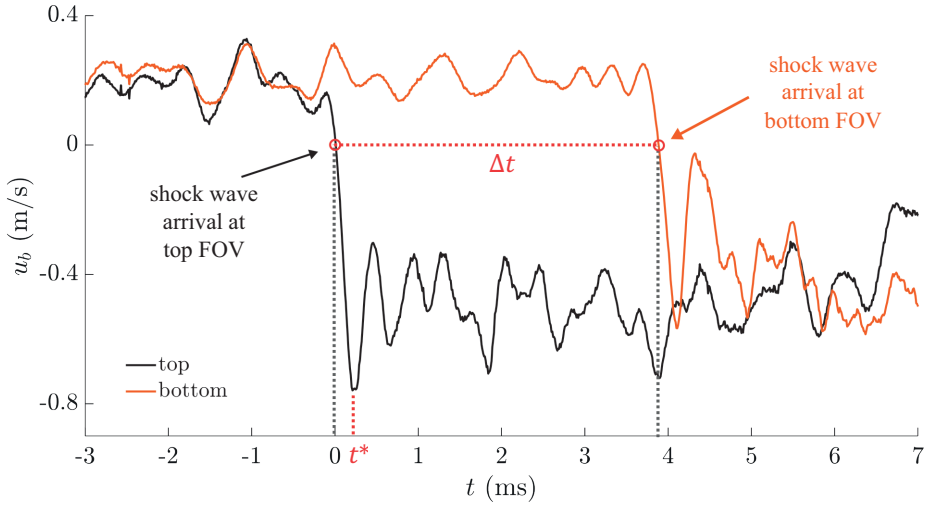


Figure 3.4: Example of the shock wave speed determination by images with the split FOVs. The mean velocity of the bubbles in the top FOV (black curve) and bottom FOV (orange curve) changes abruptly during the passage of the shock wave front. As expected, initially the shock wave front is detected by the bubbles located in the top FOV, and 3.88 ms later by the bubbles in the bottom FOV separated 0.72 m from the top FOV. Because the two images are recorded by one camera, there are no synchronization issues, i.e. ‘perfect synchronization’ is achieved. The shock wave speed U_s is directly calculated from the time difference. In this example the shock wave speed is 186 m/s ($= 0.72 \text{ m} / 3.88 \text{ ms}$).

3.3.4. REFERENCE MEASUREMENTS BY TWO-PHASE PIV

Two-phase particle image velocimetry (PIV) measurements in the gas-liquid flow were performed to measure simultaneously the liquid and gas phase velocities during the shock wave passage. Fluorescent tracer particles (FluoStar, 1.1 g/cm^3 , $13 \text{ }\mu\text{m}$ diameter, $\lambda=579 \text{ nm}$) closely follow the liquid motion (with a Stokes number $St \ll 1$). A Nd:YLF laser (Litron LDY300 PIV, 4 mJ/pulse , $\lambda = 527 \text{ nm}$) produces a laser sheet with thickness of 5 mm at a synchronized frequency of 10 kHz that passes through the center of the cylinder and aligned normal to the camera optical axis; see Fig. 3.5. To avoid overexposure by reflections, the camera lens is equipped with an optical high-pass filter (Schott OG590 with a 590 nm cut-off wavelength). This filter passes the emitted orange light by the fluorescent tracer particles and blocks the green light emitted by the laser. An LED array opposite the camera is used for shadowgraphy to record the bubbles as dark objects. Two distinct intensity levels are applied, which allows the segmentation of the bubble and liquid velocity following the method of Lindken & Merzkirch: the high-intensity spots correspond the fluorescent tracer particles and the darker regions represent the bubble images (Kim et al., 2016; Lindken & Merzkirch, 2002). All images (with image size of $896 \times 528 \text{ px}$) are divided into 3,256 interrogation windows of $24 \times 24 \text{ px}$ with a

50% overlap. Interrogation windows that contain at least one pixel with a lower intensity than the threshold (800 counts, see Fig. 3.5, right) are labeled as ‘bubble’, and otherwise labeled as ‘fluid’ (see Fig. 3.6, b). The average liquid velocity is taken as the mean displacement of the ‘fluid’ interrogations windows. The spatial and temporal resolutions are $71.6 \mu\text{m}/\text{px}$ and $100 \mu\text{s}$ respectively. Second, the bright intensity spots of the tracer particle images are removed by setting these pixels to the average background level and then applying a 2D Gaussian smoothing filter using the MATLAB function *imgaussfilt* to reduce any intensity jumps that may occur. The filtered image is now comparable to the image with split FOV and the same algorithm from section 3.3.2 is applied for further processing, where the bubble velocity is determined by 1D-correlations. However, larger objects with more than 1,000 connected pixels, such as the markers and larger bubbles with equivalent radius of 2.8 mm (36 pixels), are removed.

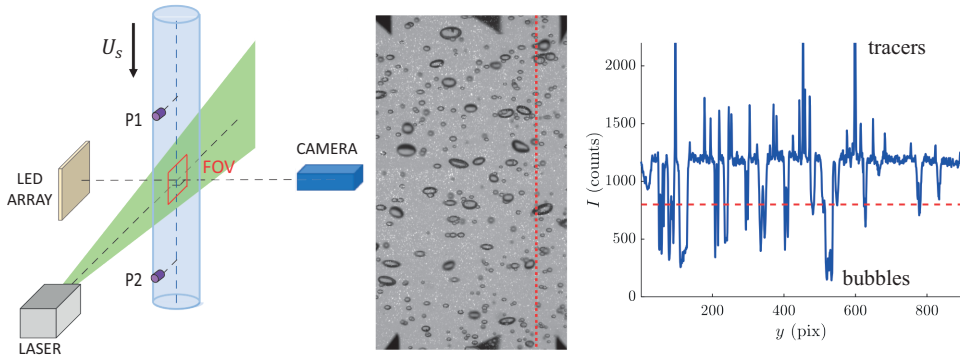


Figure 3.5: Experimental setup with the alignment of the laser sheet for two-phase particle image velocimetry (*left*), typical two-phase PIV image (*center*) where the intensity profile over the dotted vertical line is shown in the right diagram. Intensity drops (below the 800 counts) represent bubbles.

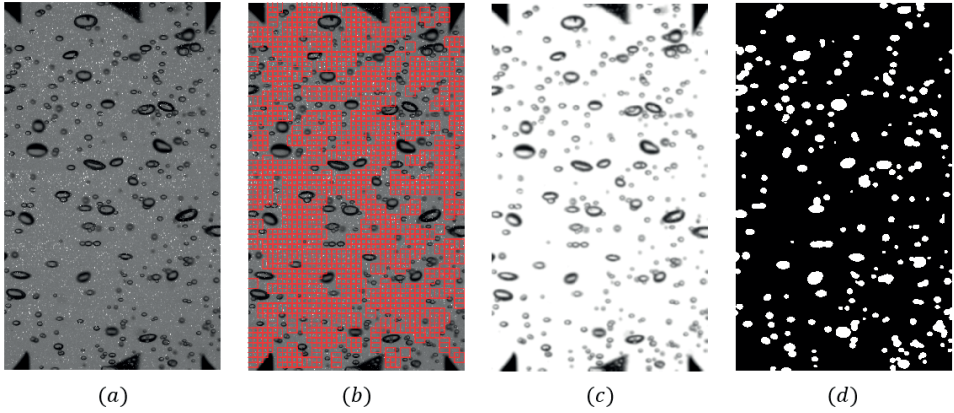


Figure 3.6: Processing of the two-phase PIV images: (a) raw image, the smaller bright intensity spots are the seeding particle images and the darker regions the bubble shadows; (b) PIV interrogation windows (24×24 pixels, 50 percent overlap) that only contain liquid and seeding particles; (c) selection of bubble images after applying the threshold; (d) detected bubbles in the gas phase by applying threshold and filling operators to step (c) by isolating the gas phase, the image can be processed starting at step (d1) of figure (3.3).

3.3.5. REFERENCE MEASUREMENTS BY PRESSURE TRANSDUCERS

Three flush-mounted high-frequency pressure transducers (P1, P2 and P3) serve as reference measurements to validate the imaging-based measurements and are separated by a distance $\Delta Y = 0.72$ m (see Fig. 3.2). Since the PCB model 102B18 pressure transducers have a rise time $\leq 1 \mu\text{s}$, resonance frequency > 500 kHz, and a useful range of 689 kPa (100 psi), the shock pressures can be fully resolved. Fig. 3.7 shows a typical example of a recorded pressure profile during the shock wave passage. The oscillations in the pressure profiles are caused by the presence of gas bubbles (Fig. 3.7, right), while absent in case for (nearly) zero aeration (Fig. 3.7, left), which agrees with the findings by Ando et al. (2011). Precursory waves through the tube material are visible prior to the shock passage. The dotted black line indicates the constant threshold value (in kPa) that is used to determine the time of arrival of the shock wave front. Linear interpolation is applied to enhance the temporal resolution. As expected, the passage of the shock wave front is first detected by the top pressure transducer (P1) that causes a sudden increase in pressure magnitude (at $t = 0$). Consecutively, the shock wave front is detected by the center (P2) and bottom (P3) pressure transducer. The reference shock wave speed $U_{s,ref}$ is computed by $\Delta Y / \Delta t = \Delta Y / (t_{top} - t_{bottom})$, where the subscripts ‘top’ and ‘bottom’ indicate the arrival time at the top (P1) and bottom (P3) pressure transducers, respectively. Pressure transducer P2 is located in between the top and bottom transducer and provides further validation of the measurement.

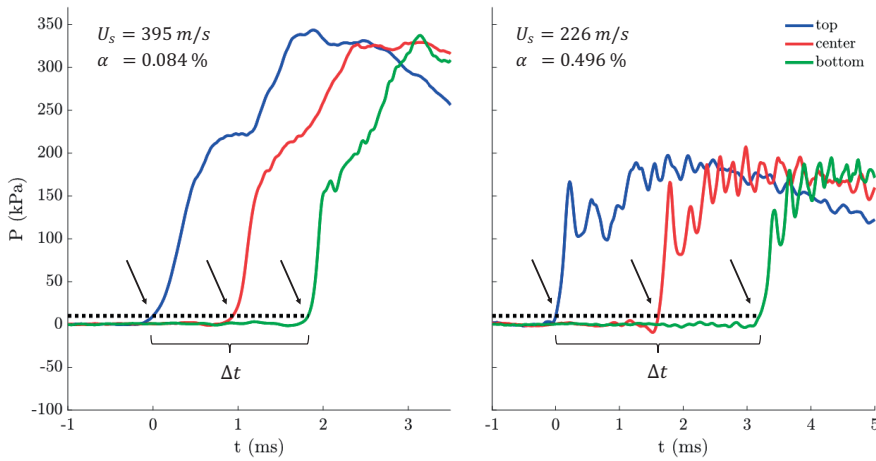


Figure 3.7: Typical pressure profiles by the three pressure transducers; see Fig. 3.2. The black arrows indicate the arrival times of the shock wave front. Pressure profiles of a single impact with impact velocity of 1.70 m/s; (left) 0.084 percent aeration and $U_s = 395.3$ m/s, and (right) 0.496 % aeration and $U_s = 225.6$ m/s. The shock wave speed U_s is determined by the top and bottom pressure transducers, while the center transducer serves as an additional validation check.

3.4. RESULTS

SHOCK WAVE SPEED

Figure 3.8 shows the experimental results for the shock wave front speeds by the non-intrusive optical method U_s and the pressure transducers $U_{s,ref}$. In total, 350 impact measurements were performed, grouped into two sets of 170 and 180 measurements with 0.85 and 1.70 m/s impact velocity, respectively. These sets cover 17 and 18 unique void fraction levels (see Table 3.1), with ten tests per aeration level.

Table 3.1: Experimental conditions

u_{imp} (m/s)	$\bar{\alpha}$ (%)
0.85	0.01, 0.10, 0.14, 0.22, 0.33, 0.39, 0.51, 0.60,
	0.83, 1.01, 1.25, 1.62, 1.98, 2.32, 2.83, 3.13, 3.51
1.70	0.04, 0.08, 0.17, 0.22, 0.28, 0.39, 0.50, 0.57, 0.78
	0.96, 1.07, 1.36, 1.63, 1.92, 2.42, 2.77, 3.10, 3.58

Shock wave speeds are varied by the aeration level of the bubbly liquid, where higher

eration levels result in lower shock wave speeds. The overall mean absolute error (MAE) for the smaller and larger impact velocities are 4.2 m/s and 3.8 m/s for impact velocities 0.85 m/s and 1.70 m/s, respectively, where the MAE is calculated by $(1/N) \sum_i^N |U_s - U_{s,ref}|/N$. This corresponds to 2.1 and 1.9 % of the average shock speed of 200 m/s. Even for relatively high aeration levels around 3.5 %, the image processing is still able to determine the time instances of shock wave arrival robustly and to provide accurate shock wave speeds. The variance around the black dotted line increases for higher U_s , as this region indicates lower aeration level and fewer bubble images are present. This imaging method is limited by the availability of observed bubbles in both FOVs, and thus cannot be applied to single-phase liquids.

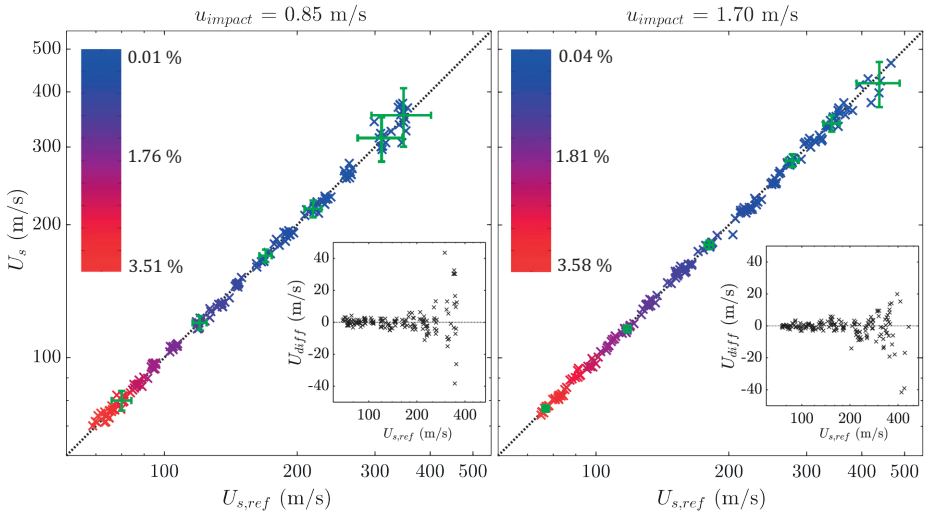


Figure 3.8: Comparison between the shock wave speeds measured by the imaging-based method (vertical axis) and by the pressure transducers (horizontal axis). The green error bars illustrate ± 2 standard deviations and are computed based on the realisations of ten measurements within one void fraction group.

SHOCK WAVE PRESSURES

Shock wave pressures are estimated from the model and compared with the reference pressure transducers (Fig. 3.9). The mean absolute error (MAE) is computed by $(1/N) \sum_i^N |P_{calc,i} - P_{exp,i}|$ and is 12.6 kPa for the lower impact velocity (159 measurements) and 28.3 kPa for the higher impact velocity (173 measurements). Deviations in shock wave pressures are relatively small for lower pressure magnitudes, while the variance increases for larger pressure magnitudes. PIV measurements are performed to investigate the source of the variances in the shock pressure in more detail. The slip velocity between the bubbles and liquid (u_{slip}) forms an important mechanism in the model,

and two-phase PIV measurements allow for the simultaneous investigation of the bubble and surrounding liquid velocities upon the arrival of the shock front.

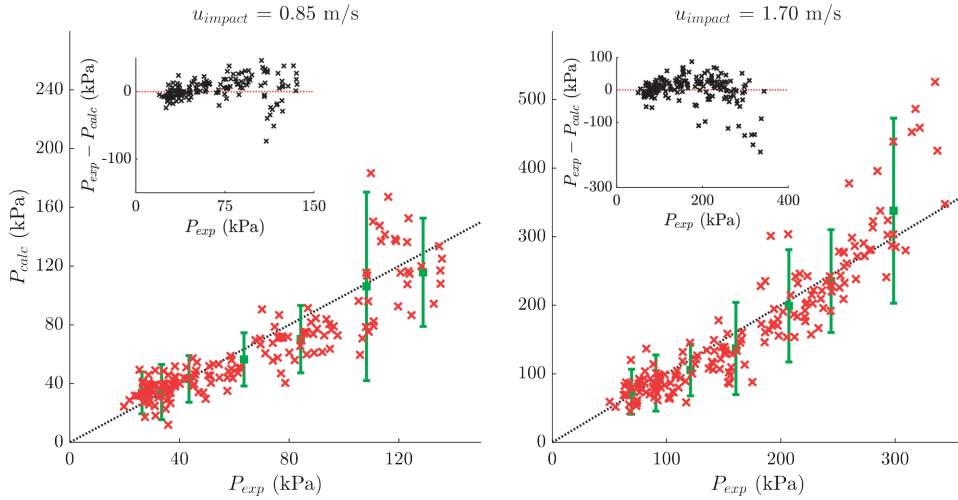


Figure 3.9: Comparison between the pressure magnitude (in kPa) obtained directly from the pressure transducers (horizontal axes) and the computed pressure magnitude (in kPa) by the present model for $u_{\text{impact}} = 0.85 \text{ m/s}$ (left) and 1.70 m/s (right). The 7 error bars (green vertical lines) represent ± 2 standard deviations, and are constructed by first sorting the data in ascending order for P_{exp} , then divided into 7 groups of circa 25 measurements each, followed by calculating the mean and standard deviations for each group.

TWO-PHASE PIV MEASUREMENTS

PIV measurements were performed to validate the shock-induced liquid acceleration. A typical recording is shown in the supplementary material, both in a raw and processed format (with u_l and u_b shown as vectors). Necessary changes to the optical arrangement in the experimental setup are made to perform these planar PIV measurements (Fig. 3.2), but other components of the system remained identical. In total, 54 impacts were recorded ranging from 0 to 1.0 percent aeration and two impact velocities of 0.85 and 1.70 m/s. Note that the shock-induced liquid velocities are clustered; see Fig. 3.10. Also, the model predictions show a smaller bias, i.e. $\bar{u}_{\text{model}}/\bar{u}_{\text{PIV}} = 1.062$ and 0.916 , while $\bar{P}_{\text{model}}/\bar{P}_{\text{ref}} = 1.095$ and 0.828 , for 0.85 and 1.70 m/s respectively. Since $\Delta P_l = \Delta P_l(\rho_l, U_s, \Delta u_l)$, i.e. the Joukowsky equation, where U_s is accurately measured (see Fig. 3.8) and the maximum error for ρ_l is 1.0 percent (the upper range of the void fraction), most deviations in Fig. 3.9 are expected to originate from the computed shock-induced liquid velocities. Also, the emitted pressures from collapsing and expanding bubbles may have an effect on the overall pressure signal; see Fig. 3.7. This is supported by Fig. 3.10 (right), where the model consistently under predicts the shock pressure, as

single bubble dynamics models (such as the Rayleigh-Plesset model) are not included. On the other hand, Fig. 3.9 shows that the largest deviations occur for lower aeration levels, where fewer bubbles are present. Also, Fig. 3.7 (left) shows that no typical higher frequency pressure variations of smaller bubbles are observed in that specific measurement with $\alpha = 0.084 \%$.

3

Only for the PIV measurements, the shock speed is derived from the reference pressure transducers. The shock wave speed U_s cannot be determined by these larger non-split images, as the back-light illumination would overexpose the emitted light by the tracer particles. Since U_s can accurately be determined by the reference pressure transducers (Fig. 3.8), this model input variable is expected to contribute marginally to the model output variance.

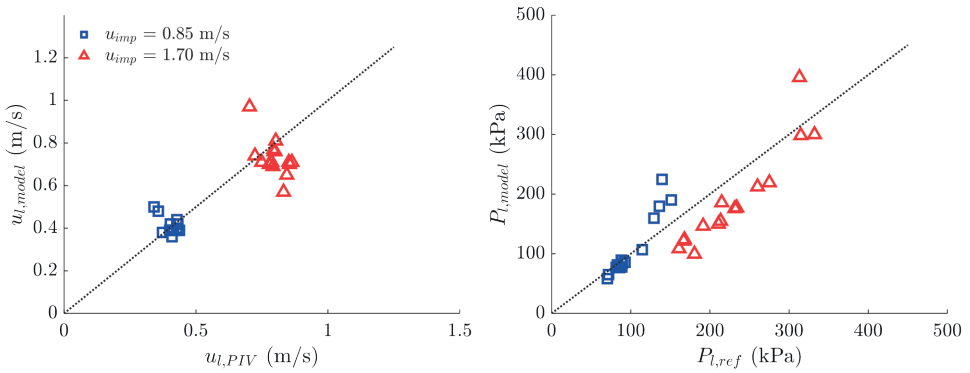


Figure 3.10: Left: The experimentally determined shock-induced liquid velocities are obtained with PIV measurements (horizontal axis), while $u_{l,model}$ is calculated by the model. Right: The associated shock pressures that follow from the reference pressure transducers (horizontal axis), and the calculated shock pressures by the model.

The synchronized bubble and liquid velocities during the shock passage are shown in Fig 3.11 (left), where the arrows (a-e) refer to the corresponding images in Fig. 3.12. Time $t = 0$ ms (b) corresponds to the image in which the average bubble velocity intersects with the zero velocity threshold. As expected, bubbles initially accelerate faster than the surrounding liquid and decelerate afterwards, and compress in response to the elevated shock pressures. Furthermore, the shock wave front passage through the gas-liquid fluid is observed within one image by the acceleration of the liquid (Fig. 3.12, c), from which the shock wave speed is estimated from the liquid velocity profiles along the vertical location of the FOV in Fig. 3.11 (right). For $\Delta y = 42$ mm and $\Delta t = 100 \mu s$ (consecutive frames), the estimated shock wave speed is 420 m/s, which reasonably approximates the measured shock wave speed of 411.4 m/s by the reference measurement.

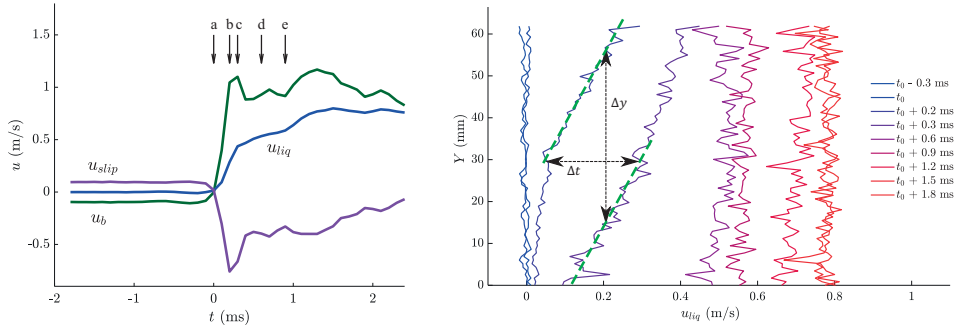


Figure 3.11: Left: liquid (blue), bubble (green) and slip (purple) velocity profiles during the shock wave passage. Letters (a) to (e) correspond to the images in Fig. 3.12. Right: instantaneous velocity profile of the fluid tracer particles. Interestingly, the shock wave front is captured in the center of image $t + 0.2$ ms at $Y = 30$ mm. The shock wave front is also indicated in Fig. 3.12 (b) by the purple dotted line.

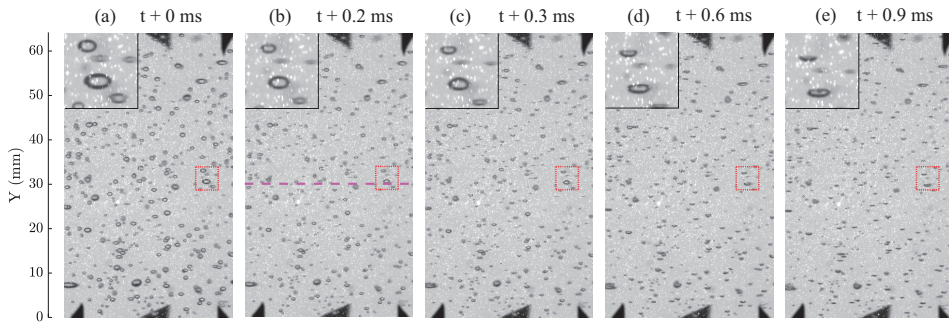


Figure 3.12: Five consecutive two-phase PIV images at the shock wave passage. Bright spots indicate fluid tracer particles, while darker spots represent bubbles. The shock wave front is observed in frame (b) at $t=0.2$ ms (indicated by the purple dotted line) and corresponds to $t+0.2$ ms in Fig. 3.11 (right). The liquid accelerates at the top of the image, while being still quiescent at bottom. The inset enlarges bubbles (from the red encircled region) and their response to the shock wave passage corresponds to the schematic representation in Fig. 3.1.

3.5. CONCLUSIONS AND OUTLOOK

This article presents a novel experimental imaging-based method to determine shock characteristics (i.e. shock wave speed and magnitude, and shock-induced liquid velocity), non-intrusively and solely from gas bubble velocities. The model is validated by pressure transducers and two-phase PIV measurements. We conclude that the proposed method with a split FOV is capable of accurately measuring the shock wave speed U_s in the range of $70 < U_s < 400$ m/s (with MAE of 4.2 and 3.8 m/s). Compared to the PIV measurements, the model is able to estimate the shock-induced liquid velocity within a reasonable margin of error, as validated by PIV for two different impact velocities. Measuring the maximum shock wave pressure of transient shocks remains challenging and incurs the largest relative uncertainties. As the model does *not* include single bubble

dynamics, and therefore pressure oscillations by single bubbles, such as the observed high-frequency perturbations on the 'global' pressure profile in Fig. 3.7 (right), cannot be computed by the current model. This may explain why the maximum shock wave pressure deviates more than the shock-induced liquid velocity from the reference measurements, even though they are interdependent by the Joukowski equation. Furthermore, the liquid velocity is mostly affected by the 'global' pressure wave profile, irrespective of the radiated pressure by oscillating bubbles (which does affect the maximum observed pressure), so that the deviation between observed liquid velocity (by the PIV reference measurements) and the computed liquid velocity by the model would be less.

The advantages of the proposed method include (1) the absence of flush-mounted intrusive pressure transducers; (2) no volumetric bubble reconstruction is required and thus applicable to larger void fractions; (3) by splitting the camera field-of-view, minimal optical access is required (using two small optical windows), and we enhance the dynamic range (DVR x DSR) of the measurement significantly, allowing for increased measurement accuracy for the shock wave speed; (4) the flow remains unaltered, i.e. no addition of particles or objects, because bubbles are naturally present in bubbly gas-liquid fluids; (5) the region of interest can be chosen anywhere in the flow (and not exclusively to the wall region); (6) the possibility to apply in high-temperature and/or high-pressurized flows; and (7) this method may serve a shock wave detection system.

The method is based on a limited number of assumptions which may be addressed in future research, most notably the (1) initial quiescent liquid ($u_{l,o} \approx 0$), (2) constant gradient dP/dy between the arrival and maximum pressure magnitude, and (3) sphericity of bubbles. Non-ideal circumstances may lead to additional measurement uncertainty. The effect of larger void fractions beyond our experimental range (3.5 %) is difficult to estimate. On the one hand, the rise velocity of a swarm of (large) gas bubbles may exceed the rise velocity of isolated bubbles (Krishna et al., 1999) which violates the equation of motion for isolated bubbles (Eq. 3.7), as the liquid has initial bubble-induced turbulence (no longer quiescent), and larger bubbles deform into non-spherical shapes. Also, the mixture density ρ_0 is currently approximated by the liquid density ρ_l for dilute mixtures. However, it is possible to extend the current model for larger void fractions by estimating the void fraction from the camera images (when recording over a longer period) and locally by using defocused imaging (Cornel et al., 2018), or numerically model the relation between covered pixels by bubbles and the associated expected void fraction by a Monte Carlo simulation.

BIBLIOGRAPHY

- Adrian, R., & Westerweel, J. (2011). *Particle image velocimetry*. Cambridge University Press.
- Ando, K., Sanada, T., Inaba, K., Damazo, J. S., Shepherd, J. E., Colonius, T., & Brennen, C. E. (2011). Shock propagation through a bubbly liquid in a deformable tube. *J. Fluid Mech.*, 671, 339–363.
- Batchelor, G. (2000). *An introduction to fluid dynamics*. Cambridge University Press.
- Campbell, I. J., Pitcher, A. S., & Temple, G. F. J. (1958). Shock waves in a liquid containing gas bubbles. *Proc R Soc Lon Ser-A*, 243(1235), 534–545.
- Cornel, W. A., Westerweel, J., & Poelma, C. (2018). Local microbubble concentration by defocused volumetric shadowgraphy with a single camera. *Proc. 18th Int. Symp. on Flow Visualization, June 26-29, 2018, Zürich*.
- Frolov, S. M., Avdeev, K. A., Aksenov, V. S., Borisov, A. A., Frolov, F. S., Shamshin, I. O., Tikhvatullina, R. R., Basara, B., Edelbauer, W., & Pachler, K. (2017). Experimental and computational studies of shock wave-to-bubbly water momentum transfer. *Int. J. Multiphase Flow*, 92, 20–38.
- Frolov, S. M., Avdeev, K. A., Aksenov, V. S., Sadykov, I. A., Shamshin, I. O., & Frolov, F. S. (2022). Interaction of Shock Waves with Water Saturated by Nonreacting or Reacting Gas Bubbles. *Micromachines*, 13(9), 1553.
- Ghidaoui, M. S., Zhao, M., McInnis, D. A., & Axworthy, D. H. (2005). A review of water hammer theory and practice. *Appl. Mech. Rev.*, 58(1), 49–76.
- Gluzman, I., & Thomas, F. O. (2022). Image-based characterization of the bubbly shock wave generation and evolution in aviation fuel cavitation. *Phys. Rev. Fluids*, 7(8), 084305.
- Hayasaka, K., Tagawa, Y., Liu, T., & Kameda, M. (2016). Optical-flow-based background-oriented schlieren technique for measuring a laser-induced underwater shock wave. *Exp. Fluids*, 57(12), 179.
- Horvat, D., Agrež, V., Požar, T., Starman, B., Halilovic, M., & Petkovšek, R. (2022). Laser-induced shock-wave-expanded nanobubbles in spherical geometry. *Ultrason Sonochem*, 89, 106160.
- Jakeman, D., Smith, B. L., & Heer, W. (1984). *Propagation of pressure waves through air-water mixture* (tech. rep.). Eidg. Institut for Reaktorforschung Wurenlingen.
- Kalra, S. P., & Zvirin, Y. (1981). Shock wave-induced bubble motion. *Int. J. Multiphase Flow*, 7(1), 115–127.
- Kameda, M., Shimauro, N., Higashino, F., & Matsumoto, Y. (1998). Shock waves in a uniform bubbly flow. *Phys. Fluids*, 10(10), 2661–2668.

- Kim, M., Lee, J. H., & Park, H. (2016). Study of bubble-induced turbulence in upward laminar bubbly pipe flows measured with a two-phase particle image velocimetry. *Exp. Fluids*, 57(4), 55.
- Krishna, R., Urseanu, M. I., van Baten, J. M., & Ellenberger, J. (1999). Rise velocity of a swarm of large gas bubbles in liquids. *Chem. Eng. Sci.*, 54(2), 171–183.
- Lau, Y. M., Deen, N. G., & Kuipers, J. A. M. (2013). Development of an image measurement technique for size distribution in dense bubbly flows. *Chem. Eng. Sci.*, 94, 20–29.
- Lee, H., Gojani, A. B., Han, T.-h., & Yoh, J. J. (2011). Dynamics of laser-induced bubble collapse visualized by time-resolved optical shadowgraph. *J. Vis*, 14(4), 331–337.
- Li, J., Shao, S., & Hong, J. (2020). Machine learning shadowgraph for particle size and shape characterization. *Meas. Sci. Technol.*, 32(1), 015406.
- Lindken, R., & Merzkirch, W. (2002). A novel PIV technique for measurements in multi-phase flows and its application to two-phase bubbly flows. *Exp. Fluids*, 33(6), 814–825.
- Magnaudet, J., & Eames, I. (2000). The Motion of High-Reynolds-Number Bubbles in Inhomogeneous Flows. *Annu. Rev. Fluid Mech.*, 32(1), 659–708.
- Mei, R. (1996). Velocity fidelity of flow tracer particles. *Exp. Fluids*, 22(1), 1–13.
- Mur, J., Reuter, F., Kočica, J. J., Lokar, Ž., Petelin, J., Agrež, V., Ohl, C.-D., & Petkovšek, R. (2022). Multi-frame multi-exposure shock wave imaging and pressure measurements. *Opt. Express*, 30(21), 37664–37674.
- Noordzij, L., & Van Wijngaarden, L. (1974). Relaxation effects, caused by relative motion, on shock waves in gas-bubble/liquid mixtures. *J. Fluid Mech.*, 66(1), 115–143.
- Salibindla, A. K., Masuk, A. U. M., & Ni, R. (2021). Experimental investigation of the acceleration statistics and added-mass force of deformable bubbles in intense turbulence. *J. Fluid Mech.*, 912, A50, 1–19.
- Schmitt, C., Pluvinaud, G., Hadj-Taieb, E., & Akid, R. (2006). Water pipeline failure due to water hammer effects. *Fatigue Fract Eng M*, 29(12), 1075–1082.
- Takagi, S., & Matsumoto, Y. (1996). Force acting on a rising bubble in a quiescent liquid. *Am. Soc. Mech. Eng. Fluids Eng. Div. Newsl.*, 236, 575–580.
- Tijsseling, A. S. (2007). Water hammer with fluid–structure interaction in thick-walled pipes. *Comput. Struct.*, 85(11), 844–851.
- Turton, R., & Levenspiel, O. (1986). A short note on the drag correlation for spheres. *Powder Technol.*, 47(1), 83–86.
- Van Wijngaarden, L. (2007). Shock waves in bubbly liquids. *Shock wave science and technology reference library: Multiphase flows i* (pp. 3–33). Springer Berlin Heidelberg.
- Vogel, A., Busch, S., & Parlitz, U. (1996). Shock wave emission and cavitation bubble generation by picosecond and nanosecond optical breakdown in water. *J. Acoust. Soc. Am.*, 100(1), 148–165.
- Westerweel, J., Elsinga, G. E., & Adrian, R. J. (2013). Particle image velocimetry for complex and turbulent flows. *Annu. Rev. Fluid Mech.*, 45(1), 409–436.

4

ENERGY PARTITIONING OF CLOUD CAVITATION COLLAPSES VIA TIME-RESOLVED X-RAY DENSITOMETRY

The energy partitioning during the final collapse stage of vapor bubble clouds in a cavitating venturi is studied. In the experiments, we quantitatively relate the evolution of potential bubble energy to the emitted shock wave energy and rebound energy. Instantaneous vapor cloud structures are recorded by time-resolved X-ray densitometry measurements during the full shedding cycle at frame rates of 12 and 25 kHz, and the emitted shock waves are simultaneously registered by synchronized high-frequency pressure transducers to measure the emitted shock wave energy. Potential cavity energy is partitioned (via liquid kinetic energy) into shock wave energy, dissipative thermal energy, rebound energy, and complex flow behavior (such as impinging liquid micro-jets). In total, 684 vapor bubble cloud collapses are recorded spanning 8 different parameter sets of cavitation numbers ($0.41 < Ca < 0.71$) and system pressures ($35.9 < P_\infty < 71.0$ kPa). On average, between 24 and 56 percent of the initial potential cavity energy E_{pot} is converted into shock wave energy E_s for coherent cloud cavitation in our experimental range. For constant added kinetic energy to the flow, we found that both the energy conversion, and the amount of E_{pot} and E_s increase for decreasing cavitation number. Also, by keeping the cavitation number constant, it appears that relatively more energy is partitioned into shock wave energy for increasing surrounding pressures.

4.1. INTRODUCTION

Cavitation is the phenomena in which condensable bubbles are formed in a liquid in regions where the pressure drops below the vapor pressure, often caused by hydrodynamic effects. Cloud cavitation is a type of cavitation where many vapor bubbles are in close proximity to each other forming clouds, which may cause severe cavitation noise and erosion upon collapse. Cloud cavitation flows have been studied extensively near wedges (Furness & Hutton, 1975; Petkovšek et al., 2020; X. Wu et al., 2017), hydrofoils (Coutier-Delgosha et al., 2007; Huang et al., 2013; Kubota et al., 1989; Leroux et al., 2005; Reisman et al., 1998; H. Zhang et al., 2021), venturis (G. H. Chen et al., 2015; Ganesh et al., 2016; Jahangir et al., 2019; Stutz & Reboud, 1997; Xu et al., 2020), and backward facing steps (Maurice et al., 2021). Once vapor bubbles are advected to regions where the local pressure P exceeds the vapor pressure P_{vap} , the bubbles collapse violently and the surrounding liquid accelerates towards the vapor bubble centers. During the collapse stage, bubbles at the outer region of the cloud collapse first for sufficiently large vapor fraction and initial cloud radius (Y.-C. Wang & Brennen, 1995). During the collapse, potential energy is converted to kinetic energy of fluid moving inward. Shock waves are generated from the cloud collapse in the flow region where the pressure recovers (G. Chen et al., 2015; Y.-C. Wang & Brennen, 1995; Z. Wang et al., 2021; Yamamoto, 2016). These events are responsible for material erosion and vibrations (Bourne, 2002; Knapp, 2022; Sarkar et al., 2021; Z. Wang et al., 2021). Typically, the pressure profiles of these radiated shock waves are characterized by a large pressure peak and short duration (Brujan et al., 2012; Ceccio & Brennen, 1991; Kumar & Brennen, 1993; Reisman et al., 1998; Y.-C. Wang & Brennen, 1995). The interaction between bubbles complicates the problem (Y.-C. Wang & Brennen, 1995). The large dynamic range in spatial and temporal scales make it difficult to resolve the flow physics numerically. Also, the assessment of cavitation erosion risk from numerical flow simulation is still a major challenge (Schenke et al., 2019).

We gain a better understanding of these complex flow events by quantifying the partitioning of energy during the final collapse stage of cavitation clouds. Tinguely et al. (2012) describes the partitioning of potential cavity energy (E_{pot}) via kinetic energy (E_{kin}) into shock wave energy (E_s), internal energy (U), and rebound energy ($E_{kin,reb}$). Obreschkow et al. (2011) shows that micro-jets are formed during the collapse and rebound stages of cavitation bubbles subject to a pressure gradient. Several models are based on this energy cascade mechanism, including Schenke et al. (2019) and Melissaris et al. (2019). Due to asymmetries in the collapse, Schenke et al. (2019) suggest that some residual kinetic energy may remain in the flow and result in complex flows such as impinging liquid

jets. The initial potential energy of imploding vapor structures is proportional to the initial cavity volume ($V_{vap,0}$) and the driving pressure (P_d), which is the difference between the pressure in the surrounding liquid (P) and the vapor pressure (P_{vap}) (Brennen, 1995; Vogel & Lauterborn, 1988). According to Tinguely et al. (2012), the conversion of potential energy into dissipative thermal energy U is negligible, and non-condensable gas in the bubble may cause rebounds. The rebound energy is only significant at low ambient pressures, far below atmospheric pressure (Tinguely et al., 2012). Since our experiments are performed at pressures of $40 < P < 70$ kPa, thus below atmospheric pressure, the rebound energy partition might be relevant. For a spherical single bubble collapse, Supponen et al. (2017) found that 80-90 % of the potential cavity energy is transferred into shock wave energy and less than 10 percent into rebound energy. Wen et al. (2023) found for a single laser-induced millimeter-sized spherical cavitation bubble that 89.7 percent of the initial potential energy is transferred into shock wave emission, while 6.2 percent is transferred into rebound energy; the resulting 4.1 percent of the energy is transferred into condensation and viscous damping.

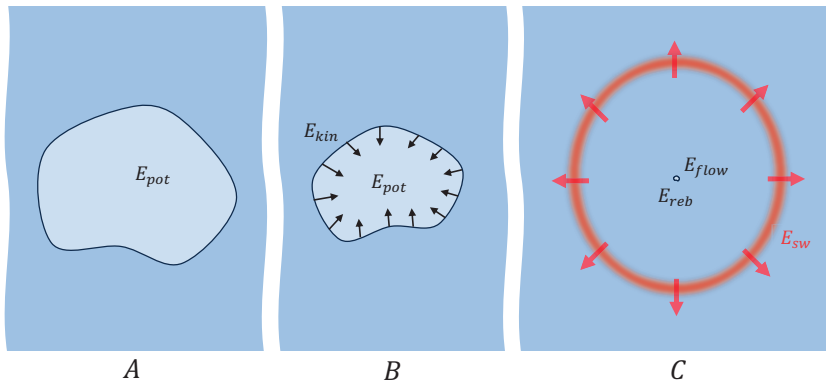


Figure 4.1: Schematic overview of the energy conversion: initial cavity potential energy (A) is converted into liquid kinetic energy (B) and subsequently into shock waves energy and other types of energy (C).

Quantifying the evolution of the global cavitation cloud structures with synchronized pressure data is key to partitioning the initial potential cavity energy into shock wave energy, rebound energy, internal energy and kinetic energy absorbed by complex flow behaviour. In practice it is very difficult, or even impossible, to study large collapsing vapor clouds by shadowgraphy. For example, G. H. Chen et al. (2015) and G. Chen et al. (2015) documented the evolution of the projected cavity area (A/A_{max}) by high-speed imaging (3000 frames per second), while Hutli et al. (2019) studied the vapor cloud dy-

4

namics by shadowgraphy (100 kfps), but both were not able to resolve the cavity volume. G. H. Chen et al. (2015) observed that the decrease in volume of a large detached cavity, while gradually moving downstream, was followed by an increase in pressure fluctuations. Jung et al. (2009) experimentally studied the correlation between cavitation and pressure fluctuations using pressure sensors and a high-speed camera. Although the projected geometrical shapes can be estimated by shadowgraphy, quantitative information on the vapor fraction is more complex (Dash et al., 2018). For this purpose, high-speed X-ray densitometry is more appropriate: the two distinct advantages over shadowgraphy in optically opaque multi-phase flows are (1) the full capture of the vapor fraction and cavity volume, i.e. no image saturation at high vapor fractions (Mäkiharju et al., 2017), and (2) X-ray beams remain unrefracted between the source and detector, whereas rays in the visual part of the spectrum suffer strongly from differences in the refractive index between vapor and liquid.

Pike et al. (1965) were among the first to apply X-ray densitometry to measure vapor fractions in a steam-water mixture. More recently, Stutz and Legoupil (2003) employed X-ray densitometry to describe cloud cavitation by measuring the instantaneous volume fraction of the vapor phase, and compare these to optical measurements. They conclude that both measurement techniques agree within their uncertainty ranges. Mäkiharju et al. (2013) developed a two-dimensional X-ray densitometry system to measure the void fraction distribution in gas-liquid flows, and characterized the most important sources of uncertainty. X-ray based methods have been employed to study complex opaque flows, such as unsteady cavitating flows around a 2D foil section (Coutier-Delgosha et al., 2007), partial cavity dynamics around a NACA0015 hydrofoil (J. Wu, 2019), sheet-to-cloud transitions for partial cavities (Ganesh et al., 2016), characterizing topology features and different cavitation regimes in high-speed nozzle flows (Karathanassis et al., 2021), cavitating backward facing step flow (Maurice et al., 2021), to demonstrate the presence of significant slip velocities between phases within sheet cavities (Khelifa et al., 2017), and the effect of injected non-condensable gas on the shedding natural cavity flow (Mäkiharju et al., 2017). Jahangir et al. (2019) and Bauer et al. (2018) measured the void fraction distributions in a venturi flow by X-ray computed tomography to study the internal structures of cavitating flows, while G. Zhang, Khelifa, and Coutier-Delgosha (2020) and G. Zhang, Khelifa, Fezzaa, et al. (2020) studied the internal flow structures and dynamics of quasi-stable sheet cavitation. Extensive reviews were recently published on X-ray flow visualization in multiphase flows (Aliseda & Heindel, 2021; Heindel, 2011) and on X-ray measurement techniques applicable to wall-bounded cavitating flows (Heidari-

Koochi et al., 2021).

In the current research, we perform temporally-resolved X-ray densitometry measurements to quantify vapor fractions and volumes. We focus on the flow region where the shed vapor clouds collapse. The vapor creation and the attached vapor sheet are not considered here. Previous studies could not resolve the internal structure of cavitating flows during the final stage of the collapse as this requires a high temporal resolution. In this paper we report on novel experimental data that provide a quantification of energy partitioning for coherent cloud cavitation in a cavitating flow for various cavitation numbers Ca and ambient pressures P_∞ . Several researchers have numerically and theoretically studied the dynamics and emitted shock waves of a cavitating bubble cloud (Büdich et al., 2018; Du et al., 2016; Furness & Hutton, 1975; Melissaris et al., 2019; Rasthofer et al., 2017; Schenke et al., 2019; Schnerr et al., 2008; Y.-C. Wang & Brennen, 1995; Z. Wang et al., 2021). Our experimental data with sub-millimeter spatial and sub-millisecond temporal resolution on the cavity structures with synchronically measured pressure data can further be used to validate computational studies on shock wave emissions from cloud cavitation collapses. Furthermore, these results may be used to develop models that predict impact loads from shock waves originating from collapsing vapor bubble clouds in liquids.

The article is organised as follows: The subsequent section describes the experimental setup and processing of the X-ray and pressure data. Section 4.3 elaborates on the data processing of the X-ray images, system and pressure data, and synchronization. Section 4.4 begins with the instantaneous vapor volumes during the final collapse stage. Since the cavitation in the Venturi is cyclic, we describe the phase-averaged vapor volume and synchronically measured pressure in time. Next, the computed potential energy, shock-wave energy and rebound energy are discussed, followed by an analysis of the various contributions to these energies. The limitations of this research are discussed in section 4.5, and section 4.6 summarizes our main findings.

4.2. HIGH-SPEED X-RAY FACILITY (HSX)

The X-ray densitometry measurements are performed at the TNO research institute (The Hague-Ypenburg, the Netherlands). The measurements are performed in a convergent-divergent venturi as described by Jahangir et al. (2018), which has an 18.0 degrees convergent angle and an 8.0 degrees divergent angle. Figure 4.2 shows the measurement section of the closed-loop cavitation facility. Vapor cavities are generated when the lo-

cal pressure drops below the vapor pressure by accelerating the liquid in the convergent part of the venturi. The local pressure recovers in the divergent part downstream of the throat, where the vapor cavities collapse. Upstream and downstream the Venturi is connected to a cylindrical pipe with a diameter of 50 mm, and the Venturi area contraction ratio for the throat is 9. By comparing the dimensionless shedding frequency, or Strouhal number (St) as a function of the cavitation number (Ca) to the data reported by Jahangir et al. (2018), we conclude that our experimental data and findings can directly be compared to their study.

4

The HSX-facility (“High-Speed X-ray”) is equipped with an advanced densitometry system that allows for high-speed recordings of cavitating flows. The X-ray source (Varian Medical Systems, A-292 rotating anode X-ray tube) is powerful enough to allow for capturing images at 25 kHz. To avoid damage due to heat production in the anode, the X-ray source (710 mA, 40 keV) is limited to radiate for maximum duration of 0.63 seconds. In our experiments this corresponds to approximately 30 unique cloud collapse cycles per recording. The use of X-ray imaging requires strict safety measures: The entire setup is located in a bunker with 1-meter thick concrete walls, and operated and monitored from a remote control room. The X-ray beam is able to pass through the medium in

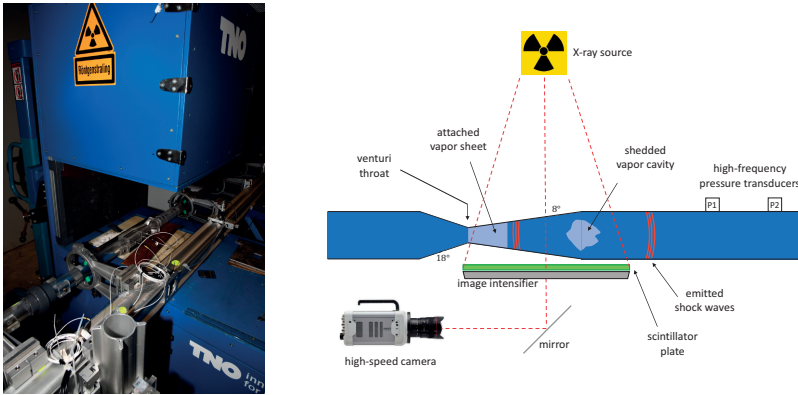


Figure 4.2: Picture (left) and schematic overview (right) of the measurement section of the X-ray densitometry setup at TNO (not to scale). Photo courtesy of Frits Hilvers (TNO).

straight rays, and thus avoids complications encountered when using light in the visual part of the spectrum. Absorption of the X-rays by the medium depends on the mass attenuation coefficient. An image intensifier behind the scintillator plate amplifies the light emitted by the scintillator plate, which is then recorded by the electronic sensor of a high-speed camera (Photron FASTCAM NOVA S16). The combined response time of the

X-ray source, scintillator plate and image intensifier is of the order of $20 \mu\text{s}$. The camera is focused on the surface of the image intensifier with a spatial resolution of 0.262 mm/px . The intensity in the recorded images can be related to the fraction of photons absorbed by the material through which the X-rays passed, which is proportional to the material density. Image parts with high intensities (i.e. many counts) represent X-ray paths that contain material with a low integrated mass attenuation coefficient, such as gas and vapor. Image parts with a low intensity (i.e., low counts) represent denser material, such as water and metals, as illustrated in Figure 4.3. X-ray densitometry allows for quantifying vapor fraction α by (Mäkiharju et al., 2013):

$$\alpha = \ln\left(\frac{I}{I_{full}}\right) / \ln\left(\frac{I_{empty}}{I_{full}}\right), \quad (4.1)$$

where I represents the image intensity (i.e., digital image count), and the subscripts ‘full’ and ‘empty’ refer to the water-filled and empty tubes, respectively. These intensities are determined in a two-point calibration procedure prior to the measurements (Mäkiharju et al., 2013). For both ‘full’ and ‘empty’, 1,000 images are recorded at camera rates of 12 and 25 kHz, and subsequently time-averaged to suppress the noise in the amplified scintillation images.

The system pressure is lowered to 40 kPa by a vacuum pump and the flow loop is run for 45 minutes before the calibration and measurements to ensure that the non-condensable gas content is removed from the water in the system. Once degassed, the water was not replaced during the entire experiment.

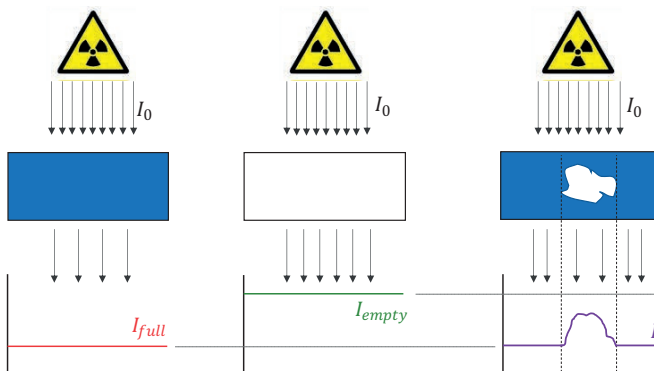


Figure 4.3: Graphical explanation of computing the vapor fraction from X-ray absorption. In the rectangle, blue indicates the liquid phase and white the vapor phase. The vapor fraction is computed by Eq. (4.1).

Three flush-mounted pressure transducers (PCB piezoelectric model 102B) with resonance frequency ≥ 500 kHz are installed to record the pressure magnitude of emitted shock waves P_s , that originate from the vapor cavity collapses. The transducers are located 257, 607, and 1057 mm, respectively, downstream from the venturi throat, or $x/D \approx 5, 12, \text{ and } 21$. The surface in contact with the liquid is approximately 24 mm^2 , and the sensitivity is 0.15 mV/kPa . The signals are sampled digitally by a data acquisition board (National Instruments) and recorded at a sampling frequency of 100 kHz . While the general shape of the pressure peaks are captured, the finite sampling rate may introduce a small underestimation for the very short, intense pulses ($< 10 \mu\text{s}$). The recorded pressure magnitudes are used for determining (1) the shock wave speed U_s , (2) shock pressure magnitude P_s , (3) the shock energy E_s , and (4) the shedding frequency f . The images and pressure data are measured simultaneously, allowing to couple observed pressure profiles to the images. The maximum time registration error is one camera frame, thus 40 and $83 \mu\text{s}$ for 25 and 12 kHz , respectively. The uncertainty in the simultaneous registration between the camera and pressure transducers is negligible compared to the cloud cavity collapse time of approximately 1 ms . By using three transducers it is possible to validate that the shock waves initially originate from the vapor collapses by considering the arrival times of the shock wave at each of the three transducers.

The system pressure P_∞ , liquid temperature T , and flow rate Q_v are recorded simultaneously during the X-ray measurements to accurately characterize the cavitation regime. Furthermore, the saturated vapour pressure P_{vap} and the densities of saturated vapour ρ_{vap} and liquid ρ_{liq} are computed from the equations by Grigull and Schmidt (1989) and Büdich et al. (2018). The flow velocity at the throat u_{th} follows from the flow rate divided by the throat cross section $\frac{\pi}{4}d^2$, where the throat diameter is 16.7 mm . The vapor pressure and density are used to calculate the cavitation number $Ca = 2(P_\infty - P_{vap})/\rho_{liq}u_{th}^2$. The characteristic frequency in the Strouhal number $St = fD/u_{th}$ is identified in the power spectrum of the recorded pressure magnitude signal of transducer 1, which is located closest to the pressure recovery section. The flow conditions for all measurements are tabulated in Appendix 1.

Figure 4.4 provides an overview of the parameter space that is covered by the experiments (Ca, P_∞). These regimes are set by varying the system pressure and the flow velocity (u_{th}). Within each measurement of 0.63 seconds, changes in the system pressure, flow velocity and liquid temperature are found to be negligible, as these system parameters are recorded during each measurement. The kinetic energy per volume $\rho_{liq}u_{th}^2/2$ is

nearly constant for $(Ca, \bar{P}_\infty) = (0.42, 42), (0.49, 51), (0.6, 60)$ and $(0.7, 70)$, represented by the red dashed line in Figure 4.4. For these measurements, the added kinetic energy to the system is comparable, i.e. $u_{th} \approx \text{constant}$. The other parameter sets are recorded to study the effect of the system pressure P_∞ and flow u_{th} independently, represented by the black dashed and dash-dotted lines.

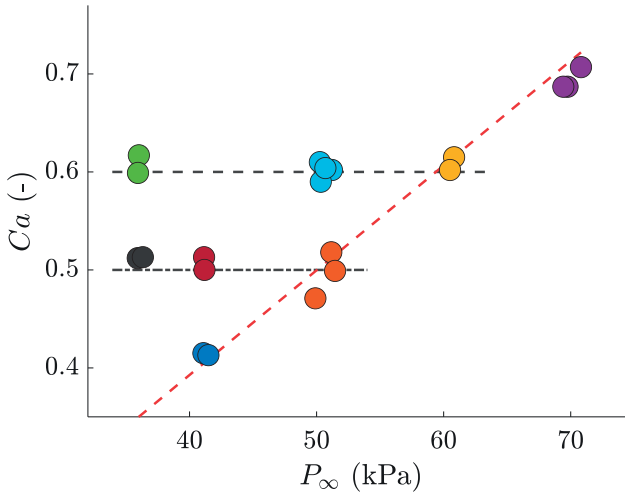


Figure 4.4: Parameter space (Ca, P_∞) of the performed experiments. Each data point represents an X-ray measurement recording of 0.63 seconds, corresponding to approximately 23 to 48 collapse cycles, depending on the cavitation number. Individual measurements with similar marker color represent measurements under comparable conditions. The dashed red line corresponds to constant kinetic energy per unit volume for $u_{th} = 13.7$ m/s, and the black lines to $Ca = 0.6$ (dashed) and $Ca = 0.5$ (dash-dotted).

4.3. DATA PROCESSING

Each measurement set results in (1) images captured by the high-speed camera, (2) the emitted shock wave magnitude by the high-frequency pressure transducers, and (3) system control parameters including the system pressure, flow and temperature (see section 4.2). This section describes the processing of these experimental data in detail.

4.3.1. IMAGE DATA

Figure 4.5 shows the four steps in the image data processing: (1) filtering, (2) image cropping and masking, and the conversion from intensity to (3) vapor fraction and (4) Vapor content integrated along the ray passing through the measurement section, referred to as ‘vapor thickness’. The recorded high-speed images (see section 4.2) are stored in uncompressed TIFF format (400×1024 px, 16-bit) and imported in MATLAB (version

R2018b). First, the images are spatially low-pass filtered and to reduce the impact of dead/hot pixels (Adrian & Westerweel, 2011) by a 2D median filter of 3×3 px, resulting in the spatial cutoff frequency in the order of 1 mm. Although vapor clouds are readily observable in the noisy images recorded at 25 kHz further image processing is needed. Therefore, the signal-to-noise ratio is further improved by applying a temporal central mean filter over 11 and 5 adjacent images for the 25 and 12 kHz recordings, respectively. This lowers the effective frequency to approximately 2300 Hz. This is still sufficient to resolve the vapor collapses.

4

Next, the filtered images are masked and cropped (from 400×1024 px to 241×900 px) to only retain the relevant FOV. To avoid inconsistencies by the 3×3 px median filter for pixels located at the edges of the image, the entire image is first filtered and then cropped. The venturi wall is masked and excluded from further data processing. The wall is clearly identified by recognizable objects, such as the pressure transducers. We limit the number of images per measurement to 14,700 images for the 25 kHz and 7056 images for the 12 kHz recordings, both corresponding to 0.588 seconds. This way, the non-steady initial startup phase of the X-ray source is excluded from the measurements. Unlike the camera and pressure transducers, the X-ray source has no external trigger option and is triggered manually. Therefore, the reference time instance for synchronizing the camera images and X-ray source phase is defined by the characteristic sharp decline in the intensity profile at the turn-off of the X-ray source. We set an intensity threshold of 300 counts for the mean intensity of a selected region in the image. It was consistently observed that the intensity slightly increases by $\mathcal{O}(1\%)$ during each measurement of 0.588 seconds. A slow drift in the X-ray source intensity was also observed by Mäkiharju et al. (2013). This nearly linear drift has been corrected by using calibration images $I_{full}(t)$ and $I_{empty}(t)$. Hereby we synchronize the phase of the X-ray source for the calibration $I_{full}(t)$ and $I_{empty}(t)$. This effectively excludes the observed slow drift in intensity. This approach prevents an underestimation of vapor fraction in the beginning of the measurement (when a lower intensity is measured) and an overestimation of vapor fraction at the end of the measurement. After synchronizing and corrections for the intensity of the X-ray source, the vapor fractions per image are computed by Eq. (4.1). Occasionally, single pixels in the far downstream image regions show negative vapor fractions, caused by the near absence of vapor in combination with non-zero intensity variance. This non-physical artifact is resolved by setting pixels with a negative vapor fraction to zero in all images.

To convert dimensions of the vapor clouds in the images to actual physical dimensions,

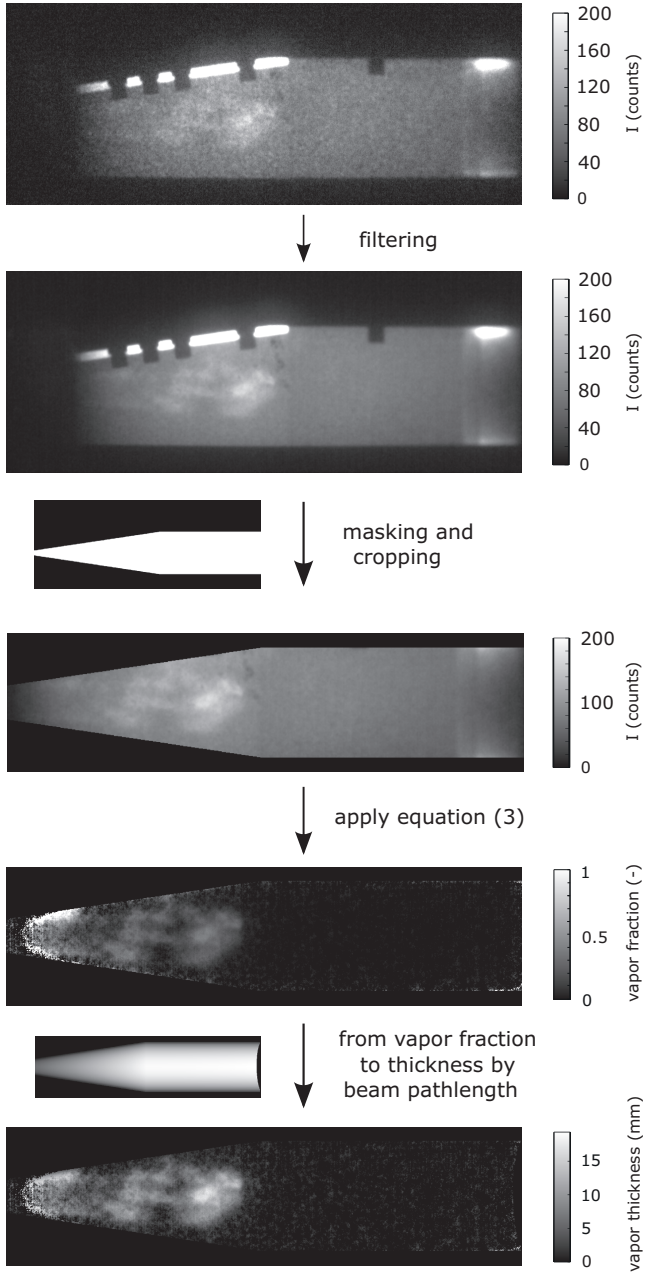


Figure 4.5: Data processing: from raw intensity image data to vapor thickness

we model the X-ray source and venturi projection image and compute for each image pixel the corresponding path length through the venturi interior. The measurement domain consists of a divergent part and a cylindrical part, and what may appear as equal vapor fractions in each of these parts may actually result in different values for the vapor thickness. The exact location of the X-ray source is determined by using a calibration target consisting of a two rows of metal rods, separated by 90 mm, where the top and bottom arrays have different lengths to distinguish between top and bottom. The distance of 557 mm from the X-ray source to the centerline of the venturi is not large with respect to the typical size of the measurement domain (≈ 100 mm), so that it is necessary to take into account the divergence of the X-ray beam. Values for the vapor thickness are computed by the Hadamard product of the vapor fraction image values through Eq. (4.1) and geometrical X-ray beam length through the liquid-vapor mixture. These path lengths are thus corrected for the position of the venturi with respect to the X-ray source.

Since we only have the total vapor thickness data along the ray paths, we cannot reconstruct the exact 3D-shape of the vapor concentration, and thus we are limited to quasi-3D reconstructions. However, based on the assumption of axisymmetry in combination with the observation that vapor structures form clusters in the projected $X - Y$ plane, it is most likely that vapor structures are also clustered in the $X - Z$ plane and form distinct clouds (see also section 4.4). Note that for computing the potential energy, which is the main goal of this study, the exact 3D-reconstruction is not required as this involves volume integration. Asymmetry due to gravity is considered negligible as $Fr = u_{th}/\sqrt{gD_b} \gg 1$, which is also supported by previous observations in the same experimental setup (Jahangir et al., 2019).

4.3.2. VAPOR VOLUME OF DETACHED CAVITIES

A distinction between the attached vapor sheet directly downstream of the venturi throat and the *detached* vapor cavities to the right of the red zigzag line in Fig. 4.6 is required to quantify the initial cavity potential energy. The attached vapor sheet condenses as a result of the passage of the condensation shock wave (Gawandalkar & Poelma, 2022), travelling upstream from the collapse location, and does not contribute to the emitted shock wave energy by the vapor cavities that are first shed and then collapse downstream. Therefore, a space-time diagram (or $X - t$ diagram) is constructed for each measurement to track the contours of the attached vapor sheet. As the attached sheet grows and retracts quasi-periodically, the region of interest is adjusted for each individual cycle to only include shed vapor structures. To illustrate this, Figure 4.14 in the results section

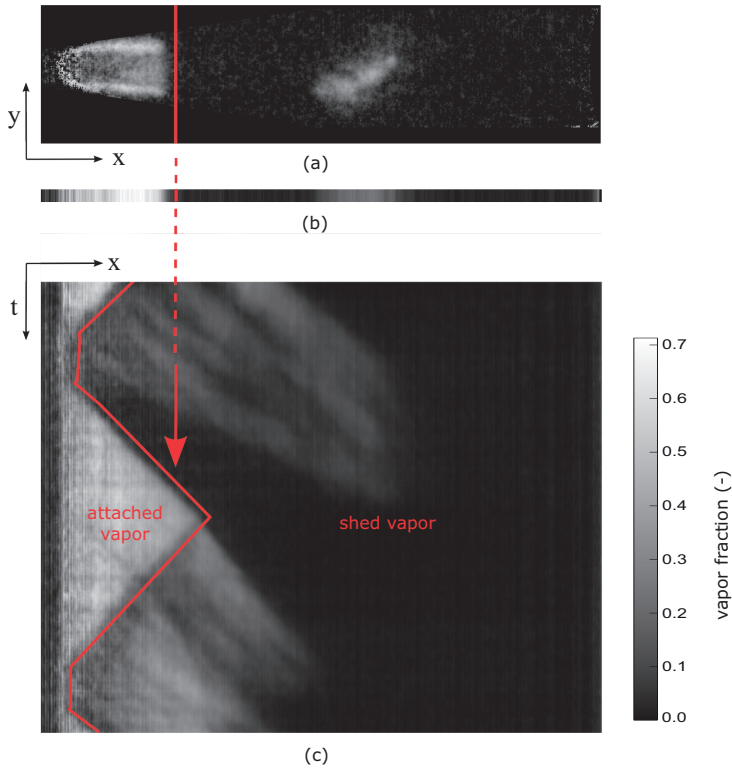


Figure 4.6: Separating the attached and shed vapor structures. Only detached vapor to the right of the red line is included in the instantaneous vapor volume. (a) processed instantaneous image of the vapor fraction, (b) averaged vapor fraction per horizontal pixel, and (c) x - t diagram with vertically stacked averaged vapor fractions from b.

shows the evolution of V_{vap} for a single shedding cycle. The maximum shed vapor volume $V_{vap,0}$, indicated by a blue arrow, is used to calculate the potential energy in the vapor bubble clouds for each cycle. The instantaneous detached vapor volume V_{vap} is computed by summing up all vapor volumes per pixel that are within the region of interest.

4.3.3. PRESSURE DATA

Three piezoelectric pressure transducers have been employed to measure the shock wave energy (using Eq. (4.4), to be discussed in detail later) and the shock wave speed. As the violent vapor collapses produce shock waves, attenuation of the higher frequency components results in an underestimation of the peak pressure. Reconstructing the pressure profiles is challenging when this attenuation is unknown. Also, wave steepening effects

between the collapse center and location of the pressure transducers, limitations of the pressure transducer, and the finite dimensions of the transducers' surface complicate the reconstruction of the actual pressure. However, all measurements are subject to the same geometry and equipment, so that it can be expected that these effects are similar for all measurements. The high-frequency response of piezoelectric pressure transducers needs to be taken into consideration, especially for strong transient shock waves (Persico et al., 2005; Svete & Kutin, 2022; van de Bunt & Bouvy, 2011). Based on the specifications provided by the manufacturer, the transfer function of the PCB102b probes is almost unity up to 300 kHz, which is well beyond our sampling rate of 100 kHz. The inset of Fig. 4.7 shows that the rising slope consists of in total 30 samples (= 0.3 ms). Based on the measured pressure profiles, possible loss due to missing high-frequency components is assumed to be negligible. In previous studies, the pressure profile was characterized by the peak pressure P_{max} , the sound power spectral density (W. K. Blake et al., 1977), or the acoustic impulse $I = \int_{T_s} P dt$ (Ceccio & Brennen, 1991; Kumar & Brennen, 1993; Reisman et al., 1998). Reisman (1997) emphasized that choosing the limits of integration may prove to be non-trivial, as poorly chosen limits may lead to inaccurate pressure impulse estimates. In the current study, the pressure profile is therefore quantified by the integrated squared pressure to directly compute the shock wave energy; see Eq. (4.3) in Section 4.4. Figure 4.7 shows an advantage of using the squared pressure as it significantly reduces the contribution of both tails (around times t_a and t_b , indicated by red dashed lines in Fig. 4.7). The grey shaded area is integrated to compute the shock wave energy.

During the data processing, we noticed that for some measurements the second and third pressure transducer only partially capture the shock wave energy. This occurs at the start of the measurements, which may be an indication that the liquid is not fully degassed, even after degassing for over 45 minutes at low system pressure before starting the measurements. This observation agrees with the findings of Reisman (1997), who reported a profound reduction in the measured acoustic impulse by the injection of air into the sheet cavity, even at very low flow rates. This claim is further supported by the significantly lower observed shock wave speeds for initial measurements compared to later measurements for similar flow conditions (Ca , P_∞), as shock wave speeds depend significantly on the void fraction (Ando et al., 2011; Campbell et al., 1958; Cornel et al., 2023). In these cases, the shock wave energy is partially absorbed by the liquid, so that the potential energy hypothesis cannot be tested. Also, for a limited number of measurements we find that $\int P_2^2 dt > \int P_1^2 dt$, which cannot be fully explained. Although the pres-

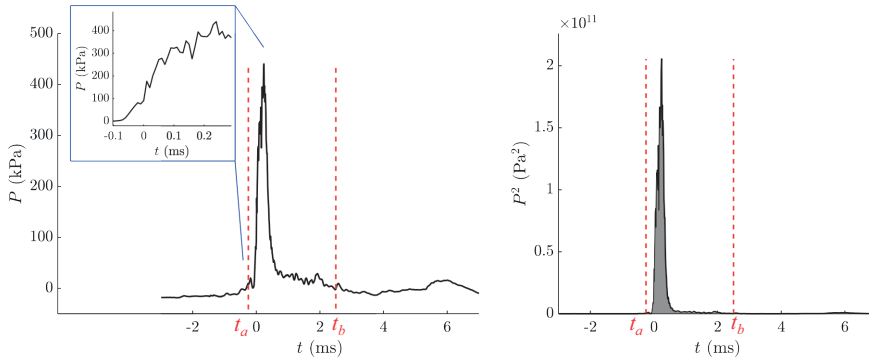


Figure 4.7: (left) A typical example of the original recorded pressure profile for the final collapse stage, where the arrival of the emitted shock wave front at pressure transducer 1 is clearly noticeable by the sudden rise in pressure. (right) The integrated squared pressure between t_a and t_b for computing the shock wave energy. Note that the reduced contributions of the tails avoid the sensitivity of the choice of the limits of integration, which are indicated by the red dashed lines.

sure profiles in transducer 1 and 2 are highly correlated, there is a small difference that significantly contributes to the increase of $\int P_2^2 dt$. Therefore, only measurements that meet the criterion $0.75 < \int P_2^2 dt / \int P_1^2 dt < 1.25$ are included in the analysis to remove any undesired effects due to air content in the working fluid during the measurements. In the end, 41 percent of the measurements are not evaluated. By alternating between parameter sets, we are able to obtain results for all the parameter sets, albeit fewer measurements per set. Redoing the experiments was not feasible due to the limited time available to access the facility, even more so in the view of COVID restrictions.

The shock wave speed U_s is determined directly from pressure transducers 1 and 2, which are located downstream of the collapse location and separated by $D_{1,2} = 350 \pm 1$ mm. For each collapse cycle, the consecutive arrival (or reference) times t_1 and t_2 , respectively, of the shock wave front are determined. The shock wave profile is well-defined (see Fig. 4.7), and the arrival time is defined by the pressure exceeding a threshold value of $0.40 \cdot P_{max}$. Straightforwardly, the shock wave speeds are computed by $U_s = D_{1,2} / (t_2 - t_1)$ for each shedding cycle. Because shock waves are characterized by a very steep rise in pressure, the uncertainty in arrival time is estimated to be $\pm 10 \mu s$, corresponding to 2 samples at a sampling rate of 100 kHz.

4.3.4. SYNCHRONIZING IMAGE AND PRESSURE DATA

Synchronizing images and pressure data per collapse cycle is based on the arrival time of the shock wave front at pressure transducer 1, given by the first sample where the shock pressure exceeds the specified threshold value. Since the pressure and camera recordings start simultaneously and their recording frequencies are known, the images and pressure samples can be synchronized and split by individual cycles, each relative to the reference time. As we are mainly interested in the final stage of the collapse, we isolate 10 ms of data prior to each collapse, corresponding to 250 images (at 25 kHz) or 120 images (at 12 kHz). Note that the collapse does not exactly take place at $t=0$, as the closest pressure transducer 1 is located approximately 150 mm from the average collapse location. This corresponds to circa 0.5 ms for a typical shock wave speed of $U_s = 300$ m/s.

4

4.4. RESULTS

INSTANTANEOUS VAPOR VOLUME OF TYPICAL FINAL STAGE COLLAPSES

The instantaneous projected vapor volume by X-ray densitometry (recorded at 12 kHz) of a typical collapse cycle is presented in Fig. 4.8 for $Ca = 0.415$ and $P_\infty = 41$ kPa. The evolution of the vapor cloud thickness is resolved and synchronized with the pressure recordings. The shed vapor cavities are advected downstream by the flow with an observed velocity of 2.5 ± 0.5 m/s (represented by the magenta dashed lines in Fig. 4.8), which is roughly 18 percent of the flow velocity at the throat. As the local pressure recovers downstream, the driving pressure $P - P_{vap}$ increases and the vapor structure collapses. No shed vapor remains visible in the image at time t_0 , which corresponds to the arrival time of the emitted shock wave front at pressure transducer 1 (see section 4.3.3). The observed shedding frequency is 47 Hz, and 67 percent of the cycle is shown in Fig. 4.8. Instead of showing vapor fractions, we deliberately chose to display the projected thickness of the cavities, as the divergent section between the venturi throat and cylindrical tube would have disturbed the visualization. Because of the axial dependency of the tube diameter, the vapor fraction of bubbles with constant volume would decrease while travelling downstream due to the increasing tube diameter. This distortion effect is avoided when using vapor volumes, so that the displayed changes in the vapor structure are solely caused by actual changes in the vapor volume. Furthermore, the potential cavity energy E_{pot} depends on V_{vap} and P_d , making the chosen display of the vapor volume obvious.

The visualized vapor thickness projections are cavitation clouds consisting of collections

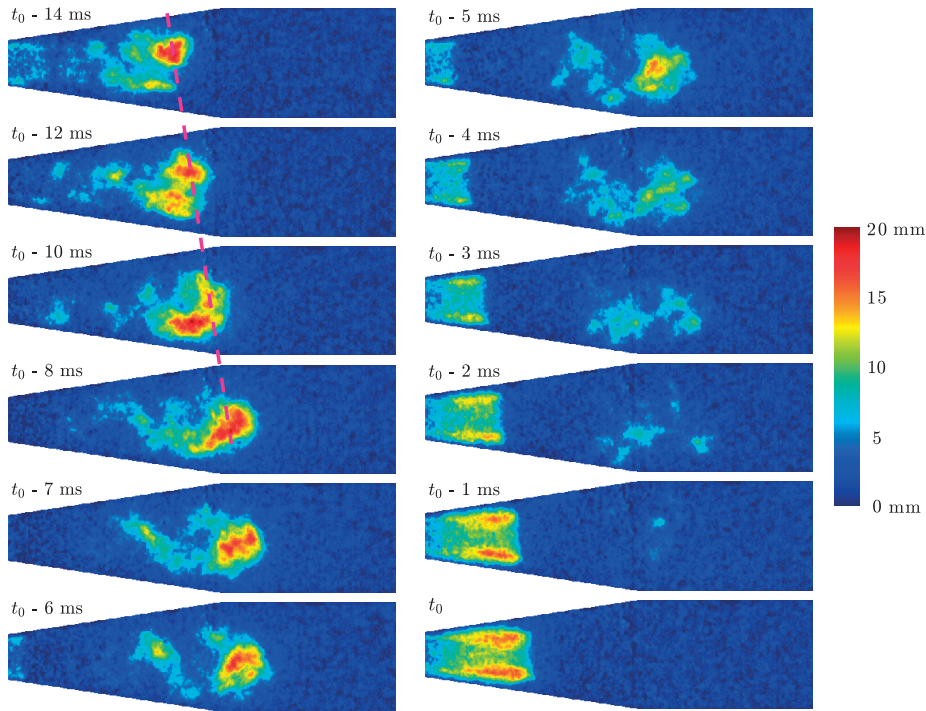


Figure 4.8: Typical evolution of vapor structures in the final stage of a collapse. t_0 represents the time at which the emitted pressure wave is detected by pressure transducer 1. The last remaining vapor visible is at $t_0 - 1$ ms, while other vapor structures already collapsed. The attached vapor sheet, created at the throat from $t_0 - 6$ ms onwards, is excluded from the shed vapor clouds when determining the shed vapor volume. The vapor thickness is purposely expressed in its physical dimension (mm), to avoid distortion in the visualization due to varying tube diameter. A movie of this collapse cycle is available as supplementary material.

of smaller condensable bubbles surrounded by liquid. Since only one camera was employed, we do not have information on the distribution of the vapor clouds in the direction normal to the projected plane. However, the cavitation clouds in the projected plane form clusters, and the mean flow is approximately axisymmetric under the assumption that effects due to gravity are negligible (see section 4.3.1), it is most likely that similar vapor cloud structures are present in the projected direction. Y.-C. Wang and Brennen (1995) studied the characteristic dynamics of cavitation clouds and proposed a cloud interaction parameter $\beta = \alpha_0 (1 - \alpha_0) A_0^2 / R_0^2$, where A_0 and R_0 are the initial radii of the cloud and bubble, respectively. If $\beta > 1$, bubble interactions dominate, and the cloud behaves as a collective structure (Reisman et al., 1998). Otherwise, the natural frequency of the cloud approximates the natural frequency of single isolated bubbles. Although small individual bubbles are not spatially resolved due to limitations of this

measurement method, we estimate the minimum allowed bubble size R_0 for coherent cloud dynamics by rearranging the cloud interaction parameter. Based on image $t - 10$ ms in Fig. 4.8, we estimate $\alpha_0 \approx 0.4$, and $A_0 \approx 15$ mm. For $\beta = 1$, this gives a minimum allowed bubble size R_0 of 7.3 mm. Individual bubbles of such large size (diameters of 14.6 mm) were not observed (see also supplementary material accompanying the paper of (Jahangir et al., 2018)), so that the cloud interaction parameter in the present measurements is $\beta \gg 1$. Our findings are in agreement with Rasthofer et al. (2017) and Du et al. (2016), who found typical values of $\beta \approx 85$ and 115, respectively.

ENERGY PARTITIONING DURING THE FINAL VAPOR COLLAPSE STAGE

The cavity potential energy $E_{pot} = V_{vap}(P - P_{vap})$ is estimated from X-ray images and local pressure recordings. The driving pressure ($P - P_{vap}$) depends on the local pressure in the liquid and the vapor pressure. The reference system pressure P_∞ is measured far downstream of the venturi (see section 4.2). Bernoulli's principle is applied to estimate the local pressure P in the divergent part of the venturi, and hereby neglecting the effect of viscous dissipation. The effect of vapor blockage (smaller effective cross-sectional flow area) may cause vapor bubbles to collapse further downstream, compared to a single-phase approach, due to higher local velocities (and thus lower pressure) around the vapor bubbles. However, due to the highly complex two-phase flow the effect of vapor blockage on the local pressure is not further investigated in this research. The cavity potential energy is computed per horizontal pixel index i as $E_{pot}(i) = (P(i) - P_{vap}) \sum_j V(i, j)$, where $V(i, j)$ is the projected volume per pixel (i, j) and j is the pixel index in the vertical direction. Next, the total potential energy (per image) is summed over all pixels downstream of the attached cavity (i.e., to the right of the red line in Fig. 4.6). Since the shock wave energy originates from the shed vapor cavities, it is essential to exclude the attached vapor sheet. For each collapse cycle, the maximum amount of cavity potential energy is determined.

The shock wave energy for a collapsing isolated vapor bubble in an infinite reservoir is given by (Schenke et al., 2019):

$$E_s = \frac{A(r)}{\rho_{liq} U_s} \int_{T_s} P_s^2(t, r) dt, \quad (4.2)$$

where A is the surface at some distance r from the source, U_s the shock wave speed, ρ_{liq} the liquid density, P_s the pressure magnitude of the shock wave, and T_s the shock wave duration (typically in the order of milliseconds). For idealized spherical bubbles with $A = 4\pi r^2$, the original equation by Cole (1948) is retrieved. Since the experiments

are performed in a tube, and the distance between the collapse location and the nearest pressure transducer well exceeds the diameter of the tube, the surface area in the present case is better approximated by $A = 2 \cdot \pi \left(\frac{D_{tube}}{2} \right)^2$ (see also Fig. 4.2, right), where the factor 2 is included to capture both the shock waves travelling upstream and downstream. The integral term in Eq. (4.2) is approximated by the discrete summation over the recorded pressure samples in between the threshold pressure levels:

$$\int_{T_s} P_s^2(t, r) dt \approx \frac{1}{f_s} \sum_i P_{sw,i}^2 \quad (4.3)$$

where i represents the pressure sample index, and f_s the sampling frequency of the pressure signal, which is 100 kHz for all performed experiments. Combining equations (4.2), (4.3), and the adjusted surface A yields :

$$E_s \approx \frac{\pi D_{tube}^2}{2 \rho_{liq} U_{liq}} \frac{1}{f_s} \sum_i P_{sw,i}^2. \quad (4.4)$$

Figure 4.9 shows the amount of initial cavity potential energy E_{pot} that is converted into shock wave energy E_s . Note that $E_{pot} \geq E_s$ must hold for the shock wave originating from the vapor collapse. Since there is a causal relation between E_{pot} and E_s , cycles with $E_{pot} < E_s$ are considered as measurement errors and non-physical, as this means that more energy is measured than initially present. For each parameter set (Ca , P_∞) between 52 and 148 cycles are observed. Collapse cycles with similar kinetic energy are denoted by squares. These collapses contain more energy compared to collapses with a higher Ca number. The relatively large variance in data points is mainly caused by the inherent cycle-to-cycle variations, which also was reported by Reisman et al. (1998), and also shown in Fig. 4.14. Furthermore, in agreement with findings of Reisman et al. (1998) we observe that the overall pattern is quite repeatable. The absolute variance increases with decreasing cavitation number, for constant kinetic energy.

Within the experimental range, on average between 24 and 56 percent of the cavity potential energy E_{pot} is converted into shock wave energy. The lowest and highest conversion factors were found for $(Ca, P_\infty) = (0.61, 36 \text{ kPa})$ and $(0.42, 41.3 \text{ kPa})$, respectively; see Fig. 4.10. For constant kinetic energy with $u_{th} = 13.7 \pm 0.1 \text{ m/s}$ (left panel), relatively more potential energy is transferred into shock wave energy for decreasing Ca numbers. Interestingly, more potential energy is converted into shock wave energy for increasing local pressure at constant cavitation number. The higher driving pressure could result in more severe cavity collapses.

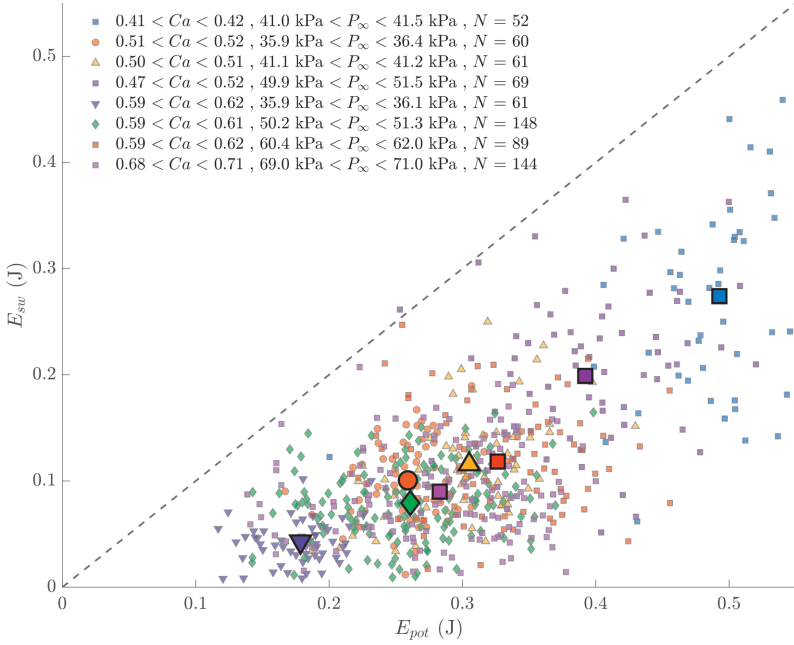


Figure 4.9: E_{pot} versus E_s for different Ca numbers and P_∞ for in total 684 vapor collapses. E_{pot} is measured by the X-ray densitometry method, while E_s is computed from the pressure transducers. Especially for higher cavitation numbers $Ca > 0.6$ we notice that a smaller part of the observed potential energy is converted into shock wave energy.

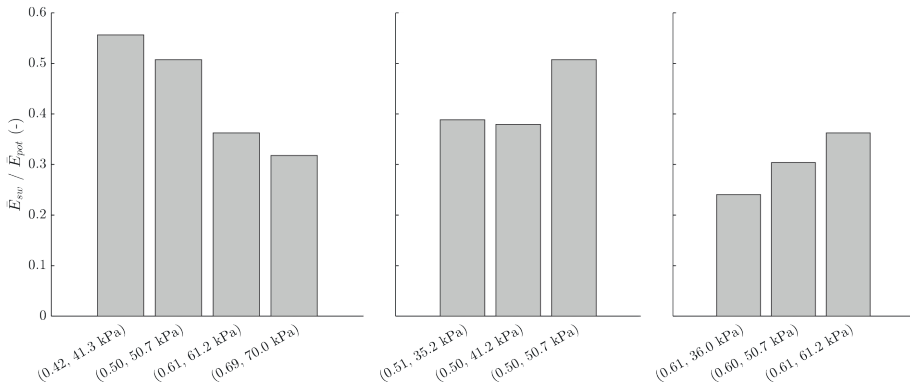


Figure 4.10: Energy partitioning from E_{pot} to E_s for constant u_{th} (left), constant $Ca = 0.5$ (center) and constant $Ca = 0.6$ (right). The (Ca, P_∞) values on the horizontal axis represent the measurement sets.

The rebound energy E_{reb} is estimated by $V_{vap,reb}(P - P_{vap})$, where $V_{vap,reb}$ is the amount of rebounded vapor volume that appears after the final stage of the collapse. However, no significant amount of $V_{vap,reb}$ was observed in any of the performed measurements, not even for the lowest liquid pressure ($P_\infty \approx 40$ kPa); see Fig. 4.13. Interestingly, the contribution of rebound energy increases for lower pressures (Tinguely et al., 2012), and thereby decreases the energy available to convert to shock wave energy. Conservatively estimated for this measurement, the X-ray densitometry is able to resolve vapor bubble clusters with projected thickness of 3.0 mm, leading to an upper estimate for E_{reb} of 0.5 mJ, which is orders of magnitude smaller than the potential energy E_{pot} observed in the experiments. For this estimate, $V_{vap,reb}$ is approximated by a sphere filled with vapor, i.e. $V_{vap,reb} = (\pi/6)D_{b,reb}^3$ with $D_{b,reb} = 3.0$ mm.

ENERGY TRANSFER OF E_{pot} TO E_s FOR CONSTANT u_{th}

The vapor potential energy E_{pot} and shock wave energy E_s are closely examined by the effect of four (Ca , P_∞) configurations on the experimentally measured quantities V_{vap} , $\int P_1^2 dt$, U_s , $P - P_{vap}$ for constant added kinetic energy per volume $\rho_l u_{th}^2/2$ with $u_{th} \approx 13.7$ m/s \pm 0.1 m/s (squares in Fig. 4.9). The available fluid kinetic energy for the formation of the vapor bubble clouds is held constant to isolate the effect of local pressure. From the equation of the potential energy $E_{pot} = V_{vap}(P - P_{vap})$ it follows that lowering the driving pressure $P - P_{vap}$ reduces the amount of potential energy, while E_{pot} increases proportionally with V_{vap} . The potential energy E_{pot} increases for lower cavitation numbers while keeping u_{th} constant; see Fig. 4.9 (left). This is not immediately obvious, as lower driving pressures proportionally reduce the cavity potential cavity energy. The amount of vapor increases by a factor of approximately 3 from 4.7 to 13.6 cm³, while the pressure is nearly halved from 70 to 40 kPa; see Fig. 4.11. Figure 4.9 (right) shows the effect of the pressure on the emitted shock wave energy for constant kinetic energy. The amount of emitted shock wave energy increases non-linearly with decreasing pressures. The non-linearity also motivates the decreasing trend in the conversion ratio E_s/E_{pot} for increasing Ca as shown in Fig. 4.10 (left), since relatively less potential energy is converted into shock wave energy.

Shock wave energy, among other energy terms, is emitted by the collision of accelerating flows at or close to the vapor cloud centers. Therefore, it is expected that V_{vap} and $\int P_s^2 dt$ are positively correlated which is confirmed in Fig. 4.12. A linear fit through the four data points that summarize the results at the four general flow conditions almost approaches the origin, which is expected since no pressure waves are observed in the absence of vapor cavities. An alternative fit that is forced to intersect the origin passes

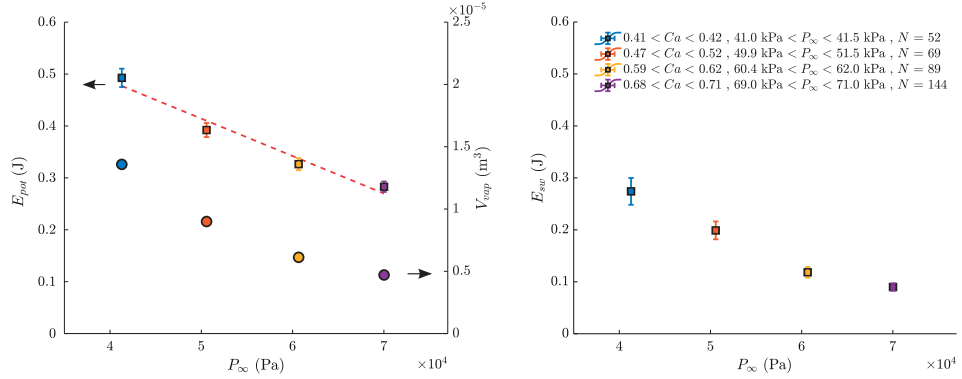


Figure 4.11: Relation between between the system pressure P_{∞} and E_{pot} (left), and P_{∞} and E_s (right) for constant kinetic energy per volume. The liquid velocity at the throat is kept constant around 13.7 m/s \pm 0.1 m/s. For decreasing local pressures (nearly halved), the increase of vapor volume (by a factor 3) results in an increase in potential energy.

4

through the three lower volume data points. For larger Ca numbers, the vapor structures have less time to grow, which result in smaller volumes. Figure 4.12 supports the findings of Gavaises et al. (2015), who proposed cavitation structures for lower Ca numbers are present for a longer time to form agglomerations. Chizelle et al. (1995) studied the relationship between the dimensionless impulse and the maximum vapor volume $V_{vap,max}$, where they obtained the actual sizes of individual cavitation bubbles from imaging. They showed that the dimensionless impulse and maximum vapor volume are positively correlated. Their findings are in agreement with our experimental results.

4.5. DISCUSSION

There are several effects that may contribute to the difference between E_{pot} and $E_s + E_{reb} + U$, including (1) the non-geometrical focusing of the liquid in the center of the cavitation cloud, (2) the absence of rebounds, (3) the exclusion of the internal energy, (4) the exclusion of the vapor blockage in estimating the local pressure, (5) the attenuation of the shock wave between the collapse location and pressure transducer 1, (6) the loss of the shock wave energy to the surroundings, and (7) the observation that some vapor clusters may collapse before the final collapse. For (6) and (7), the emitted shock wave energy is not included in the estimation of E_s .

1. Figure 4.8 shows that the coherent and collective vapor bubble clouds are asymmetric. This corresponds with the findings of Jahangir et al. (2019). Although not readily observed, micro-jets may form upon collapses (Obreschkow et al., 2011).

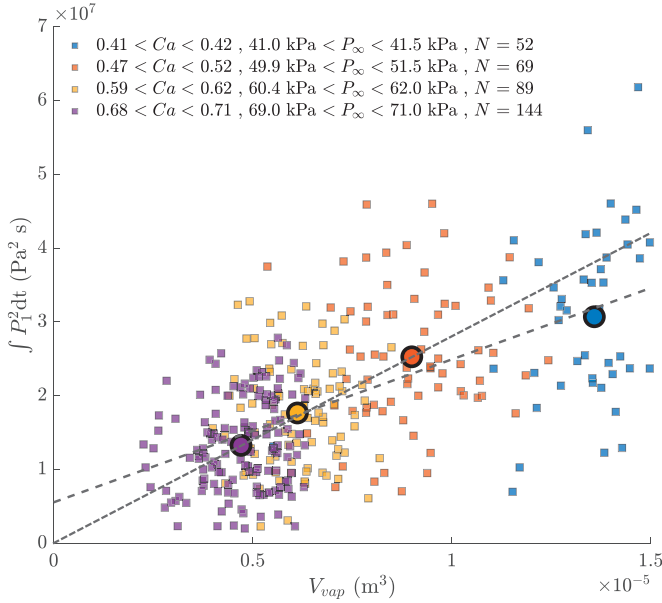


Figure 4.12: The relation between V_{vap} and the integrated squared pressure $\int P_1^2 dt$ for constant kinetic energy per volume. The four coloured markers represent the average value of the individual collapse cycles (smaller markers) for 4 flow conditions (Ca, P_∞) .

Therefore, some residual kinetic energy may result in the complex flow dynamics, such as impinging liquid jets, as suggested by Schenke et al. (2019).

2. Tinguely et al. (2012) observed experimentally the single cavitation bubble dynamics in micro-gravity conditions, and showed that the surrounding pressure has an effect on the first rebound bubble. They concluded that for three distinct water pressures (10, 30, and 80 kPa) the diameter of the first rebound bubble increases for lower pressures. In case of $P_\infty = 30$ kPa and 80 kPa, the normalized rebound radius varies between $0.2 \leq R/R_{max} \leq 0.48$ and $0.2 \leq R/R_{max} \leq 0.24$, respectively (see Fig. 2 in (Tinguely et al., 2012)). Rebound cycles are subsequent cloud collapses that also produce radiated pulses (Reisman et al., 1998). In our experiments, the cavitation clouds consist of small vapor bubbles, in contrast to a single cavitation bubble. However, compared to our experiments at $P_\infty = 41.5$ kPa, the previously mentioned correlation would correspond to the rebounded vapor cloud with $R/R_{max} \geq 0.2 \approx 3$ mm diameter in case of a 15-mm diameter sized initial vapor cloud. This was not observed in the present experimental data; see Fig. 4.13. By investigating our experimental data on the rebound of vapor after the collapse

(see Figure 4.13, last images), it is concluded that $E_{kin,rebound}$ can be neglected for our experiments.

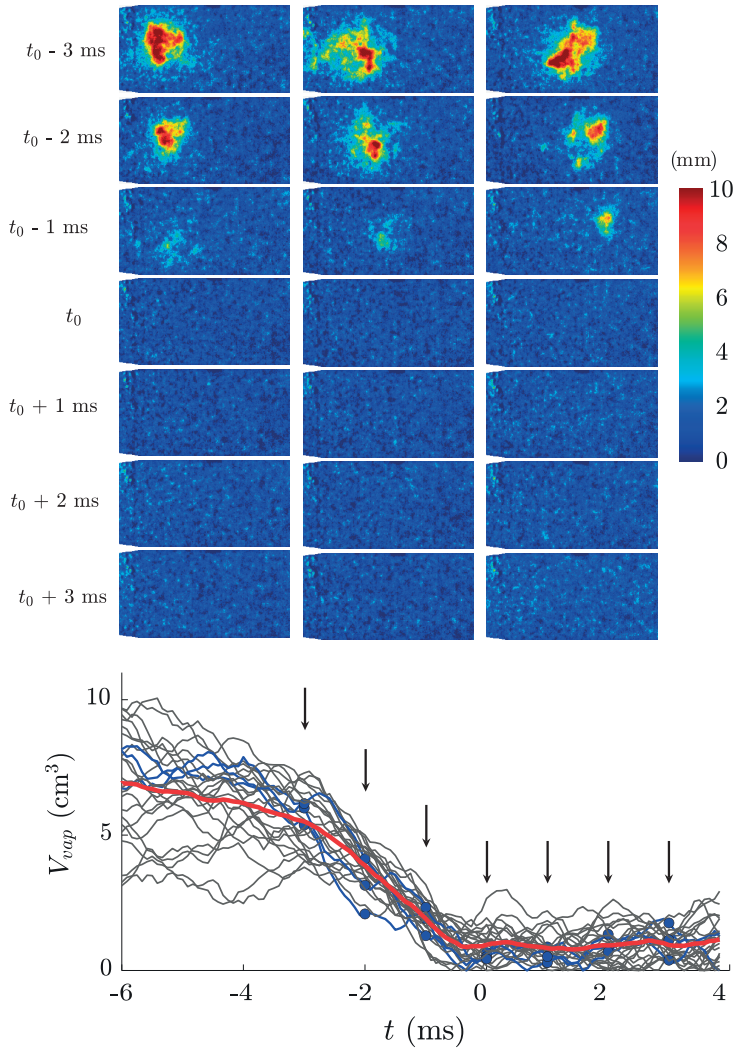


Figure 4.13: The final collapse and rebound stage of three cycles for $t = -3$ to 3 ms (top) and the evolution of shed vapor volume for 25 collapse cycles (bottom). Each of these cycles originate from individual measurements ($Ca = 0.415$, $P_\infty = 41$ kPa) of 0.63 seconds. The color bar represents the projected thickness of the cavitation cloud in mm. The blue lines indicate the three collapse events above. Movies of these collapse cycles are included as supplementary material. No significant cavitation rebound is observed after the final collapse.

3. The internal energy U of the condensable bubble cloud is not further taken into account as internal energy can be neglected (Tinguely et al., 2012). Non-condensable

gas dissolved in the liquid may diffuse into the vapor bubbles (Prosperetti, 2017), but the amount of non-condensable gas content in the liquid is considered negligible; see also Section 4.3.3).

4. We applied Bernoulli's principle to estimate the local pressure and ignore that the flow actually is a two-phase liquid. Taking vapor blockage into account, this would result in a lower local pressure and subsequently lower driving pressures. These lower local pressures may result in smaller cavity potential energy; see Fig. 4.11. This effect is significant close to the throat due to the relative large vapor fraction in the attached vapor sheet. However, for the shed vapor downstream this effect diminishes. Based on Fig. 4.8, we estimate the increase in local flow velocity by the reduced cross-sectional flow area as A_{vap}/A_{tube} to be approximately 15 percent. This would imply an increase from about 1.5 to 1.7 m/s at the collapse location. Note that the corresponding change in local pressure is less than 1 % for $P_{\infty} = 41$ kPa.
5. The shock waves propagate through the liquid towards the pressure transducers. Possibly energy is dissipated by the remaining bubbles in the liquid, causing attenuation of the shock wave. Based on the pressure measurements at distance of approximately $3D_{tube}$ for transducer 1 and $\sim 10D_{tube}$ for transducer 2, we conclude that the energy dissipation through the fluid is negligible for this relative short distance to transducer 1. Furthermore, the effect of non-condensable gas can be neglected as the system was degassed; see also section 4.2.
6. Audible noise is clearly noted while running the measurements under strongly cavitating conditions, and hearing protection is required under these conditions. These acoustic waves travelling to the surroundings may not have been recorded by the pressure transducers. As a conservative estimate of the acoustic energy loss, a sound pressure level of 100 dB at one meter distance from the cavitation for a duration of 1 ms corresponds to $\mathcal{O}(10^{-4})$ J $\ll E_s$ and can therefore be neglected.
7. Cycle-to-cycle variation is a general feature of sheet-to-cloud shedding (Reisman et al., 1998), and there is no perfect repeatability in the shedding process (Büdich et al., 2018). This phenomena has also been reported in literature, for example by Ganesh et al. (2016) and Reisman et al. (1998). Cycle-to-cycle variation causes differences between collapse cycles, even under nearly identical measurement conditions (even within 0.63 seconds). Due to this, many different shed clouds may form. For instance, the observation that the vapor cluster may collapse before

the final collapse contributes to the underestimation of the produced shock wave energy during the final collapse stage, as only passing shock waves between $t_a < t_0 < t_b$ are integrated. Most of these collapses produce weaker shock waves; see Fig. 4.14. However, this cannot explain the energy difference between E_{pot} and E_s for all measurements. Furthermore, multiple shed vapor bubble clusters are formed during the shedding and collapse stages; see Fig. 4.8. It is unlikely that these clusters collectively emit shock waves, and it is possible that the observed pressure profile is a non-linear superposition of shock waves generated from distinct vapor bubble clusters.

4

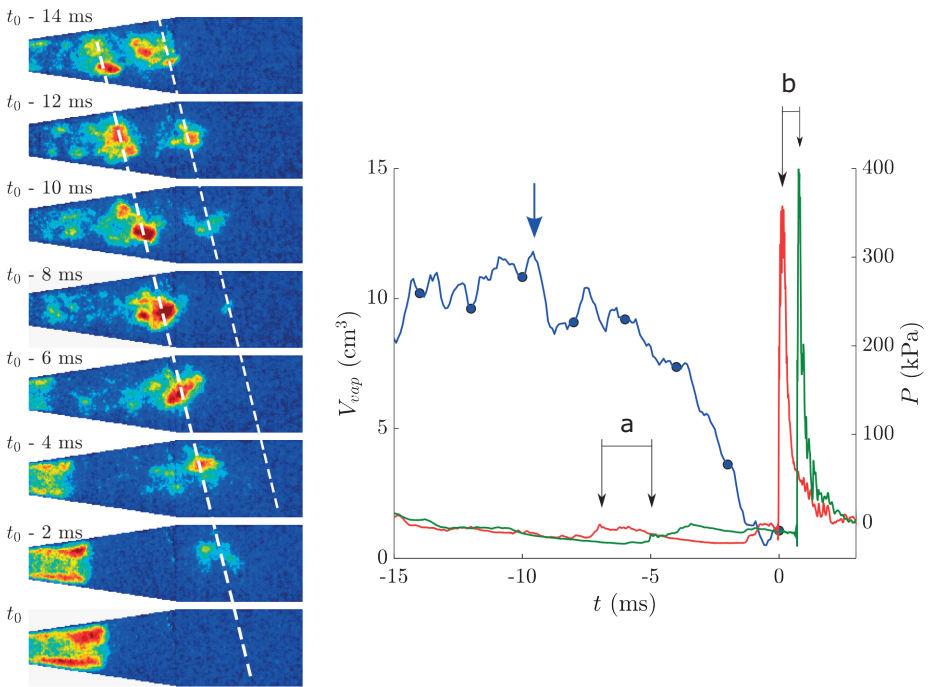


Figure 4.14: Left: Evolution of a vapor cloud during the final collapse stage with multiple collapses. Right: corresponding V_{vap} (blue), and pressure signals from transducer 1 (P_1 , red) and 2 (P_2 , green). The small pressure peak in P_1 and P_2 at $t \approx -7$ ms originates from the early vapor cloud collapse. Because of the lower pressure amplitude, the shock wave speed of the final collapse (indicated by b) exceeds the shock wave speed of the earlier collapse (indicated by a). The blue arrow (at $t \approx -10$ ms) represents the maximum instantaneous shed vapor volume. Both vapor clouds are travelling with similar velocities, as shown by the two parallel white dashed lines. Also, the shock wave arrives at transducer 1 first, which validates that the shock wave originates from the vapor cloud collapse location, and thus not being a reflected wave.

Interestingly, Fig. 4.14 shows no significant pressure fluctuations prior to the final collapse stage, while an earlier collapse occurs at $t \approx t_0 - 8$ ms. The shock waves originate

from the cloud collapses, as the shock wave fronts are first detected by pressure transducer 1 subsequently followed by transducers 2 and 3, and no reflected shock waves from other collapse cycles are observed. However, during some experiments we also observe ‘multiple’ collapses, in which two or more significant pressure peaks within one shedding cycle are detected. This phenomena has significant effects on the magnitude of final pressure impulse, which is significantly reduced compared to other observed final pressure peaks in comparable conditions. Studying the arrangement of the local vapor structures might resolve this issue.

Since we can follow the development and collapse of the total vapor volume in time, we can apply an alternative method to relate the collapsing cavitation cloud to the emitted shock waves by computing the volumetric acceleration of the vapor volume: $d^2 V_{vap} / dt^2 = P4\pi R / \rho$ (W. Blake, 1986; Chizelle et al., 1995). However, corresponding to the findings of G. Chen et al. (2015), we also noticed that the volumetric acceleration of the vapor phase is relatively smooth (at 25 kHz, with a temporal filter of 11 frames), and not able to accurately describe the strong shock waves with pressure magnitudes in the order $\mathcal{O}(10^5)$ Pa.

4.6. CONCLUSION

The energy partitioning during the final stage of a vapor cloud is investigated by applying high-speed X-ray densitometry with simultaneous pressure measurements to a cavitating flow through a venturi. The projected vapor fractions and volumes of the cavity structures are quantified for several (Ca, P_∞) combinations with both high spatial and temporal resolution. Contrary to shadowgraphy, X-ray densitometry allows accurate quantification of the cavitation volume over time and the cavity potential energy during the collapse stage. We find that within our experimental range on average between 24 and 56 percent of the initial cavity potential energy E_{pot} is converted into shock wave energy E_s in the event of cloud cavitation. Due to the cycle-to-cycle variance, which causes large differences in cloud arrangements during the collapse, there is also a significant variation in the conversion factor between E_{pot} and E_s for each individual cycle. For a given kinetic energy added to the flow, i.e. u_{th} is constant, we find that both the energy conversion and the amount of E_{pot} and E_s increase for decreasing cavitation number. By keeping the cavitation number constant, it seems that more energy is converted into shock wave energy for increasing ambient pressures. The observed discrepancy between E_{pot} and E_s cannot be explained by the energy conversion to rebound energy E_{reb} (see section 4.4), internal energy ΔU (see Tinguely et al. (2012)), or other losses, such as

acoustic radiation to the surroundings. We conjecture that two complex mechanisms are accountable for this discrepancy. First, we observe that collapses prior to the final collapse only occur sporadically. This means that part of the initial potential cavity energy was already transferred into shock wave energy prior to the final collapse. Secondly, we confirm experimentally that the (projected) cloud cavitation structures have asymmetrical arrangements, most notably in the final stage of the collapse. Residual kinetic energy may remain in the flow (Schenke et al., 2019), contributing to complex flow behavior, such as the occurrence of liquid jets during the collapse. However, we did not observe this with the current X-ray densitometry setup. Recently, Tinguely et al. (2022) also mentioned the formation of micro-jets due to asymmetric collapse during the collapse of a cavitation bubble, further affirming that potential energy is converted into complex flows. In future research, the arrangement of local clusters and linking their volumetric changes to the fluctuations in the recorded pressure profile might provide further information on the energy transfer prior to the final collapse.

BIBLIOGRAPHY

- Adrian, R., & Westerweel, J. (2011). *Particle image velocimetry*. Cambridge University Press.
- Aliseda, A., & Heindel, T. J. (2021). X-ray flow visualization in multiphase flows. *Annu. Rev. Fluid Mech.*, 53(1), 543–567.
- Ando, K., Sanada, T., Inaba, K., Damazo, J. S., Shepherd, J. E., Colonius, T., & Brennen, C. E. (2011). Shock propagation through a bubbly liquid in a deformable tube. *J. Fluid Mech.*, 671, 339–363.
- Bauer, D., Barthel, F., & Hampel, U. (2018). High-speed x-ray CT imaging of a strongly cavitating nozzle flow. *J. Phys. Commun.*, 2(7), 075009.
- Blake, W. K., Wolpert, M. J., & Geib, F. E. (1977). Cavitation noise and inception as influenced by boundary-layer development on a hydrofoil. *J. Fluid Mech.*, 80(4), 617–640.
- Blake, W. (1986). *Mechanics of flow-induced sound and vibration*. Academic Press.
- Bourne, N. (2002). On the collapse of cavities. *Shock Waves*, 11(6), 447–455.
- Brennen, C. E. (1995). *Cavitation and Bubble Dynamics*. Oxford University Press. <http://caltechbook.library.caltech.edu/1/04/content.htm>
- Brujan, E. A., Ikeda, T., & Matsumoto, Y. (2012). Shock wave emission from a cloud of bubbles. *Soft Matter*, 8, 5777–5783.
- Büdich, B., Schmidt, S. J., & Adams, N. A. (2018). Numerical simulation and analysis of condensation shocks in cavitating flow. *J. Fluid Mech.*, 838, 759–813.
- Campbell, I. J., Pitcher, A. S., & Temple, G. F. J. (1958). Shock waves in a liquid containing gas bubbles. *Proc R Soc Lon Ser-A*, 243(1235), 534–545.
- Ceccio, S. L., & Brennen, C. E. (1991). Observations of the dynamics and acoustics of travelling bubble cavitation. *J. Fluid Mech.*, 233, 633–660.
- Chen, G. H., Wang, G. Y., Hu, C. L., Huang, B., & Zhang, M. D. (2015). Observations and measurements on unsteady cavitating flows using a simultaneous sampling approach. *Exp. Fluids*, 56(2), 32.
- Chen, G., Wang, G., Hu, C., Huang, B., Gao, Y., & Zhang, M. (2015). Combined experimental and computational investigation of cavitation evolution and excited pressure fluctuation in a convergent–divergent channel. *Int. J. Multiphase Flow*, 72, 133–140.
- Chizelle, Y. K. D., Ceccio, S. L., & Brennen, C. E. (1995). Observations and scaling of travelling bubble cavitation. *J. Fluid Mech.*, 293, 99–126.
- Cole, R. H. (1948). *Underwater explosions*. Princeton University Press.

- Cornel, W. A., Westerweel, J., & Poelma, C. (2023). Non-intrusive, imaging-based method for shock wave characterization in bubbly gas–liquid fluids. *Exp. Fluids*, 64(2), 35.
- Coutier-Delgosha, O., Stutz, B., Vabre, A., & Legoupil, S. (2007). Analysis of cavitating flow structure by experimental and numerical investigations. *J. Fluid Mech.*, 578, 171–222.
- Dash, A., Jahangir, S., & Poelma, C. (2018). Direct comparison of shadowgraphy and x-ray imaging for void fraction determination. *Meas. Sci. Technol.*, 29(12), 125303.
- Du, T., Wang, Y., Liao, L., & Huang, C. (2016). A numerical model for the evolution of internal structure of cavitation cloud. *Phys. Fluids*, 28(7), 077103.
- Furness, R. A., & Hutton, S. P. (1975). Experimental and Theoretical Studies of Two-Dimensional Fixed-Type Cavities. *J. Fluids Eng.*, 97(4), 515–521.
- Ganesh, H., Mäkiharju, S. A., & Ceccio, S. L. (2016). Bubbly shock propagation as a mechanism for sheet-to-cloud transition of partial cavities. *J. Fluid Mech.*, 802, 37–78.
- Gavaises, M., Villa, F., Koukouvini, P., Marengo, M., & Franc, J.-P. (2015). Visualisation and les simulation of cavitation cloud formation and collapse in an axisymmetric geometry. *Int. J. Multiphase Flow*, 68, 14–26.
- Gawandalkar, U., & Poelma, C. (2022). The structure of near-wall re-entrant flow and its influence on cloud cavitation instability. *Exp. Fluids*, 63(5), 77.
- Grigull, U., & Schmidt, E. (1989). *Properties of water and steam in SI-units 4 enlarged ed* [INIS Reference Number: 20040503]. Springer.
- Heidari-Koochi, M., Karathanassis, I. K., & Gavaises, M. (2021). Chapter 7 - X-ray measurement techniques used for wall-bounded cavitating flows. In P. Koukouvini & M. Gavaises (Eds.), *Cavitation and bubble dynamics* (pp. 211–248). Academic Press.
- Heindel, T. J. (2011). A Review of X-Ray Flow Visualization With Applications to Multiphase Flows [074001]. *J. Fluids Eng.*, 133(7).
- Huang, B., Young, Y. L., Wang, G., & Shyy, W. (2013). Combined experimental and computational investigation of unsteady structure of sheet/cloud cavitation [071301]. *J. Fluids Eng.*, 135(7).
- Hutli, E., Nedeljkovic, M., & Bonyár, A. (2019). Dynamic behaviour of cavitation clouds: Visualization and statistical analysis. *J. Braz. Soc. Mech. Sci. Eng.*, 41(7), 281.
- Jahangir, S., Hogendoorn, W., & Poelma, C. (2018). Dynamics of partial cavitation in an axisymmetric converging-diverging nozzle. *Int. J. Multiphase Flow*, 106, 34–45.
- Jahangir, S., Wagner, E. C., Mudde, R. F., & Poelma, C. (2019). Void fraction measurements in partial cavitation regimes by X-ray computed tomography. *Int. J. Multiphase Flow*, 120, 103085.
- Jung, J., Lee, S.-J., & Han, J. (2009). Study on correlation between cavitation and pressure fluctuation signal using high-speed camera system. *7th International Symposium on Cavitation*.

- Karathanassis, I. K., Heidari-Koochi, M., Zhang, Q., Hwang, J., Koukouvinis, P., Wang, J., & Gavaises, M. (2021). X-ray phase contrast and absorption imaging for the quantification of transient cavitation in high-speed nozzle flows. *Phys. Fluids*, 33(3), 032102.
- Khelifa, I., Vabre, A., Hocevar, M., Fezzaa, K., Fuzier, S., Roussette, O., & Coutier-Delgosha, O. (2017). Fast X-ray imaging of cavitating flows. *Exp. Fluids*, 58(11), 157. Retrieved January 20, 2023, from <https://doi.org/10.1007/s00348-017-2426-7>
- Knapp, R. T. (2022). Recent Investigations of the Mechanics of Cavitation and Cavitation Damage. *Transactions of the American Society of Mechanical Engineers*, 77(7), 1045–1054.
- Kubota, A., Kato, H., Yamaguchi, H., & Maeda, M. (1989). Unsteady Structure Measurement of Cloud Cavitation on a Foil Section Using Conditional Sampling Technique. *J. Fluids Eng.*, 111(2), 204–210.
- Kumar, S., & Brennen, C. (1993). A study of pressure pulses generated by travelling bubble cavitation. *J. Fluid Mech.*, 255, 541–564.
- Leroux, J.-B., Coutier-Delgosha, O., & Astolfi, J. A. (2005). A joint experimental and numerical study of mechanisms associated to instability of partial cavitation on two-dimensional hydrofoil. *Phys. Fluids*, 17(5), 052101.
- Mäkiharju, S. A., Gabillet, C., Paik, B.-G., Chang, N. A., Perlin, M., & Ceccio, S. L. (2013). Time-resolved two-dimensional X-ray densitometry of a two-phase flow downstream of a ventilated cavity. *Exp. Fluids*, 54(7), 1561.
- Mäkiharju, S. A., Ganesh, H., & Ceccio, S. L. (2017). The dynamics of partial cavity formation, shedding and the influence of dissolved and injected non-condensable gas. *J. Fluid Mech.*, 829, 420–458.
- Maurice, G., Machicoane, N., Barre, S., & Djeridi, H. (2021). Coupled x-ray high-speed imaging and pressure measurements in a cavitating backward facing step flow. *Phys. Rev. Fluids*, 6, 044311.
- Melissaris, T., Bulten, N., & van Terwisga, T. J. C. (2019). On the applicability of cavitation erosion risk models with a urans solver [101104]. *J. Fluids Eng.*, 141(10).
- Obreschkow, D., Tinguely, M., Dorsaz, N., Kobel, P., de Bosset, A., & Farhat, M. (2011). Universal scaling law for jets of collapsing bubbles. *Phys. Rev. Lett.*, 107, 204501.
- Persico, G., Gaetani, P., & Guardone, A. (2005). Dynamic calibration of fast-response probes in low-pressure shock tubes. *Meas. Sci. Technol.*, 16(9), 1751–1759.
- Petkovšek, M., Hocevar, M., & Dular, M. (2020). Visualization and measurements of shock waves in cavitating flow. *Exp. Therm. Fluid. Sci.*, 119, 110215.
- Pike, R. W., Wilkins Jr., B., & Ward, H. C. (1965). Measurement of the void fraction in two-phase flow by x-ray attenuation. *AIChEJ.*, 11(5), 794–800.
- Prosperetti, A. (2017). Vapor bubbles. *Annu. Rev. Fluid Mech.*, 49(1), 221–248.
- Rasthofer, U., Wermelinger, F., Hadjidoukas, P., & Koumoutsakos, P. (2017). Large Scale Simulation of Cloud Cavitation Collapse. *Procedia Comput. Sci.*, 108, 1763–1772.

- Reisman, G. E., Wang, Y.-C., & Brennen, C. E. (1998). Observations of shock waves in cloud cavitation. *J. Fluid Mech.*, 355, 255–283.
- Reisman, G. E. (1997). *Dynamics, acoustics and control of cloud cavitation on hydrofoils* (Doctoral dissertation). California Institute of Technology.
- Sarkar, P., Ghigliotti, G., Franc, J.-P., & Fivel, M. (2021). Mechanism of material deformation during cavitation bubble collapse. *J. Fluids Struct.*, 105, 103327.
- Schenke, S., Melissaris, T., & van Terwisga, T. (2019). On the relevance of kinematics for cavitation implosion loads. *Phys. Fluids*, 31(5), 052102.
- Schnerr, G. H., Sezal, I. H., & Schmidt, S. J. (2008). Numerical investigation of three-dimensional cloud cavitation with special emphasis on collapse induced shock dynamics. *Phys. Fluids*, 20(4), 040703.
- Stutz, B., & Legoupil, S. (2003). X-ray measurements within unsteady cavitation. *Exp. Fluids*, 35(2), 130–138.
- Stutz, B., & Reboud, J. L. (1997). Experiments on unsteady cavitation. *Exp. Fluids*, 22(3), 191–198.
- Supponen, O., Obreschkow, D., Kobel, P., Tinguely, M., Dorsaz, N., & Farhat, M. (2017). Shock waves from nonspherical cavitation bubbles. *Phys. Rev. Fluids*, 2, 093601.
- Svete, A., & Kutin, J. (2022). Identifying the high-frequency response of a piezoelectric pressure measurement system using a shock tube primary method. *Mech. Syst. Signal Process*, 162.
- Tinguely, M., Obreschkow, D., Kobel, P., Dorsaz, N., de Bosset, A., & Farhat, M. (2012). Energy partition at the collapse of spherical cavitation bubbles. *Phys. Rev. E*, 86(4), 046315.
- Tinguely, M., Ohtani, K., Farhat, M., & Sato, T. (2022). Observation of the formation of multiple shock waves at the collapse of cavitation bubbles for improvement of energy convergence. *Energies*, 15(7).
- van de Bunt, E., & Bouvy, A. (2011). Dynamic calibration of a pressure transducer. *Advanced Model Measurement Technology Conference, Newcastle*.
- Vogel, A., & Lauterborn, W. (1988). Acoustic transient generation by laser-produced cavitation bubbles near solid boundaries. *J. Acoust. Soc. Am.*, 84(2), 719–731.
- Wang, Y.-C., & Brennen, C. E. (1995). The Noise Generated by the Collapse of a Cloud of Cavitation Bubbles. *Cavitation and gas-liquid flow in fluid machinery devices* (pp. 17–29). ASME.
- Wang, Z., Zhang, X., Wang, Y., & Liu, J. (2021). Comparative study between turbulence models in unsteady cavitating flow with special emphasis on shock wave propagation. *Ocean Eng.*, 240, 109988.
- Wen, H., Yao, Z., Zhong, Q., Tian, Y., Sun, Y., & Wang, F. (2023). Energy partitioning in laser-induced millimeter-sized spherical cavitation up to the fourth oscillation. *Ultrason. Sonochem.*, 95, 106391.
- Wu, J. (2019). *Bubbly shocks in separated cavitating flow* (Doctoral dissertation). University of Michigan.

- Wu, X., Maheux, E., & Chahine, G. L. (2017). An experimental study of sheet to cloud cavitation. *Exp. Therm Fluid Sci.*, 83, 129–140.
- Xu, S., Wang, J., Cheng, H., Ji, B., & Long, X. (2020). Experimental study of the cavitation noise and vibration induced by the choked flow in a Venturi reactor. *Ultrason. Sonochem.*, 67, 105183.
- Yamamoto, K. (2016). Investigation of bubble clouds in a cavitating jet. In Y. Shibata & Y. Suzuki (Eds.), *Mathematical fluid dynamics, present and future* (pp. 349–373). Springer Japan.
- Zhang, G., Khelifa, I., & Coutier-Delgosha, O. (2020). A comparative study of quasi-stable sheet cavities at different stages based on fast synchrotron X-ray imaging. *Phys. Fluids*, 32(12), 123316.
- Zhang, G., Khelifa, I., Fezzaa, K., Ge, M., & Coutier-Delgosha, O. (2020). Experimental investigation of internal two-phase flow structures and dynamics of quasi-stable sheet cavitation by fast synchrotron X-ray imaging. *Phys. Fluids*, 32(11), 113310.
- Zhang, H., Liu, Y., & Wang, B. (2021). Spatial-temporal features of the coherent structure of sheet/cloud cavitation flows using a frequency-weighted dynamic mode decomposition approach. *Phys. Fluids*, 33(5), 053317.

Table 4.1: Experimental conditions for the performed X-ray densitometry measurements. The rows correspond to the markers in Fig. 4.4. The temperature T and system pressure P_∞ are directly recorded. u_{th} is computed from the flow meter by adjusting for the cross-sectional area of the tube and throat. P_{vap} , ρ_{liq} and ρ_{vap} are computed by relations provided in Griggull and Schmidt (1989). U_s is computed by the distance between P1 and P2, divided by the difference in arrival time, see section 4.3.3. The shedding frequency is determined by the arrival of the shock wave at P1. Dimensionless numbers Ca and St are computed with this data.

Ca	P_∞ kPa	P_{vap} kPa	u_{th} m/s	ρ_{liq} kg/m ³	ρ_{vap} kg/m ³	T °C	f_{shed} Hz	St -	U_s m/s
-									
0.415	41.09	2.80	13.59	997.51	44.19	22.91	47.13	0.0578	409.7
0.413	41.48	3.53	13.58	996.52	39.59	26.79	46.54	0.0571	383.7
0.512	35.92	2.88	11.38	997.40	43.61	23.37	54.46	0.0798	407.0
0.513	36.32	3.24	11.38	996.91	41.23	25.33	53.66	0.0786	381.5
0.513	41.14	2.74	12.25	997.60	44.68	22.54	57.62	0.0784	459.7
0.500	41.17	3.24	12.33	996.91	41.23	25.33	54.85	0.0741	416.9
0.518	51.15	2.66	13.70	997.70	45.29	22.08	65.35	0.0795	533.8
0.471	49.90	4.75	13.88	995.00	34.56	31.93	57.82	0.0694	442.5
0.499	51.45	3.09	13.95	997.11	42.13	24.57	61.58	0.0736	499.4
0.617	36.01	2.93	10.37	997.32	43.20	23.69	60.79	0.0977	484.7
0.599	35.94	3.37	10.44	996.73	40.45	26.01	58.81	0.0939	451.0
0.602	51.20	4.31	12.51	995.52	36.07	30.26	72.28	0.0963	401.4
0.610	50.26	2.63	12.51	997.75	45.58	21.86	71.68	0.0955	564.7
0.590	50.33	4.49	12.49	995.31	35.43	30.95	67.92	0.0906	526.1
0.604	50.69	3.03	12.58	997.19	42.55	24.22	70.89	0.0939	558.6
0.615	60.82	2.54	13.78	997.88	46.36	21.29	79.60	0.0963	592.5
0.602	60.50	2.92	13.85	997.34	43.30	23.61	77.43	0.0932	591.9
0.687	69.75	3.60	13.91	996.42	39.20	27.15	86.73	0.1040	591.0
0.707	70.81	2.55	13.91	997.86	46.25	21.37	90.50	0.1084	603.7
0.687	69.42	3.78	13.85	996.20	38.36	27.95	86.73	0.1044	586.5

5

CONCLUSION

5.1. SUMMARY OF THE RESEARCH FINDINGS

Emitted shock waves by collapsing vapor clouds and the propagation through a two-phase gas-liquid mixture are investigated in this thesis. The first goal is the design and validation of two novel experimental methods that allow for accurately measuring shock wave properties (i.e. shock wave speed and magnitude, and shock-induced liquid velocity) to non-intrusively measure the propagation of shock waves through a well-specified two-phase fluid. It is found that the volumetric gas/vapor fraction and shock wave characteristics can be reliably quantified with a single high-speed camera, without recourse to external transducers or seeding particles. The second goal is to quantify the shock wave energy, which is emitted from collapsing vapor cloud bubbles, non-intrusively. The energy conversion from potential energy to shock wave energy is determined by comparing the initially present cavity potential energy E_{pot} to the final emitted shock wave energy E_s for the experimental conditions considered.

5.1.1. FINDINGS ON THE PROPOSED EXPERIMENTAL METHODS

The two experimental methods are specifically designed to perform non-intrusive measurements with limited optical access, for example in an autoclave. One non-intrusive optical experimental technique, based on defocused volumetric shadowgraphy, is proposed to measure the concentration of non-condensable micro-bubbles (in this thesis with a typical diameter of 0.56 mm) in the center of bubble clouds with a single camera. The depth or z -position of the bubbles is retrieved from the degree of defocusing of the bubble images. Two reference methods validate this method independently for the case of a non-condensable gas concentration of 0.08 percent.

A second experimental method is developed for non-intrusive measuring shock wave properties. In absence of seeding particles, the developed hydrodynamic model only requires the input of the gas bubble velocity. The measured shock wave speeds are typically $\mathcal{O}(10^2)$ m/s, so that a split field-of-view (FOV) is applied to the imaging with a single camera to enhance the accuracy of the wave speed measurements in the experimental range of $70 < U_s < 400$ m/s for various gas fractions ($0.01 < \alpha < 3.58$) and impact velocities of 0.85 and 1.70 m/s considered in this thesis. Reference measurements by two-phase particle image velocimetry (PIV) are performed to validate the liquid and gas phase velocities during the shock wave passage, while external pressure transducers validate the computed shock wave pressures. It is found that shock wave speeds are measured accurately with a mean absolute error of approximately 2.0 percent of the average shock speed of 200 m/s for both impact velocities considered in this thesis. Shock pressure measurements prove more challenging than shock wave speed measurements and incur the largest relative uncertainties.

5

5.1.2. FINDINGS ON EMITTED SHOCK WAVE ENERGY

The emission of shock wave energy during the final stage of a vapor bubble cloud collapse is investigated with high-speed X-ray densitometry (at frame rates of 12 and 25 kHz) and simultaneous pressure recordings (at 100 kHz). Within the experimental range for the cavitation number Ca and ambient pressure P_∞ of $0.41 < Ca < 0.71$ and $35.9 < P_\infty < 71.0$ kPa, respectively, on average between 24 and 56 percent of the initial cavity potential energy was converted into shock wave energy for cloud cavitation. For a constant kinetic energy added to the flow, the energy conversion from E_{pot} to E_s increases for decreasing cavitation numbers; see Fig. 4.10 (left). Next, it seems that the amount of energy that is converted into E_s increases for increasing ambient pressures at constant cavitation numbers; see Fig. 4.10 (center and right). Large differences in the projected cloud arrangements between individual cycles are recorded, which likely contributes to the large cycle-to-cycle variance in the energy conversion between E_{pot} and E_s for individual cycles.

5.2. OUTLOOK

Despite the preparations of the experimental novel techniques, the impact load experiments for flow conditions close to thermodynamic equilibrium in the autoclave at MARIN, Wageningen, could not be conducted within the time frame of this funded research due to external construction delays and the effects of the Covid-19 global pandemic. Consequently, some aspects of the original research plan remain open research questions.

Nonetheless, a number of possible directions for future research are presented:

1. Phase transitions are complex phenomena that may lead to large impact loads on structures during sloshing events. By locally altering the compressibility of the two-phase liquid, these theoretically predicted phase changes upon impact complicate the shock wave propagation significantly. It remains unsure whether liquid at the wave crest evaporates rapidly due to local perturbation upon direct impact, which causes an elevated compressibility. This increased vapor fraction causes the acoustic speed to drop significantly, and the exerted load upon the structure is expected to decrease. This could be seen as a ‘cushioning’ effect. Also, the local pressure is likely to drop below the vapor pressure during the passage of the rarefaction part of the shock wave. This would result in local evaporation and thus the occurrence of vapor bubbles within the flow, which may: (1) dampen reflected waves, and: (2) emit shock waves upon collapse. Chapter 4 shows that these transient emitted shock waves, typically short-lived $\mathcal{O}(1 \text{ ms})$, propagate with strong pressure gradients and with pressure magnitudes that can exceed several bars in pressure.
2. The energy conversion from E_{pot} to E_s has a large cycle-to-cycle variation; see Fig. 4.9. The repeatability of the measurements is likely to be reduced by highly complex flow in proximity of the venturi throat. Furthermore, as shown by van Meerkerk (2021), the global wave and gas flow behavior of a plunging breaking wave is repeatable for minimal system variability, while the *local* wave and gas flow behavior can differ significantly. The experimental data on projected vapor clouds also shows variances between cycles; see Fig. 4.13 (top). For precise impact experiments with a quiescent liquid and controlled aeration inside an autoclave, close to thermodynamic equilibrium, the small variations in temperature and pressure may provide insight in the complex dynamics during the growth and collapse of vapor bubble clouds. Combined with the novel experimental techniques presented in this thesis, the effects on shock wave emission and propagation can be studied in detail.
3. The specific vapor bubble arrangement seems to have an effect on the energy conversion from E_{pot} to E_s . Expanding the number of X-ray sources with aligned cameras allows for an enhanced quasi-3D reconstruction in time. This makes it possible to infer the effect of the 3D-structure to the energy conversion rate, so that this geometry factor can be included in the evaluation of the conversion process. This is likely to result in more accurate estimates of the amount of emitted shock

wave energy for each *individual* collapse cycle. Numerical simulations often have insights into vapor volume configurations, the surrounding liquid, and local pressures. Based on the vapor clouds arrangements, numerical simulations may be validated and improved by taking into account this geometry coupling.

4. The discrepancy between E_{pot} and E_s cannot be fully explained by the energy conversion to rebound energy, internal energy, or other losses, including acoustic radiation to the surroundings. Due to possibly asymmetric collapses, liquid jets may occur within the flow, causing complex flow behavior (Schenke et al., 2019). In unpublished experimental observations, impinging liquid jets were sporadically observed in the reference PIV measurements (see Chapter 3) during the collapse of a single vapor bubble. Therefore, in addition to the X-ray measurements, PIV measurement on the flow field around the location of the final bubble cloud collapse in the venturi geometry may resolve the residual kinetic energy. This would require very challenging optical measurements, especially due to the large number of smaller vapor bubbles that collectively form the vapor clouds. The results would indicate if the residual kinetic energy is indeed the missing energy term. Also, based on the measured velocity field, the exact flow mechanism might be identified.
5. The non-intrusive optical measurement for shock wave properties is proposed and validated for stagnant aerated liquid in a vertical impactor experimental setup; see Figure 3.2. It is possible to extend the hydrodynamic model to include aerated steady-state flows in vertical transparent tubes, by computing the relative velocity between the rising bubble and the surrounding liquid a priori to the impact. Since the gas bubble velocity is recorded with the camera, the initial liquid velocity can be computed via the relative velocity. Unsteady flows prior to the impact would still remain challenging, as the initial liquid velocity is difficult to compute by the gas bubble velocity in this case.

BIBLIOGRAPHY

- Schenke, S., Melissaris, T., & van Terwisga, T. (2019). On the relevance of kinematics for cavitation implosion loads. *Phys. Fluids*, 31(5), 052102.
- van Meerkerk, M. (2021). *Variability in wave impacts: An experimental investigation*. (Doctoral dissertation). TU Delft.

ACKNOWLEDGEMENTS

Performing experimental research involves many people with whom I had the pleasure to work with over the last years. First and foremost, I would thank my Promotors, prof. Christian Poelma and prof. Jerry Westerweel, for guiding and supporting me during this PhD project. The many fruitful scientific discussions we have had over several years really helped me to advance in this research topic. I appreciate the academic freedom given to me, and that I could always rely on your guidance, expertise, knowledge about the subject and experimental skills. Many thanks for your highly detailed and constructive feedback, I learnt a lot from this. Christian, thank you for being my daily supervisor during this project. Thank you for offering me the opportunity to pursue a PhD research project in your research group. I experienced it as very welcoming and supportive that your office door was always open to have a quick chat or discussing (small) questions, even when you very busy. I really appreciate your advice that there is always more in the data to discover, of which I learnt is true. Jerry, I appreciate your many ideas and although I could not perform all of them, some ideas really elevated the research to a much higher level then I originally thought was possible, and I am very grateful for these suggestions. It was a sincere privilege to have you both as my Promotors during this PhD research. I have promised several times over the last two years that the dissertation would be completed within weeks, but this time it is finally done.

I also want to express my gratitude to the project partners of the SLING project, of which this research was part of. I appreciate your knowledge and practical applications on this subject. Understanding the complex sloshing dynamics is very relevant for industry and society in general, and I sincerely hope that my current work adds a (small) piece in solving the sloshing dynamics puzzle. The project's semi-annual meetings were organised at several places around the world, including Paris (several times) and Marrakech. I want to thank my fellow PhD candidates (in no specific order) Mike, Reinier, Rien, Ronald, Utkarsh and Yous not only for their keen insights, but also for the enjoyable company during the meetings, conferences and travels!

The experiments in the laboratory involve the cooperation of many people to which I own gratitude. Jasper, although all the efforts and time spent in constructing and adjusting my experimental setups are not directly observable in this thesis, without your help these experiments would have had been much harder to perform. Edwin and Jan, thank

you for helping me with the high-speed camera's, lasers, triggers, LabView scripts, data storage etc. In short, everything needed to record the transient phenomena of interest. Some of the experiments were quite challenging to perform, but with your help it always worked out. Caroline, many thanks for all the administrative work and cheerful chats we had over the years!

The collaborative atmosphere within the research group cannot be underestimated. The willingness to help each other is unparalleled and contributes to a unique research environment. Thanks everyone, I highly appreciated your company! Udhav, thank you for the cooperation during the very productive high-speed X-ray densitometry measurements at TNO! I very much appreciated the weekly Coffee Talks, which allow to present the latest (experimental) results to the group and sharpen the research/experiments even further by the valuable feedback given, and the monthly Fluid Seminars with high esteemed guest speakers. Very enjoyable were the social activities organised by Panta Rhei, such as the Denmark trip (directly two weeks after I started the PhD), the campus survival runs, sailing on the Kaag, movies and board game nights, and the Christmas and potluck dinners. As the Panta Rhei board changes each year, in the year 2019 I organised these social activities together with Tariq and Parviz, to which I look back with great pleasure.

Family and friends also deserves an important place in this acknowledgement. First, my close friends Derick, Frank and Ruben. I have known you since the first year of the bachelor of Applied Physics, now seventeen years ago. During this time, we always remained friends and I value this friendship sincerely. Our annual 'Weekendje weg' is something I always look forward too, and I hope to enjoy this together with you for many more times in the future. As the phase of live changed over the years with marriages and children, it is surprisingly to see how little has changed between us. Frank and Ruben, as both of you already obtained your PhD degree successfully, I am honoured that you are willing to serve as my paranymphs during my PhD defense ceremony.

I am privileged to have wonderful family-in-law. Unfortunately it is not possible to visit you every week due to the larger travel distance, but our extended stays for several weeks in the summer, Christmas and Easter holidays are always very enjoyable. Your kindness and hospitality are unparalleled, and I always feel very much at home. *Tusen takk alle sammen!*

My parents and brother Roy also have a well-deserved place in this acknowledgement. As the combination of finishing a PhD dissertation and working full-time in our family-owned company was sometimes challenging (and not really recommendable), your support and patience over the years has definitely helped me to complete this the-

sis!

My deepest gratitude is for my wife Elise. During this PhD research you experienced fortunate moments in which experiments showed promising results and much progress was made, but also the harder times. Your unconditional, positive and constructive support definitely helped me during the years. Undoubtedly you are the best person I have ever met in my life. My deep appreciation for how you are taking care for our son Lukas. Although you probably don't realise this yet Lukas, but your happiness and curiosity, combined with the enjoyment you express everytime you discover something new, puts everything in perspective. I am looking forward to the years to come!



Wout Cornel
Delft, August 2024

CURRICULUM VITÆ

Wouter Anthonie CORNEL

20-12-1988 Born in 's-Gravenzande, The Netherlands

EDUCATION

2001–2007 **Secondary education**
VWO, Interconfessionele Scholengroep Westland (ISW)
's-Gravenzande, The Netherlands

2007–2010 **Bachelor Applied Physics**
Delft University of Technology, Delft, The Netherlands

2010–2012 **Master Applied Physics**
Delft University of Technology, Delft, The Netherlands
KTH Royal Institute of Technology, Sweden (exchange)
Telemark University College, Norway (internship)

2012–2015 **International Bachelor Economics and Business Economics**
Erasmus University, Rotterdam, The Netherlands
Telemark University College, Norway (internship)

2015-2016 **Master Financieel Recht**
Erasmus University, Rotterdam, The Netherlands

2017–2022 **PhD Multiphase Systems**
Delft University of Technology, Delft, The Netherlands

Promotor : Prof. dr. ir. C. Poelma

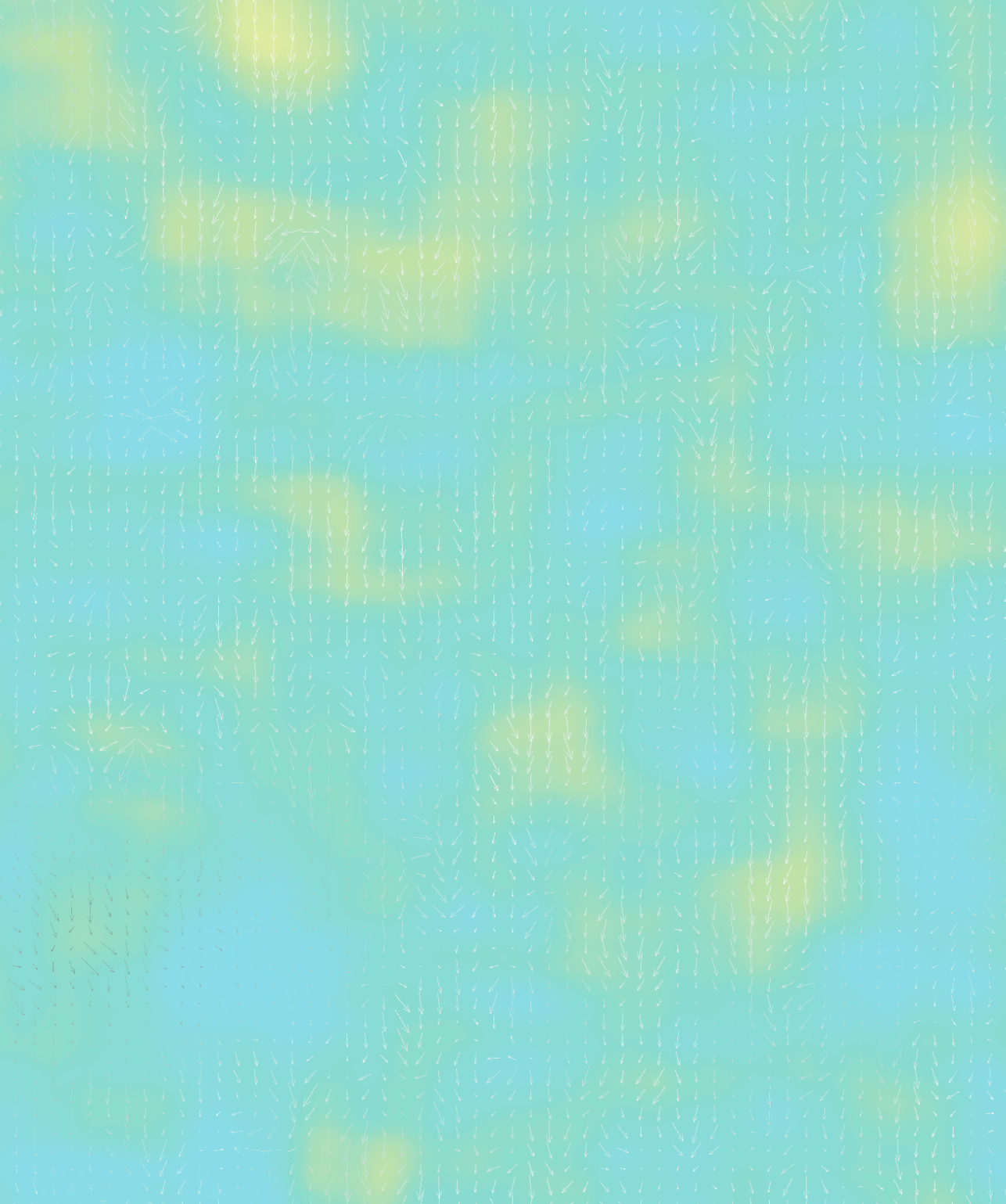
Promotor : Prof. dr. ir. J. Westerweel

WORK

2022–present **Project engineer**
Cornel B.V., 's-Gravenzande, The Netherlands

LIST OF PUBLICATIONS

3. **W.A. Cornel**, J. Westerweel and C. Poelma, *Non-intrusive, imaging-based method for shock wave characterization in bubbly gas–liquid fluids*, Exp Fluids **64**, 35 (2023).
2. S. Schreier, **W.A. Cornel**, C. Poelma. *Dynamic response of sloshing pressure sensors*. Proceedings of the 29th International Ocean and Polar Engineering Conference (ISOPE 2019), Honolulu, Hawaii, USA, June 16-21, 2019
1. **W.A. Cornel**, J. Westerweel and C. Poelma, *Local microbubble concentration by defocused volumetric shadowgraphy with a single camera*, Proceedings 18th International Symposium on Flow Visualization (ISFV18), Zurich, Switzerland, June 26-29, 2018.



 **TU**Delft

The logo for TU Delft, consisting of a stylized black flame or torch icon above the letters "TU" in a bold, blue, sans-serif font, followed by the word "Delft" in a black, sans-serif font.